

SPACE FOCUSING AND MASS SELECTION OF TRANSITION-METAL-CHLORINE
AND -SULFUR CLUSTERS GENERATED THROUGH LASER ABLATION

by

Yongzhi Yu

B.Sc., The University of Science and Technology of China, 1997

A Dissertation Submitted in Partial Fulfillment of the
Requirements for the Degree of

MASTER OF SCIENCE
in the Department of Chemistry

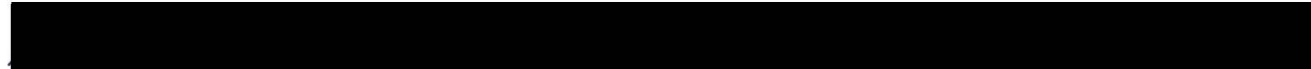
We accept this dissertation as confirming
to the required standard


Dr. C. X. W. Qian, Co-Supervisor (Department of Chemistry)


Dr. T. M. Fyles, Co-Supervisor (Department of Chemistry)


Dr. D. J. Berg, Departmental Member (Department of Chemistry)


Dr. D. A. Harrington, Departmental Member (Department of Chemistry)


Dr. A. Watton, Outside Member (Department of Physics and Astronomy)


Dr. D. Canil, External Examiner (School of Earth and Ocean Sciences)

© Yongzhi YU, 2001

All rights reserved. This dissertation may not be reproduced in whole or in part, by
photocopying or other means, without the permission of the author.

QD172
T6Y8

Abstract

The goal of this study was to develop a laser ablation-TOF mass spectrometer system suited to the generation of transition metal -chlorine and -sulfur clusters.

A detailed characterization of the plasma generated by laser ablation was accomplished. Positive clusters were shown to have a slower original flight speed than negative clusters from the same source. The approximate time window during which clusters reached the repeller with the maximum density was measured as well.

A functional triggered TOF-Mass spectrometer was built with adjustable space focusing parameters. This setup works to space focus the positive or negative clusters generated by the laser ablation. The optimized mass resolution this setup can provide is about 300. A functional mass gate was built. The mass gate can isolate a particular mass peak with about 95% purity for clusters with flight times that differ by $1.1\mu\text{s}$.

Many ionic transition metal-chlorine and -sulphur clusters were synthesized and identified, and a systematic survey of the transition metal-chlorine clusters was conducted. Trends were evident in the formation of negative clusters that can be explained by a simple building block model. To a lesser extent, the building block model can be applied to some of the positive clusters. The formation of transition metal -sulphur clusters was far more complicated.

[REDACTED]

Dr. C. X. W. Qian, Co-Supervisor (Department of Chemistry)

[REDACTED]

Dr. T. M. Fyles, Co-Supervisor (Department of Chemistry)

[REDACTED]

Dr. D. J. Berg, Departmental Member (Department of Chemistry)

[REDACTED]

Dr. D. A. Harrington, Departmental Member (Department of Chemistry)

[REDACTED]

Dr. A. Watton, Outside Member (Department of Physics and Astronomy)

[REDACTED]

Dr. D. Canil, External Examiner (School of Earth and Ocean Sciences)

Table of Contents

Abstract	i
Table of Contents	ii
List of Tables	v
List of Figures	vi
Acknowledgments	viii
Dedication	x
Chapter 1: General Introduction	1
1.1 What are clusters?	1
1.2 Why Study Clusters?	2
1.3 How to Generate Clusters	5
1.4 Techniques to Study Metal Clusters.....	7
1.4.1 Fourier Transform Infrared Spectroscopy	8
1.4.2 Infrared Photodissociation Spectroscopy	9
1.4.3 Photodissociation Spectroscopy	9
1.4.4 Collision Induced Dissociation	10
1.4.5 Flow Tube Reactor	11
1.4.6 Photoelectron Spectroscopy	12
1.4.7 ZEKE Spectroscopy	13
1.4.8 Resonance Two Photon Ionization Spectroscopy.....	14
1.4.9 Laser Induced fluorescence (LIF)	15
1.5 Goals of Thesis	16
Chapter 2: Experimental Setup	17
2.1 The Vacuum System	17
2.2 Molecular Beam Source	19
2.2.1 Sample Gas	19
2.2.2 The Molecular Beam Valve	21
2.2.3 The Reaction Chamber	22
2.2.4 Metal rods	23
2.3 Lasers and Optics	24

2.4 Time of Flight Mass Spectrometer	24
2.4.1 TOF Mass Spectrometer	24
2.4.2 High Voltage switch setups for the Repeller	27
2.5 The Ion Deflector	29
2.6 the Mass Gate	30
2.7 Detection of negative ions, positive ions and neutral particles	32
2.7.1 Detection of positive ions and neutral particles	32
2.7.2 Detection of negative ions	34
2.7.3 Shielding of the detector	37
2.8 The oscilloscope	37
2.9 Timing, triggering, computer interface and software	39
2.10 Experimental Procedures	43
Chapter 3: Characteristics of the Molecular Beam	46
3.1 The Length of the Molecular Beam	47
3.2 Density Distribution of the Negatively charged Clusters	50
3.3 Molecular Beam Generated with Different Kinds of Beam Source	52
3.4 Density Distribution of Positively charged Clusters in the Molecular Beam	57
Chapter 4 TOF-MS Space Focusing	59
4.1 Theory	59
4.1.1 Overview	59
4.1.2 The TOF Mass Spectrometer setup	60
4.1.3 Flight Time	62
4.1.4 Spatial Resolution	63
4.1.5 Energy Resolution	64
4.2 Experimental Space Focusing Result	65
Chapter 5: Species Generated from Laser Ablation of Transition Metal in a Chlorine or Hydrogen Sulfide Carrier Gas	69
5.1 Transition Metal-chlorine clusters	69
5.1.1: Titanium Chlorides	69
5.1.2: Chromium Chlorides	71
5.1.3: Iron Chlorides	73
5.1.4: Cobalt Chlorides	75
5.1.5: Nickel Chlorides	79

5.1.6: Copper Chlorides	81
5.1.7: Zinc Chlorides	84
5.1.8: Summary	86
5.2 Some molecular orbital considerations	90
5.3 Aluminum-chlorine Clusters	95
5.4 Transition Metal-Sulfur Clusters	97
Chapter 6 Mass Gate Purification of the Clusters	101
6.1 Theory	101
6.2 Selection and rejection of clusters of a specific mass	108
6.2.1 Selection of clusters with one specific mass	108
6.2.2 Rejection of clusters with one specific mass	110
Chapter 7: Conclusion	112
7.1 Summary	112
7.2 Possible Future Spectroscopy Work	115
References	117

List of Tables

Table 3.1:	The density distribution of C_2^- and C_3^- in the molecular beam ...	51
Table 3.2:	The negatively charged clusters collected from normal source...	52
Table 3.3:	The negatively charged clusters collected from source with the U-tube	54
Table 5.1:	Possible building block combination of negatively charged iron-chlorine clusters and their relative intensity	73
Table 5.2:	Building block combination of negatively charged cobalt-chlorine clusters and their relative intensity	76
Table 5.3:	Building block combination of negatively charged nickel-chlorine clusters and their relative intensity	80
Table 5.4:	Building block combination of negatively charged copper-chlorine clusters and their relative intensity	82
Table 5.5:	Building block combination of positively charged copper-chlorine clusters and their relative intensity	83
Table 5.6:	Building block combination of negatively charged zinc-chlorine clusters and their relative intensity	85
Table 5.7:	Experimentally observed transition metal-chlorine ions and their relative intensity	88
Table 5.8:	Experimentally observed transition metal-sulfur ions and their relative intensity	100
Table 6.1:	The functionality of the mass gate for single ion selection	110
Table 6.1:	The functionality of the mass gate for single ion rejection	110

List of Figures

Figure 1.1:	Gradual Transition from Molecular Behavior to Solid Behavior of Clusters	1
Figure 2.1:	Experimental Setup	18
Figure 2.2:	The molecular beam laser vaporization source	20
Figure 2.3:	The TOF mass spectrometer ion repeller setup	25
Figure 2.4.1:	The circuit used to repel negatively charged clusters	28
Figure 2.4.2:	The circuit used to repel positively charged clusters	28
Figure 2.5:	The mass gate setup	31
Figure 2.6:	The circuit used by mass gate for negatively charged clusters	32
Figure 2.7.1:	Setup and circuit to detect positively charged clusters	33
Figure 2.7.2:	Setup and circuit to detect negatively charged clusters	35
Figure 2.8:	The experimental interface layout	41
Figure 2.9:	Diagram of the triggering sequence	42
Figure 3.1_a:	TOF spectrum collected at a repeller delay of 240 μ s	48
Figure 3.1_b:	TOF spectrum collected at a repeller delay of 410 μ s	48
Figure 3.1_c:	TOF spectrum collected at a repeller delay of 350 μ s	49
Figure 3.2:	Density distribution of C ₂ ⁻ and C ₃ ⁻ in the molecular beam	51
Figure 3.3:	Negatively Charged clusters from normal source	53
Figure 3.4:	Molecular beam laser vaporization source	55
Figure 3.5_a:	Negatively charged clusters obtained from source with U-tube (flight time 14~24 μ s)	55
Figure 3.5_b:	Negatively charged clusters obtained from source with U-tube (flight time 6~13 μ s)	56
Figure 3.6:	Density distribution of the TiCl ₃ ⁻ and TiCl ₃ ⁺ clusters in the molecular beam	57
Figure 4.1:	TOF setup in our experiment	61
Figure 4.2_a:	TOF mass signal without space focusing	66
Figure 4.2_b:	TOF mass signal with space focusing	66
Figure 4.3:	The Mass Spectra of aluminum-chlorine negatively charged clusters	68

Figure 5.1:	Mass spectrum of negatively charged titanium-chlorine clusters	70
Figure 5.2:	Mass spectrum of positively charged titanium-chlorine clusters	70
Figure 5.3:	Mass spectrum of negatively charged chromium-chlorine clusters ..	71
Figure 5.4:	Mass spectrum of positively charged chromium-chlorine clusters ...	72
Figure 5.5:	Mass spectrum of negatively charged iron-chlorine clusters	74
Figure 5.6:	Mass spectrum of positively charged iron-chlorine clusters	75
Figure 5.7:	Mass spectrum of negatively charged cobalt-chlorine clusters	76
Figure 5.8_a:	Mass spectrum of positively charged titanium-chlorine clusters	78
Figure 5.8_b:	Another mass spectrum of positively charged titanium-chlorine clusters	78
Figure 5.9:	Mass spectrum of negatively charged nickel-chlorine clusters	79
Figure 5.10:	Mass spectrum of positively charged nickel-chlorine clusters	81
Figure 5.11:	Mass spectrum of negatively charged copper-chlorine clusters	82
Figure 5.12:	Mass spectrum of positively charged copper-chlorine clusters	84
Figure 5.13:	Mass spectrum of negatively charged zinc-chlorine clusters	85
Figure 5.14:	Mass spectrum of positively charged zinc-chlorine clusters	86
Figure 5.15:	MO diagram of CuCl_2^-	91
Figure 5.16:	MO diagram of CrCl_3^-	93
Figure 5.17:	MO diagram of TiCl_4^-	94
Figure 5.18:	The possible structure of negative aluminum chlorine clusters	96
Figure 5.19_a:	Mass spectrum of negatively charged nickel-sulfur clusters	99
Figure 5.19_b:	Another mass spectrum of negatively charged nickel-sulfur clusters	99
Figure 6.1:	Important parameter settings of the mass gate in our experiment ...	102
Figure 6.2_a:	V_M as a function of time to singly select a specific mass peak or group for a negatively charged cluster	103
Figure 6.2_b:	V_M as a function of time to singly reject a specific mass peak or group for a negatively charged cluster	103
Figure 6.3:	Mass spectrum of negative carbon clusters	104
Figure 6.4:	The mass gate voltage profiles	107
Figure 6.5:	The selection result of the mass gate to select clusters with a specific mass	109
Figure 6.6:	The rejection result of the mass gate to reject clusters with a	

	specific mass	111
Figure 7.1:	A possible modification to perform spectroscopic work	115

Acknowledgments

Many people were of great assistance to me in the completion of this dissertation. I would like to thank all of them. I am especially grateful to

Dr. Charles X.W.Qian, my supervisor, for his continuous scientific advice and financial support during my time at Uvic. Many comments from him and many insightful discussions with him benefited me greatly.

Dr. Tom Fyles, my co-supervisor, for his kind and devoted help for my thesis writing. It is his contribution that makes me finally finish this thesis. I learned a lot during each discussion with him.

Dr. Chuanfan Ding, a post doctor in our group and a good friend of mine, for his kind help during most of the experiments and many of the very useful suggestions. Working with him is a great pleasure in my life, we worked together to finally finished the experimental setup.

Dr. Walter J. Balfour, for what I have learned from him about spectroscopy and many other very useful suggestions.

Roy Jensen for his instructive discussions and friendship, his critical suggestions and fast mind helped me solved many problems during the experiments.

Bob Dean of the instrument shop, for helping me accomplished many of the electronic circuit designs.

Roy Bennett and Richard Robinson of the machine shop for helping me built up our experimental setups.

Ms Romey Heuff, for her instructive discussion and her friendship.

Dr. Jian Ying Cao for his contributions in developing software during the early stage of the project.

Huanhuan Liang, my wife, for her heart devoted supports and understanding.

Dedication

to

Echo Huanhuan Liang (my dear wife)

Zuolong YU (my dear father)

and Bailan Zhang (my dear mother)

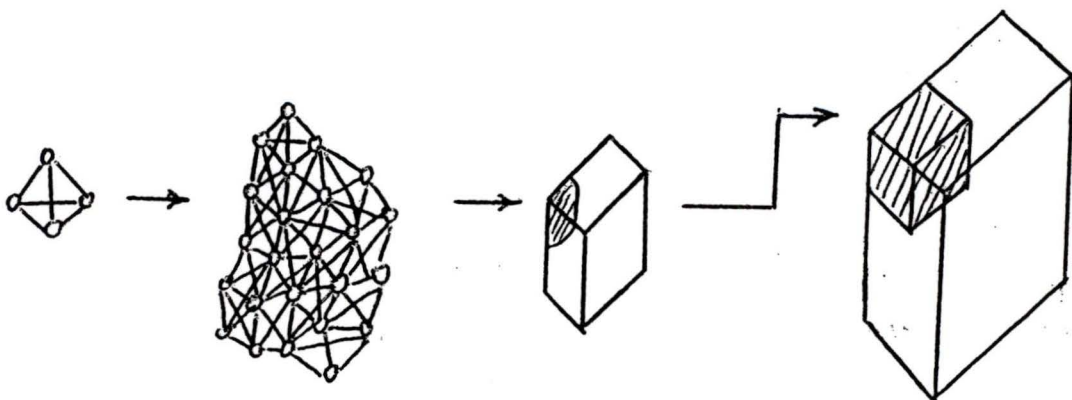
Chapter 1: General Introduction

1.1 What are clusters?

As is defined in a dictionary, a cluster is “a number of things of the same sort gathered together or growing together.” The clusters discussed in this thesis are collections of atoms or molecules, typically, metal cations and chlorine or sulfur anions. Atomic and molecular clusters are a new state of matter, which is neither gas, liquid, nor solid. A cluster is simply a group of atoms bound together with forces whose strength and character determine the behavior of the cluster. As the number of atoms in a cluster increases, a gradual transition from molecular behavior to solid behavior can be realized. Clusters are simple examples of nanostructures, which have the size of 1 ~100 nanometers. In this context, clusters can be defined as small aggregates of atoms or molecules in a state that bridges the isolated atoms and molecules and the condensed states of matter.

The Figure below shows an impression of this kind of transition:

Figure 1.1 Gradual Transition from Molecular Behavior to Solid Behavior of Clusters



Moving from left to right, a four-atom cluster might look like a pyramid; a larger cousin looks like a complex ball, while at another size the cluster will perhaps adopt a cubic structure, which is common for solid matter. Our research interest is to generate different sized charged clusters in the gas phase and to study how the clusters are related to the bulk material in condensed phases by studying their periodical trends and molecular structures.

Nowadays, the study of clusters is an interdisciplinary field involving such areas as catalysis, surface science, condensed matter physics, and material science. As an example, one can point to the discovery of a third form of carbon (other than diamond and graphite) composed of 60 carbon atoms, as the best fruit harvested from cluster research. This C_{60} cluster was named Buckminsterfullerene, after Buckminster Fuller, the architect of geodesic dome. With the nickname "Bucky", C_{60} is a chemically bonded cluster of sixty carbon atoms, with each atom occupying once of the sixty vertices of a soccer ball. Smalley, Kroto, and Curl were awarded the 1996 Nobel Prize for this discovery [1,2,3]. Cluster science continues to be an active and exciting field.

1.2 Why Study Clusters?

First, cluster studies can provide new understanding about the surface of the bulk when clusters are used as a model for surfaces. As we know, knowledge of the detailed surface electronic structure is very important in the understanding of the chemisorptive and catalytic properties of functional materials. Studies of surfaces have been concentrated on the detection of the electronic states not

found in the bulk that are generated by the presence of the surface. These states are called the surface states. The energy of the surface states of interest in catalysis commonly lies near the Fermi level of the solid. These surface states are either partially filled with electrons so that they can both donate and accept electrons from the molecules interacting with the surface, or are close enough to a filled valence band (or an empty conduction band) such that, together, they provide a pair of states to simultaneously accept and donate electrons to interacting molecules [4].

Clusters have high surface-to-volume ratio, and their chemistry is one that occurs essentially on their surfaces. At the same time, surface science is one of the most economically significant areas of chemistry, and one of the least understood. The capability for experiments with clusters of a controlled range of sizes, combined with the future outlook for computation of cluster properties, will ultimately develop into a fundamental understanding of their surface chemistry and physics. This understanding will lead to some comprehension of the behavior of bulk surfaces. Thus, research on small clusters is closely related to surface physics. This is because a cluster is composed mainly of surface atoms, and a real solid state surface is composed mainly of clusters. Therefore, a cluster can be viewed as a surface model.

A second reason to study clusters is that clusters carry out chemical reactions in new ways. One of the promising applications of clusters is in industrial catalysis, which is central in petroleum refining (to recover gasoline fractions from heavier distillates), in pollution control (to oxidize or reduce noxious emissions),

and in the synthesis of pharmaceutical compounds. Catalysis begins where the surface of a catalyst begins. The efficiency of a catalyst depends on its ability to attract reactants strongly enough for adsorption, and to hold their end products weakly enough for desorption [5]. Clusters are also the ideal laboratories for studying active sites because their unfulfilled bonding capacity makes them adsorb small molecules readily and their small size limits the number of possible adsorptions. These properties also make them possible sources of highly specific catalysts which do what they are intended to do, and only what they are intended to do. This specificity is highly prized in industry because many catalysts speed undesired reactions as effectively as they speed desired ones.

A third reason to study clusters is that clusters are novel materials with novel properties. Thin films of clusters possessing desired electronic qualities would be of great interest in microelectronics. One can foresee their application in optical memories, image processing and superconductivity. Because of their particular size property, they can be used to construct small parts of an electronic network and to connect these small parts together. It may eventually be possible to create electronic devices on a molecular scale [6]. Ultimately a machine might be designed that could serve as a link between solid state electronics and biological systems, such as systems of neurons. Such a link might, for example, convey data from a television camera to the brain of a blind person.

Clusters of certain metals have a great ability to absorb light. This is caused by the extreme density of their valence electrons, their high surface-to-volume ratio (which puts many electronic states near the surface), and the ease with which

their electron clouds can be distorted, or polarized [7]. On the basis of a given cluster chemistry and size, it is possible to predict which wavelength of light it will absorb. Because clusters are so photoreceptive they can often absorb more than one photon, which is a useful quality in light-initiated chemical processes. If suspended in a transparent medium, metal clusters may also be used as efficient radiation detectors, wavelength-specific light filters, or elements in an optical memory system.

1.3 How to Generate Clusters

There are many ways to produce clusters. The most powerful technique is by laser vaporization into a supersonic cluster of carrier gas [8]. With this technique, a powerful pulsed laser is focused on a solid material near a nozzle of a molecular beam. The laser evaporates a small amount of the material, injecting it into the cold gas streaming from the nozzle. The evaporated material is rapidly cooled by the gas jet and subsequently aggregates into clusters. The supersonic jet is formed by expanding helium gas and passing it through a tiny nozzle into a vacuum. The helium carries heat away from the clusters seeded in the helium, reducing their internal temperature to close to absolute zero. In addition, other reactive gases such as Cl_2 , H_2S , C_2H_2 , O_2 , NH_3 , N_2 , can be seeded into the helium in order to react with the evaporated materials and form other more interesting clusters.

Laser vaporization techniques have proved to be the most powerful methods of forming clusters of reactive materials. This thesis describes an apparatus that

uses this method to generate charged clusters. The details of the setup will be described in the following chapters.

In addition to the laser vaporization source that was used, there are other functional cluster sources. The characteristics of the most commonly used comparable cluster sources are listed as follows:

1. Seeded supersonic nozzle sources are most frequently used to produce intense cluster beams of low-boiling-point metals [9]. With this method, a metal is vaporized in a hot oven. The metal vapor is mixed with (or seeded in) an inert carrier gas by pressurizing the oven with the inert gas. Typically the inert-gas pressure is several bars, whereas the metal vapor pressure is in the range of 10-100 mbar. The vapor/gas mixture is ejected into a vacuum via a small hole, producing a supersonic molecular beam. The expansion into the vacuum proceeds adiabatically and causes cooling of the mixture. The cooled metal vapor becomes supersaturated, condensing as clusters. These sources produce continuous beams with reasonably narrow speed distributions. Clusters with up to several hundreds of atoms per cluster may be produced in adequate abundance [9].

- 2: Gas-aggregation cluster sources are particularly efficient in the production of large clusters ($N < 10000$). [10] Metal is vaporized and introduced in a flow of cold inert gas. This causes the vapor to become supersaturated. Due to the low temperature of the inert gas, cluster production proceeds primarily by successive single-atom addition. The intensities of the clusters produced are generally much lower than for a nozzle source.

3: Pulsed-arc cluster-ion sources use an intense electrical discharge rather than a laser to produce the clusters, resulting in intense cluster-ion beams [11]. This source has some advantages compared with the laser vaporization source. The beam tends to be very intense; furthermore, this source is significantly less expensive because it does not require a laser. However, the beam is hotter than that produced by laser vaporization.

4: Ion-sputtering sources are used primarily to produce intense continuous beams of small singly ionized clusters of most metals [12]. Typically, the clusters are hot near the evaporation limit. Cluster-ion beams are produced by bombarding a metal surface with high-energy inert-gas ions. Most often, heavier inert gases (Kr or Xe) are used, while bombardment energies range from about 10 to 20 KeV with currents up to 10 mA. The clusters are usually cooled by in-flight evaporation.

5: Liquid-metal ion sources produce singly and multiply ionized clusters of low-melting-point metals. These clusters are hot, since in-flight evaporation and fission are observed [13].

1.4 Techniques to Study Metal Clusters

There are several techniques that can be used to study the electronic and/or geometric structure of clusters. Photofragmentation or collision-induced dissociation can be used to achieve the dissociation energies. Chemisorption can be used to probe geometric structures [32,33,34], and photoelectron spectroscopy can be used to obtain the ionization potentials and electron

affinities of clusters [35,36,37]. More powerful experimental probes of the electronic structures, such as resonance two photon ionization (R2PI) [46,47,48] or laser induced fluorescence (LIF), might also be used to study clusters. However, these techniques have been proven to be unsuccessful in probing metal clusters. Both methods require that the first laser induced transition populates an excited state that lives long enough to be detected either by its fluorescence (LIF) or through the absorption of a second photon, resulting in a reduced ionization threshold. Although a few metal dimers and trimers have been successfully probed by these techniques [14], metal clusters in general possess a high density of low-lying excited states which couple together quite easily. Any energy deposited into one of these states is quickly dissipated via radiationless transitions, and the excited state is not sufficiently long-lived to be probed by techniques such as LIF or R2PI. The same manner is not true for small mono-metal chlorine clusters, which behave much more like an ion with clearly distinguished excited states [15].

In the following discussion, a brief summary of the principle and application of each technique is presented.

1.4.1 Fourier Transform Infrared Spectroscopy

Andrews' group and Lindsay's group used Fourier transform infrared spectroscopy to study metal oxides [16,17,18,19] and tantalum clusters [20] entrapped in an inert matrix. The clusters are ablated from a target and then collide with argon atoms during the condensation process. The energetic product

molecules are relaxed and trapped in a solid argon matrix for spectroscopic study. This method usually provides only spectroscopic information about the ground state of cluster species.

1.4.2 Infrared Photodissociation Spectroscopy

Fujimaki's group [21,22,23] has represented some infrared photodissociation spectroscopy studies on several metal organic clusters.

Infrared photodissociation spectroscopy can probe the intimate details of how molecules and atoms adsorb onto metal clusters. Photodissociation spectroscopy detects absorption when it is accompanied by dissociation of photoexcited species. For example, clusters of transition metal atoms are allowed to react with small metal-containing particles that make-up many industrial catalysts. A powerful infrared laser is used to excite the characteristic vibrations of the atoms or molecules adsorbed on the surfaces of the clusters, causing the complexes to fragment. The resulting photodissociation spectrum is capable of revealing whether or not the adsorbed molecules have undergone a chemical reaction after sticking to the surface of the cluster. It is anticipated that these experiments will contribute to our understanding of particle size effects and their influence on reaction mechanisms and pathways in heterogeneous catalysis systems.

1.4.3 Photodissociation Spectroscopy

Fuke's group [24] and Kleiber's group [25] did several photodissociation spectroscopy studies on clusters. A caveat in photodissociation spectroscopy is that absorption is only detected when the absorbed energy results in dissociation. Thus, single photon photodissociation spectra are a convolution of the absorption and dissociation events for each given cluster. These two events can be separated by using two different color photons to perform resonant two-photon photodissociation spectroscopy (R2PD). In R2PD, clusters are irradiated with the first photon, followed by the second photon. The first photon performs the spectroscopy and the second higher energy photon adds additional energy so that clusters can dissociate. Such a technique was used by Zhang's group to study the gas phase PdI_2 molecule [26].

1.4.4 Collision Induced Dissociation

Collision Induced Dissociation (CID) studies on clusters have been mainly carried out by Armentrout's group. [27,28,29,30,31]

CID is another experimental technique used to measure quantitatively the thermodynamic stabilities of clusters in the form of the bond dissociation energies. Positively charged cluster ions are generated in a laser vaporization-supersonic expansion source. The use of a 7 kHz repetition rate copper vapor laser for sample vaporization, with a continuous flow helium carrier gas, results in an essentially continuous cluster ion beam. The ion source is mass-selected after it is focused into a magnetic-sector momentum analyzer that acts as a mass

filter. The resulting mass-selected ion beam is decelerated to a well-defined and variable kinetic energy (0 –1000 eV), and injected into a radio frequency octopole ion beam guide. The octopole directs the beam through a gas cell that contains a neutral reactant gas (Xe, for example). The octopole minimizes losses due to scattering of both reactant and product ions. Thus, the ions are collected with high efficiency and injected into a quadrupole mass filter for product mass analysis. The mass intensity is converted into reaction cross sections from the laboratory to center-of-mass frame.

1.4.5 Flow Tube Reactor

Riley and his partners used a flow tube reactor to study small molecules' chemisorption on clusters. [32, 33, 34]

Before going into details of a flow tube reactor, the following question should be asked: What is the relationship between the structure and size of a metal catalyst particle and its catalytic activity? Over the years, surface science has refined the concept of structure-reactivity relationships for well-characterized metal surfaces, but such relationships have yet to be established for small particles. Yet only with an understanding of such relationships will chemists be able to design better and more efficient heterogeneous catalysts. The study of such structure-reactivity relationship in clusters can be achieved by a continuous-flow-tube-reactor (FTR). Clusters are generated by laser vaporization of an isotopically purified metal target located in a FTR. After growth and thermalization, the clusters react with gas phase molecules introduced into the

FTR. Continuous gas flow is used throughout, allowing careful control and characterization of such reaction conditions as temperature, reagent gas pressure, and cluster-molecule interaction times. At the end of the FTR, clusters and their reaction products are formed into a molecular beam and detected in a laser-ionization time-of-flight mass spectrometer. The experimental procedure consists of varying reaction conditions and recording the resulting changes in the relative amounts of the various reaction products.

Reactivity studies include measurements of absolute reaction rate constants, the determination of the temperature dependence of cluster reactions and their thermodynamic properties, studies of the clusters with reagent molecules, and the probing of chemical transformations on cluster surfaces such as isotopic hydrogen exchange and adsorbate decomposition.

Determining cluster structure is a more difficult problem. Very small clusters with tens of atoms cannot be probed by traditional microscopic techniques. The only information about the structure of small clusters is deduced from the uptake experiments of small molecules, such as ammonia or deuterium, through chemisorption on clusters.[32,33,34]

1.4.6 Photoelectron Spectroscopy

Wang's group had done several photoelectron spectroscopy studies on transition metal clusters.[35,36,37] Photoelectron spectroscopy was first developed by Siegbahn in 1969, and has contributed tremendously to a detailed understanding of the electronic structure of atoms and molecules, surfaces, and

bulk matter.[38] Photoelectron spectroscopy can be used to detect the electronic structure of cations and to obtain the ionization potential of neutral species. There have been many reports on measuring the ionization potentials (IPs) of clusters in the past decades [35,36,37]. Photoelectron spectroscopy of anions can be used to obtain spectroscopic information about neutral species.

Photoelectron spectroscopy of negatively charged particles can be interpreted using two different models. The quantum mechanical exact description assigns each spectral feature to a transition from a vibronic state of the anion to a vibronic state of the neutral particles [37]. If one uses a laser ablation technique, the anions are cooled by the supersonic expansion. Thus, they should be in their electronic ground state. Only in rare cases have features been observed due to a transition from electronically excited anions present in the beam. If the anion is in its ground state, in most cases the spectroscopic feature at lowest binding energy corresponds to the transition into the ground state of the neutral. The time scale of the photoelectron detachment process is fast with respect to the movement of nuclei. Therefore, the observed features correspond to the electronic states of the neutral cluster which has the ground geometry of the anion.

1.4.7 ZEKE Spectroscopy

To achieve better resolution, a novel high resolution technique called ZEKE spectroscopy has been introduced [39,40,41,42,43,44]. Instead of detecting the normal photoelectrons, it detects electrons from a narrow range of states near

the ionization level, or near its electron detachment threshold. Typically it uses a delayed electric field to detect these states which are otherwise hidden in the much larger signal of all electrons or ions. Neumarks' group and Schlag's group have applied this technique to negatively charged cluster ions with a laser ablation source, and have obtained interesting vibrationally resolved spectra for several small semiconductor clusters [39,40], and iron oxide [41]. Hackett's group employed the technique of pulsed-field-ionization zero-kinetic-energy (PFI-ZEKE) photoelectron spectroscopy to probe the electronic structure of a few transition metal cation clusters [42,43,44] and transition metal monoxide clusters [45]. While this is unquestionably a high resolution technique, it is a laser spectroscopy rather than a photoelectron spectroscopy technique. The information is mostly about the ground state, and perhaps a few low-lying excited states, and it is difficult for it to probe deep into the inner electronic energy level of a cluster.

1.4.8 Resonance Two Photon Ionization Spectroscopy

Breckenridge [46], Lee [47], and Kleinermanns [48] used resonance two photon ionization spectroscopy (R2PI) to study small metal clusters and hydrogen-bonded phenol-acid clusters. In R2PI spectroscopy, particles in the electronic ground state are excited using laser radiation (e.g. a dye laser) with a tunable photon energy. A second laser with a fixed photon energy, usually operating in the UV, serves to ionize the excited molecules. The intensity of the ions or the electrons that are ionized by the second laser is recorded as a

function of the photon energy of the tunable laser. The spectra exhibit peaks at photon energies corresponding to the optical transitions of the excited particle. Only dipole allowed transitions are observed.

1.4.9 Laser Induced fluorescence (LIF)

Yamanouchi used LIF to study C_3 cluster [49], and A. M. Ellis used LIF to study several Ga clusters [50]. LIF is similar to R2PI. Instead of detecting the ion or the electron signal as a function of the tunable photon energy, LIF measures the photon signal from the fluorescence of the excited states of the species. Both R2PI and LIF provide the electronic information about the ground and excited states of the particles.

1.5 Goals of Thesis

The main aim of this dissertation is to construct an experimental system that can generate different kinds of clusters ready for detailed spectroscopic study. In order to accomplish this goal, the following four phases must be accomplished.

1. Study the characteristic of the plasma generated by the laser ablation. In order to successfully separate the clusters (negative, positive, or neutral) in the original beam, a detailed understanding of the characteristic of the plasma generated must be achieved. The density distribution of the charged and neutral clusters inside the original beam, and the time that the maximum density will reach the repeller, will provide important information of when to collect the clusters in order to get the maximum yield.

2. Space focus the clusters so that a TOF–mass spectrum can be collected. The clusters separated from the original plasma need to be mass selected so that different clusters with different masses will reach the detector at different times. This must be done through a space focusing technique. As the space focusing goal is accomplished, a TOF–mass spectrum can be generated, and the clusters can eventually be pre–analysed according to their mass.

3: Synthesis of charged transition-metal-chlorine and -sulfur clusters. With space focusing, the ions and charged clusters generated by laser ablation can be detected. Therefore, the third goal of this dissertation was to qualitatively assess the synthesis of transition-metal-chlorine and -sulfur clusters in the gas phase. To our knowledge, these gas phase clusters are new species that have not previously been detected in the gas phase.

4: Isolate clusters of a single mass from others. This can be accomplished by using a mass gate that will only allow a cluster with a specific mass to pass the gate. A spectroscopy experiment can then be carried out following the mass gate in order to study the pre-mass-selected clusters

Chapter 2: Experimental Setup

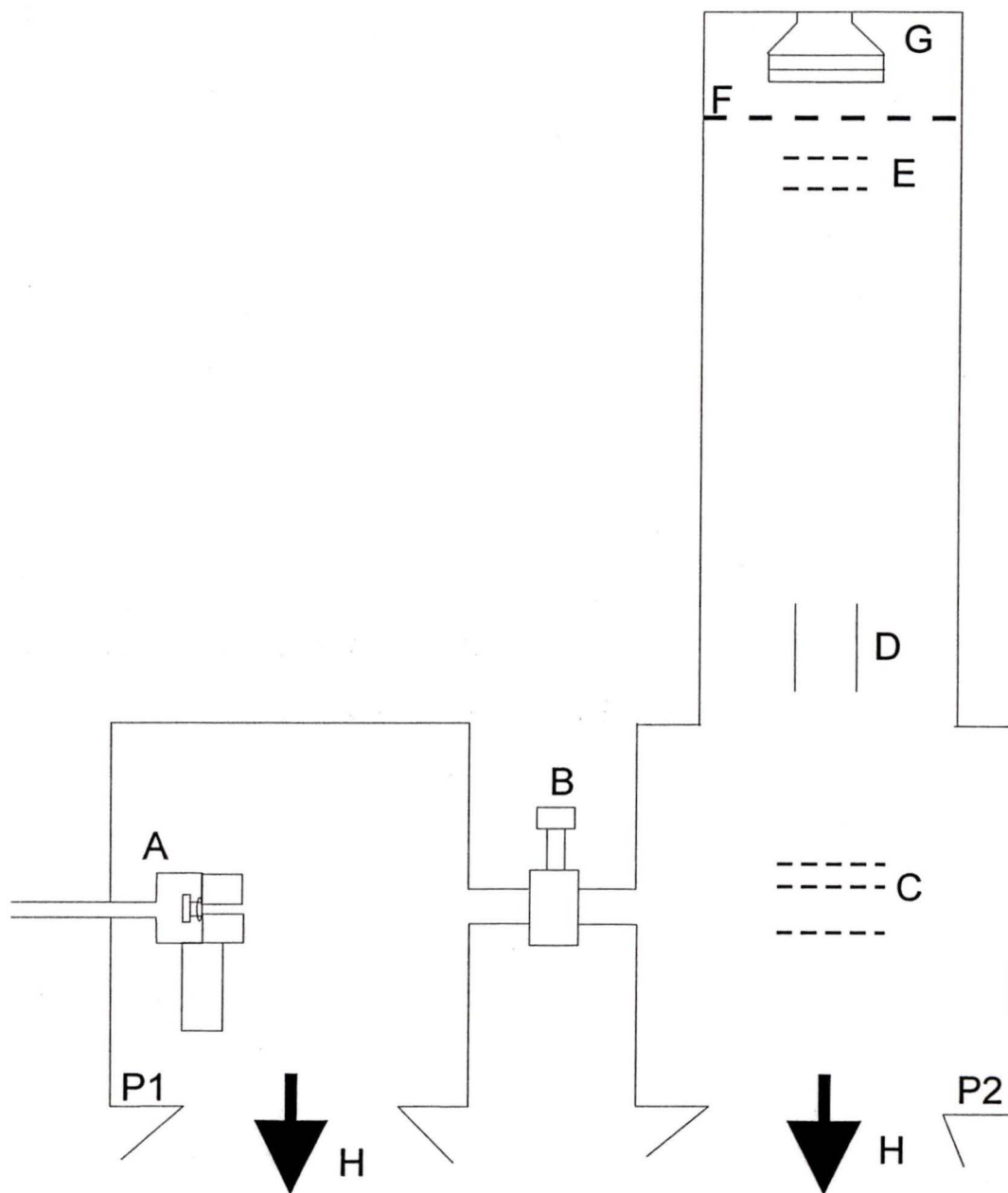
This chapter describes technical details of generation, separation and analysis of anions, cations or neutral particles of transition metal chlorides and transition metal sulfides. The order in which the following sections are presented is meant to reflect the “flow of information”. In this sense, it begins with the vacuum system, followed by the sample preparation and beam source, continuing with the lasers and optics, followed by the TOF-mass spectrometer and the mass gate. The high voltage switches used for the TOF-mass spectra, the mass gate and the timing and triggering of the system will be shown next. The signal sampling by the oscilloscope, and the data accumulation and manipulation by the data acquisition computer are at the end of this chapter.

Figure 2.1 provides an overview sketch of the experimental setup.

2.1 The Vacuum System

The vacuum environments in which the molecular beam was formed and analyzed are two 30cm×30cm×30cm black anodized cubic aluminum chambers, connected by a stainless steel valve (MDC, KGV-1500V). Each of the two chambers is evacuated by a diffusion pump (Edwards, Diffstak 250; 2300L/s). Each of the diffusion pumps is backed by a two-stage rotary pump (Edwards E2M 28, 10L/s). The pressure in the source chamber was maintained at 10^{-4} mbar during the experiment. The mass spectrometer chamber was maintained at 10^{-6}

Figure 2.1 Experimental Setup: A. beam source; B. valve connecting two chamber; C. TOF MS grids; D. deflector; E. mass gate; F. shielding grid; G. ion detector; H. to diffusion pumps; P1. Source chamber; P2. Mass Spectrum chamber



mbar. The chamber pressure was monitored using two ion gauges (Granville-Phillips, 274012 ion gauge and controller) combined with two thermocouple gauges (Granville-Phillips, 270006), while the backing pressure was monitored using a thermocouple pressure gauge of the same type. The two thermocouples were used to monitor the pressure when the vacuum was still low ($>10^{-4}$ Torr); as the vacuum went lower than 10^{-4} mbar, the ion gauges were turned on to monitor the pressure of the two chambers.

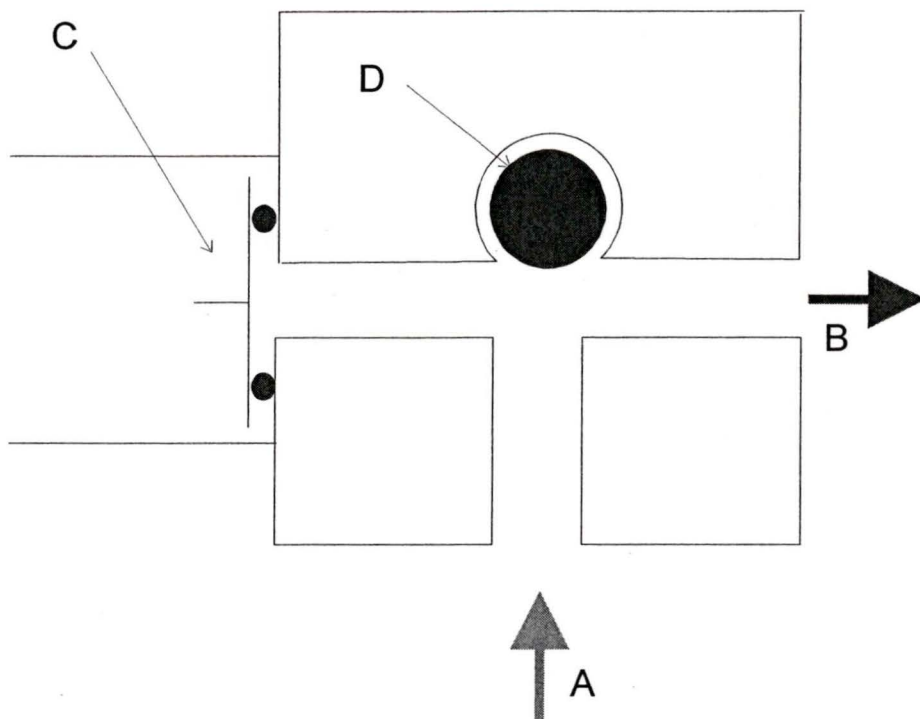
2.2 Molecular Beam Source

The beam source is sketched in Figure 2.2.

2.2.1 Sample Gas

In order to study the spectroscopy of negatively charged clusters, a sufficiently cold and intense negatively charged cluster beam is needed. Due to the electron attachment energy, negatively charged cluster ions can carry substantial internal energies and are more difficult to cool down, compared with neutral clusters. To minimize this problem, a pulsed molecular beam was formed by expanding a high-pressure sample gas into a high vacuum chamber through a homemade pulsed valve. As the gas passes the orifice of the valve and the small reaction chamber for laser ablation (section 2.2.3), it receives collisions from neighboring molecules. The gas molecules and the clusters generated in the small reaction chamber are then carried into the high vacuum chamber by the sample gas. Eventually the gas density falls so low that collisions are no longer possible.

Figure 2.2 Molecular beam laser vaporization source.
A: vaporization laser; B: molecular beam; C: piezoelectric valve;
D: rotating-translating metal rod.



The molecular beam provides a limited volume that contains gaseous molecules with a high density, a narrow velocity spread, and a low temperature.

More important to the present experiments is the fact that the molecular beam ensures a rapid cooling of the highly ionized plasma, which is formed during laser heating of a piece of metal, to create the clusters of interest.

Different gases were seeded in the helium carrier gas in order to make species of interest. Chlorine gas was used to form metal chlorides, while hydrogen sulfide gas was used to form metal sulfides. The sample gases are normally seeded in small concentration (2% ~ 10%) in pure helium at a total pressure of three bars.

The container of the gas is a 50 liter steel cylinder with two outlets, one of which is connected to a gas preparing system and another to the pulsed molecular beam valve.

The concentration of the sample gas has a significant effect on the generation of charged or neutral clusters. High gas concentration results in the favorable production of larger clusters. However, the concentration of the sample gas should be kept not higher than 10% in helium.

2.2.2 The Molecular Beam Valve

Within the vacuum chamber there is a molecular beam valve connected to the external gas supply through a Teflon tube. The pulsed molecular beam valve was designed following the description of Proch and Trickl [51]. A piezoelectric disk translator (Physik Instrument, P286.20) is driven by a homemade pulsed power supply in order to move an aluminum piston surrounded by diluted carrier gas. The tip of this piston is sealed with a rubber O-ring from a 0.5cm aperture. The valve can be opened (by lifting the piston) for an adjustable period of time so that the sample gas is able to expand into the vacuum chamber, and cool down to a lower temperature. The pulsed power supply allows for adjustment of the opening of the valve through the driving voltage (up to 800V, but usually under 300V), the pulse duration ($\sim 200\mu\text{s}$), and the timing of the molecular beam pulse.

The pulse duration and the driving voltage largely determine the molecular beam conditions. A high voltage leads to large amplitude motion of the piezocrystal, and therefore a large gas throughput. However, high driving

voltages also cause excessive strain on the disk, and possible damage. Long pulse duration increases the load on the diffusion pump and therefore increases the pressure in the vacuum chamber, without increasing the density of the clusters generated in the beam, but increasing the beam temperature slightly. On the other hand, if the pulse duration is too short, there is not enough time for the aluminum piston to respond fully to form a good molecular beam.

A critical factor is timing, that is, when the valve is triggered to open. The high temperature plasma generated by the ablation laser on the metal rod must fully intercept the pulsed sample gas expanded through the valve, so that the hot metal plasma can react with the sample gas to form the charged or neutral clusters. Typically, the pulse width sent to the nozzle was 200 μs . Since the valve itself has a mechanical response time for the trigger (possibly several hundred μs), the trigger to the lamp of the laser was sent about 200 μs later, and triggered the Q-switch of the laser about 500 μs later, than the valve trigger. Details of the timing and triggering of the system will be discussed later (Section 2.9).

2.2.3 The Reaction Chamber

The reaction chamber (part A in Figure 2.1) attached to the valve is where the laser ablation takes place, and this is where the hot plasma generated by the laser reacts with the sample gas to form different kinds of clusters. It has three mutually perpendicular channels. The main channel (2mm in diameter, 17mm or 25mm long, immediately beside the valve) allows the sample gas to flow from the valve to the vacuum chamber. The physical dimension of this channel is critical

to the species produced as a result of the reaction between the metal vapor and the sample gas. A longer channel (25mm) produced higher mass clusters and a shorter channel produced smaller clusters. The second channel, with a larger dimension ($d = 5.5\text{mm}$), allows for insertion of a metal rod (5mm in diameter). This channel lies 13mm from the valve and is exposed to both the main channel and a third channel. The third channel allows the vaporization laser to strike the metal rod placed in the second channel.

2.2.4 Metal rods

Metal vapor was produced in the reaction chamber by laser ablation of a suitable metal rod. The reaction of the sample gas with the metal vapor yields the clusters of interest. Figure 2.2 shows the cross section of the reaction chamber where the metal vapor is produced. In the experiments, rods made from different kinds of materials: carbon, Al, Ti, Cr, Fe, Co, Ni, Cu, Zn, Zr were used. These rods were all 39mm long \times 5mm diameter, and were placed in the path of the ablation laser. Driven by a stepping motor, the rod rotates and translates continuously during the experiment to expose a fresh area of surface. When the motor stops turning, a few laser shots was enough to drill a hole through the rod. The ablated area of the rod was also exposed to the main channel through which the sample gas was expanded and mixed with the plasma.

2.3 Lasers and Optics

The second harmonic (532nm) output of a Nd: YAG laser (Continuum NY61) is used as the vaporization source. There are two reasons to use the second harmonic of the YAG laser: 1) for safety reasons, the IR fundamental (1064nm) was not used; 2) the second harmonic (532nm) was used instead of the third harmonic (355nm) because the former provides sufficient energy to vaporize even the most refractory metals.

The second harmonic output at 532nm is generated using a "SHG Type II" KDP crystal. The power at 532nm can be reduced continuously, without a significant change in beam alignment or beam quality, by slightly misaligning the SHG crystal. The ablation energy significantly affects the generation and detection of the clusters. A laser pulse with higher energy gives slightly smaller clusters, and a slightly faster flying speed of the clusters generated. The delay time of the high voltage for the TOF Mass spectra (see below, section 2.4) has to be varied accordingly. The laser beam, about 8ns duration (FWHM), is focused onto the rod using a convex (converging) lens (f.l. = 50cm). The arrival time of the laser pulse compared to the pulsed molecular beam valve, is carefully adjusted in order to allow for optimum product yield.

2.4 Time of Flight Mass Spectrometer

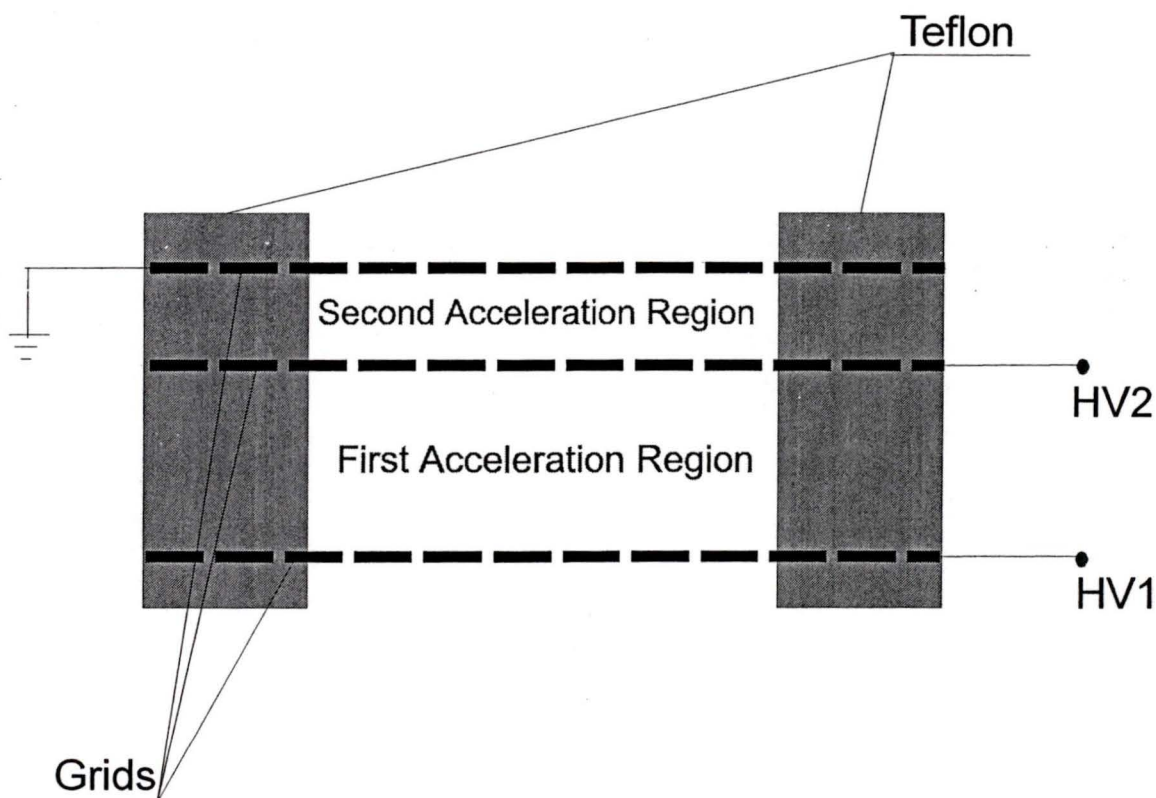
2.4.1 TOF Mass Spectrometer

Figure 2.3 is a sketch of the TOF MS used.

The Time of Flight (TOF) Spectrometer is connected next to the source chamber. The details of the TOF technique will be discussed further in Chapter 4.

The TOF drift region is perpendicular to the original flying direction of the clusters. The charged clusters (neutral clusters will be ionized by a second laser) were mass selected, and their spatial distribution was mapped using a self-designed TOF-MS of the Wiley-McLaren type [52]. Three stainless steel grids (Unique Wire Weaving Co. Inc., 95% transmittance, 25 μ m diameter) were

Figure 2.3: The TOF mass spectrometer ion repeller setup



mounted parallel to the direction of the molecular beam, in order to generate two acceleration regions perpendicular to the original flying direction of the clusters. The grids were mounted on a Teflon (diam. 72mm) frame at spaces of 20 mm and 10mm for the first and second fields, respectively.

For negatively charged clusters, an adjustable pulsed negative voltage $-1000\text{ V} \sim -1500\text{ V}$ was applied to the first grid of the repeller, with respect to the third repeller at ground. The voltage distribution between the first and second acceleration region was adjustable through a set of adjustable resistors. The voltage distribution between the two regions can be adjusted from 1:5.4 to 1:11.8; the pulsed voltage on the second grid varies from -844 V to -922 V for -1000 V on the first grid, or -1266 V to -1383 V for -1500 V on the first grid. The voltage on the second grid was adjusted to achieve the best space focusing conditions. Pulsed voltage was used instead of a constant voltage. In a constant electrical field, the charged particles will never reach the acceleration region due to electrostatic exclusion. The electrical field was zero before the charged particles reach the acceleration region. When the particles of interest reach the acceleration region, the high voltage was turned on in order to introduce the electronic acceleration field. This allowed the repelling and space focusing of those particles.

For positively charged clusters, a pulsed positive voltage of $+1000\text{ V}$ to $+1500\text{ V}$ was applied to the first grid of the repeller, with respect to the third repeller at ground. The voltage distribution between the first and second acceleration region (separated by the second grid) was adjustable through a set of adjustable resistors. The voltage distribution between the two regions can be adjusted from 1:5.4 to 1:11.8; voltage on the second grid varied from 844 V to 922 V for 1000 V on the first grid, or 1266 V to 1383 V for 1500 V on the first grid.

The same voltage settings were used for the neutral clusters except a constant electrical field is used. Since the neutral particles contain no electronic charges, they will not be affected by the electrical field and will reach the acceleration region. However, a second laser (Infinity 40-100) is required to ionize these neutral particles (so that they can be accelerated by the field) in the middle of the first acceleration region.

2.4.2 High Voltage switch setups for the Repeller

Figure 2.4.1 and 2.4.2 show the high voltage switches used for the repeller.

A fast high voltage transistor switch (BETHLKE HTS 31, $V_{o(max)} = 3 \text{ kV}$, $I_{p(max)} = 30 \text{ A}$) was used to generate the high voltage pulsed electronic fields.

For negatively charged clusters (Figure 2.4.1), the negatively signed pin on the switch was used for the input voltage ($-1000 \text{ V} \sim -1500 \text{ V}$), and the positively signed pin on the switch was used as the output (a pulsed voltage of $-1000 \text{ V} \sim -1500 \text{ V}$, depending on the input voltage). The input voltage was grounded with a $100\mu\text{F}$ capacitor in order to protect the faster high voltage switch. The output voltage was distributed to the grids of the repeller through a set of resistors. The switch was triggered by channel A of the EG&G delay box (discussed later). As the switch received a trigger from the EG&G delay box, the negatively signed pin and the positively signed pin of the switch were connected inside the switch. The input high voltage was then introduced to the output, and the electrical field was generated. When the trigger stopped, the negatively signed pin and the positively signed pin of the switchboard were disconnected, and the output voltage dropped

Figure 2.4.1: The circuit used to repel negatively charged clusters

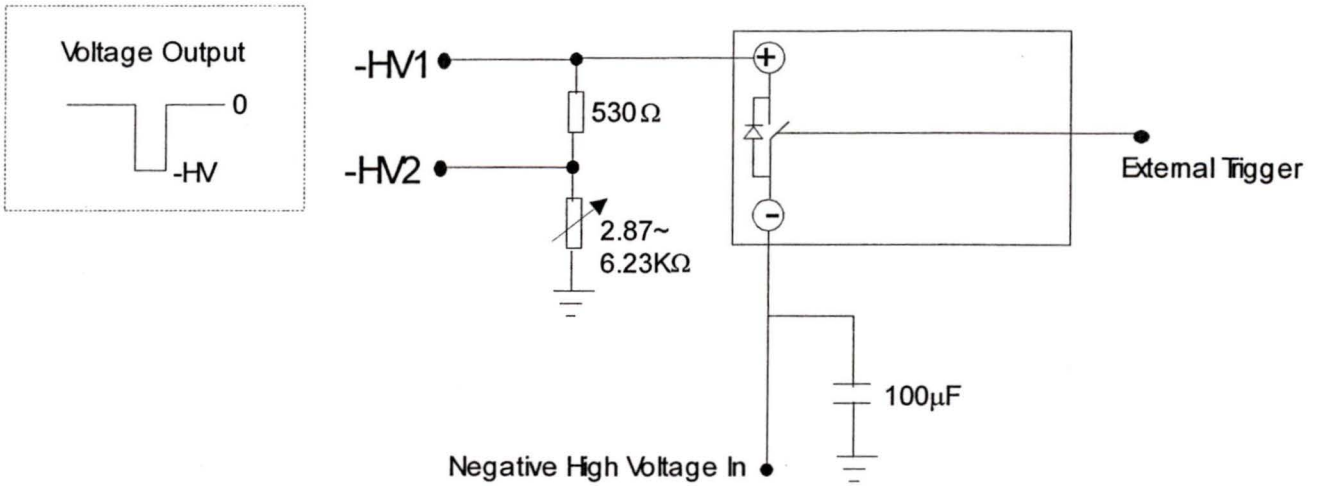
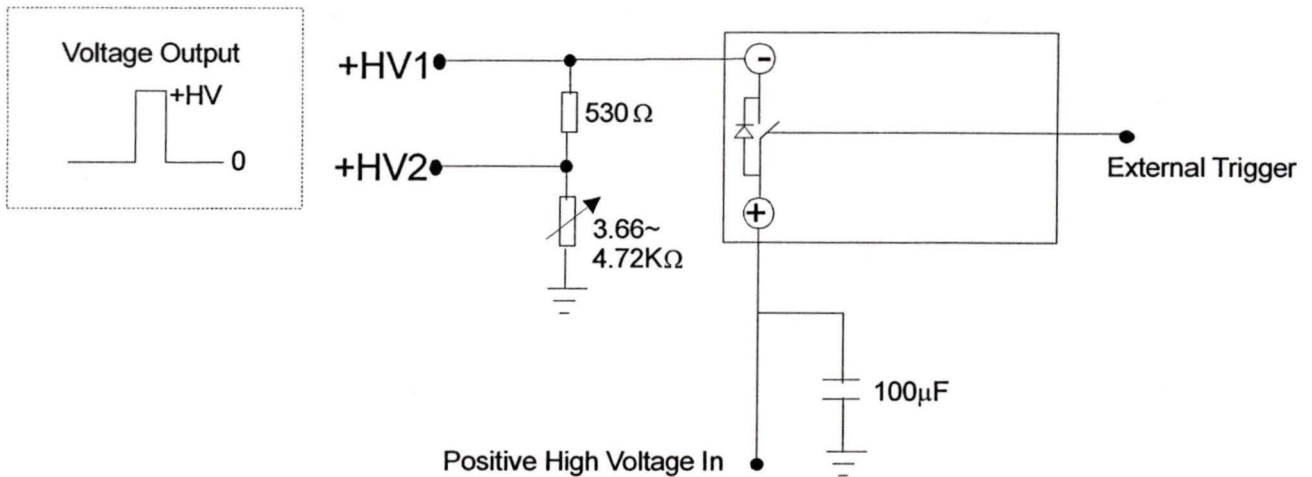


Figure 2.4.2: The circuit used to repel positively charged clusters



back to ground. A more detailed discussion of the timing and triggering of the system can be found in section 2.9.

The setup of the switch for positively charged clusters was similar (see Figure 2.4.2), except for the positively signed pin on the switch for the input voltage (1000V ~ 1500V), and the negatively signed pin for the output which will be a pulsed voltage of 1000V ~ 1500V, depending on the input voltage.

A 5V power supply was used for this high voltage switch.

2.5 the Ion Deflector

Above the repeller was a 90cm long TOF drift region, followed by a detector. A deflector was incorporated within the TOF drift region, about 22cm above the repeller. Although the charged clusters were repelled upward by the repeller, the clusters still have an original speed from left to right. This makes the trajectory of these repelled clusters to the detector indirect, with several degrees of deflection off axis. The deflector enabled one to adjust the trajectory of the cluster ions and ensure that they fall directly on to the detector. The deflector is produced an electrical field perpendicular to the TOF drift region. Two aluminum plates (4.5cm×8cm) were used for this reflector. The right grid is always grounded. Depending on whether the cluster is positive or negative, the voltage on the left grid was either negative or positive, respectively, and varies from 0V to ± 10 V in order to produce the best spectrum.

2.6 the Mass Gate

The mass gate was placed about 20cm below the detector. Charged clusters were mass selected and their spatial distributions mapped by the repeller, different cluster ions with different masses were deflected to the detector with different speeds. A mass gate is inserted between the repeller and the detector. Since cluster ions with different mass move with different speeds, they reach the mass gate at different times. The time differences of microseconds are typical.

Figure 2.5 shows the mass gate and Figure 2.6 illustrates the circuit setup.

The mass gate contains three stainless steel grids (Unique Wire Weaving Co. Inc., 95% transmittance, 25 μm diameter) perpendicular to the flying direction of the clusters. They are mounted on a Teflon (diam. 72 mm) frame with 15 mm spaces. Another fast high voltage transistor switch (BETHLKE HTS 31, $V_{o(\text{max})} = 3$ kV, $I_{p(\text{max})} = 30$ A) was used to generate a pulsed high voltage on the middle grid relative to the first and third grids held at ground potential.

The pulsed voltage on the middle grid is either negative or positive, depending upon whether the ions are positive or negative. The mass gate generates a pulsed electronic field that will block the cluster ions that reach the mass gate at particular times. Since the mass gate must "open" or "close" at particular times, according to the time the clusters reach the gate, channel B of the EG&G board is used to generate the trigger for the mass gate switch (detailed timing and triggering information will be provided later).

Consider how the mass gate was used to select negatively charged clusters. In order to select one particular cluster mass, the middle grid of the mass gate is held at a negative high voltage (-1000 V ~ -1500 V). Clusters that reach the mass gate during this time window will be pushed back. At a particular time, the clusters with a selected mass reached the mass gate, the high voltage switch is triggered. During the trigger time, the voltage on the middle grid would drop to zero, which eliminated the opposing electronic fields on the mass gate and allowed the cluster to pass the mass gate. The time duration of the trigger is adjustable, enabling a variable time windows, and was set long enough to pass a particular cluster mass. After the trigger, the voltage on the middle grid returned

Figure 2.5: The mass gate setup

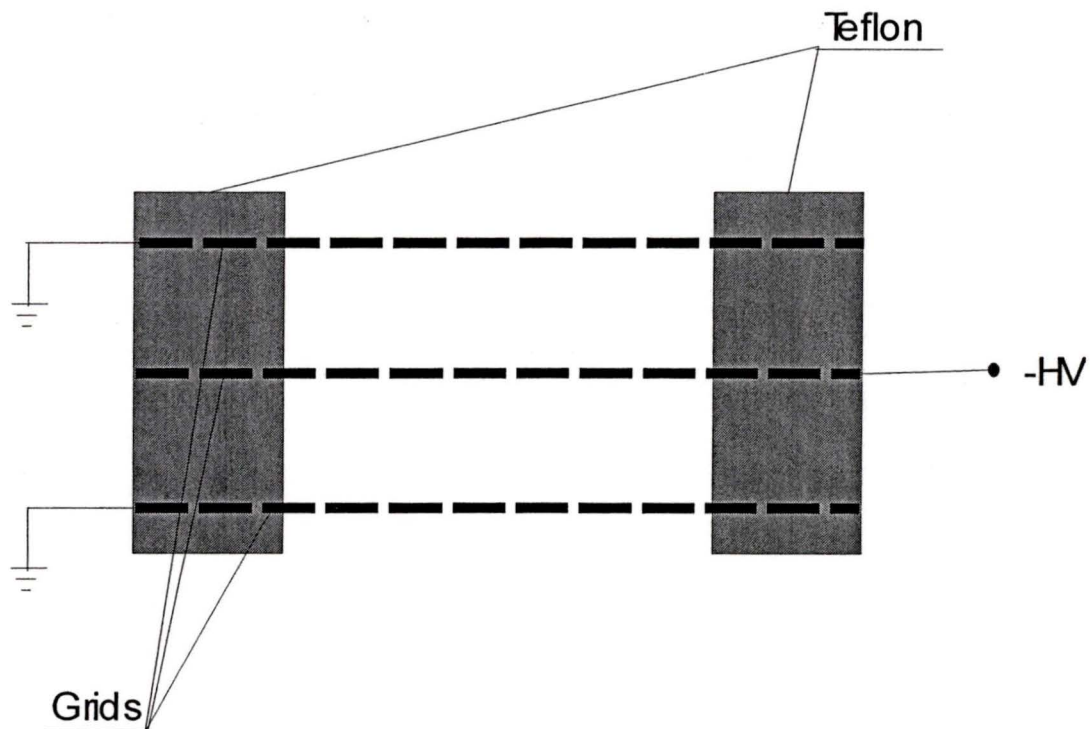
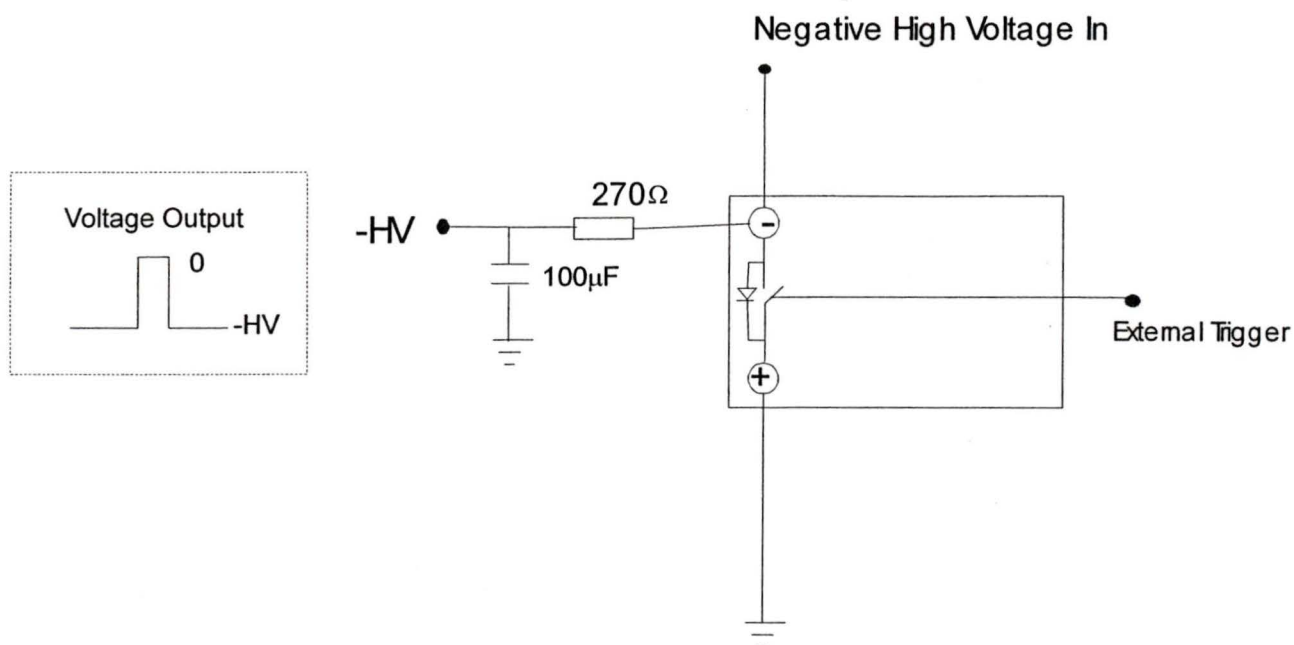


Figure 2.6 The circuit used by mass gate for negatively charged clusters



to the original high voltage, and the mass gate is “closed”. Clusters with higher mass that arrived later will also be blocked.

A detailed discussion of the performance of the mass gate can be found in Chapter 6.

2.7 Detection of negative ions, positive ions and neutral particles

2.7.1 Detection of positive ions and neutral particles

Since neutral particles are ionized in the acceleration region of the TOF-MS, the detection of positive ions and neutral particles are the same. Figure 2.7.1 is a sketch of the detection system for positive ions.

The ion detector consisted of two microchannel plates (MCP); impedance matched to 50Ω (channel diameter 10μm, 12μm spacing between centers). There is an ion screen set at ground voltage in front of the MCP. A high negative

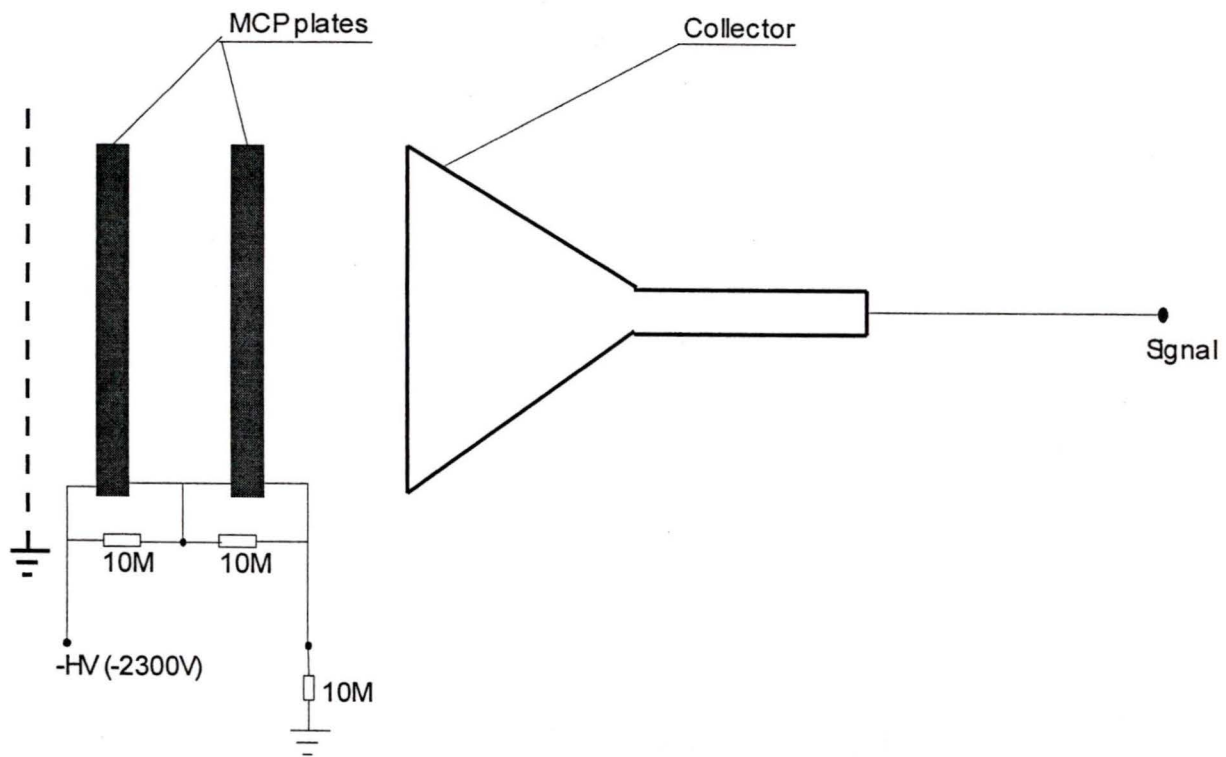


Figure 2.7.1: Setup and circuit to detect positively charged clusters

voltage (-1800V ~ -2300V) was applied to the bottom surface of the first microchannel plate. The voltage of the other surface of the MCP and the first surface of the second MCP were held the same at two-thirds of the original voltage. The last surface of the second MCP was set to one-third of the original voltage and was connected to the ground through a 10M Ω resistor.

An incoming positive ion induced a cascade of electrons falling through this field and leading to a measurable current. This current led to a voltage pulse of approximately 1mV per ion, in the case of a typical ion kinetic energy of 2keV. The recovery time per channel was not specified by the manufacturer, but was clearly shorter than 100ms and therefore influenced only the strongest signals. In all experiments the ion density on the MCP (max. 10⁴ cm⁻²) was small compared to the number of available microchannels (min. 10⁶ cm⁻²). Saturation effects were therefore not observed. The outgoing signals were then digitized with an oscilloscope for further data processing.

2.7.2 Detection of negative ions

Figure 2.7.2 shows the circuit used to detect negative ions.

In order to detect negative ions, the entrance screen was grounded. The last surface of the second MCP was set to 1800V ~2300V, the mid two surfaces of the MCP were set to two-thirds of the original voltage, and the first surface of the first MCP (next to the entrance screen) was set to one-third of the original voltage and was connected to ground through a 10M Ω resistor. The collector, located

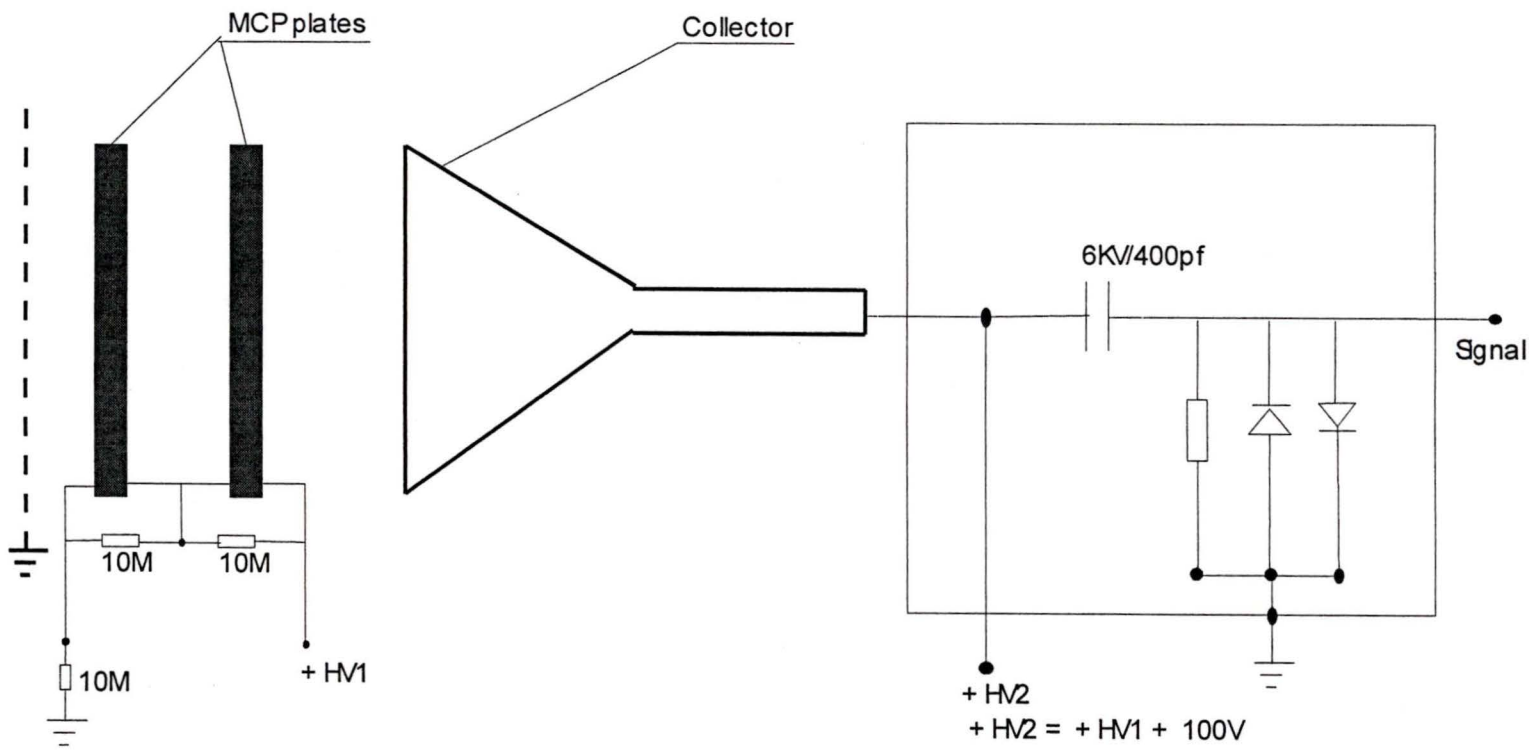


Figure 2.7.2: Setup and circuit to detect negatively charged clusters

directly behind the two MCPs, was set to 100 V higher than the voltage on the last surface of the second MCP.

An incoming negative ion induced a cascade of electrons falling through this field as well. The voltage pulse was generated on a static voltage of 1900 V ~ 2400 V, the voltage to which the collector was originally set. The signal from such a high voltage is too large for the oscilloscope. A signal pick-up circuit was designed as shown also in Figure 2.7.2. The incoming signals (the ac part of the voltage, variable from 0V to no more than 1 V) were passed to the oscilloscope through capacitor C1. The static part of the voltage was rejected by the capacitor. The 15 k Ω resistor and the two diodes were used to protect the oscilloscope from the voltage drop on the collector, which is both too high and too fast for the oscilloscope. However, the protection offered through the diodes and resistor is limited. If the change of the high voltage on the collector is too fast or has too big a variation (out of the range that the diodes can protect), the high voltage change will certainly be passed to the scope as a signal and will damage the oscilloscope. Therefore, changes in the high voltage on the collector must occur slowly. The voltage of the power supply must be slowly decreased to zero before the power supply can be turned off. Before the signal goes to the oscilloscope, it was side grounded with a 50 Ω resistor in order to match the input impedance of the scope.

2.7.3 Shielding of the detector

There are two larger microwave sources within the system (the repeller and the mass gate), and the detector reacts like an antenna to these noise source, The detector must therefore be shielded from these two sources. A grounded aluminum plate (3mm thick, with the same diameter as the TOF drift chamber) with several holes (3cm in diameter) was placed between the TOF drifting region and the detector. The entire system was also grounded by a connection to the water line of the Petch building during the experiment. This shielding was not perfect, but it was adequate for this study.

2.8 The oscilloscope

The signal from the microchannel plate detector was directed to a digital oscilloscope (Tektronics 2440; 500MHz) for acquisition and basic manipulation. The oscilloscope could acquire and digitize input signals in different ways. The instrument has two input channels that can be set differently for deflection, input resistance, and coupling. Calibrated deflection factors were available in a 1-2-5 sequence from 2 mV to 5 V per division. Input resistance could be set to 1 M Ω or 50 Ω , and coupling can be AC (only if resistance is 1 M Ω), DC, or ground. In all experiments the coupling was set to DC and the input resistance to 50 Ω in order to match the impedance of the MCP detector. This was necessary for transmitting a fast signal.

The acquisition rate can be selected in a 1-2-5 sequence between 2ns to 5s per channel. During the experiment, this was adjusted from 100ns/division to

5 μ s/division, depending upon the signal shape, the resolution and the number of mass peaks included in one data file. The smaller the time per channel, the higher the resolution for each mass peak, and the fewer the number of mass peaks that can be included in one file. Each mass peak (signal) on the scope is related purely to the time sequence of the interrelated cluster ions as they reach the detector. The smaller the time division, the narrower the range of the arrival time for those clusters captured by the detector.

The oscilloscope was triggered by a 5V external signal from channel A of the EG&G delay box. The oscilloscope and the repeller for the TOF_MS was triggered at the same time by the same channel of the EG&G board. Therefore, the delay time from “trigger zero” to the actual sampling interval could be adjusted to match the flight time of the cluster ions (the time they spend on the way from the repeller to the detector) for the respective experimental conditions. While the time resolution is 2 ns between points, the voltage resolution was determined by the 8 bit A/D converter to be $\sim 1/250$ of the full deflection, i.e., 80 μ V at the minimum deflection of 2 mV/div.

The instrument allowed for averaging of consecutive waveforms in order to improve the signal to noise ratio. However, this feature was only used when optimizing the laser alignment and not during data collection. The general purpose interface bus (GPIB) (National Instruments NI 488.2) allowed for fast data transfer from the oscilloscope to the data acquisition computer (Powerwave, 386 PC 25MHz). The GPIB was set to the “Fast transit” mode in order to load the acquired waveform at the highest possible rate. When in “normal mode” the

oscilloscope was waiting for a request from the computer before starting to send the waveform, whereas the "Fast transmit" mode worked in an "acquire-transmit-rearm" sequence. Since the number of requested waveforms was given in a single command at the beginning of each sequence, and the oscilloscope did not "listen" to the computer before the last waveform was transmitted, there was very little dead time between acquisitions. In this way the acquisition rate for a large number of waveforms could be greatly enhanced. Only by using the "Fast transmit" mode could the data acquisition, transmission, and some basic manipulations be done at the experimental pace of 10Hz.

2.9 Timing, triggering, computer interface and software

The data acquisition computer was a 386 / 25MHz IBM compatible PC, which was equipped with a GPIB board (National Instruments NI 488.2), a counter/timer card (Advantech Co. Ltd., PCL-830 with a Advanced Micro Devices chip, Am9513), an A/D converter board (Laboratory Technologies Corp., PCL-711S), one parallel port and one serial port. All these interfaces were manipulated via a suite of QuickBasic (QB) programs, which were written by Jianying Bob Cao, in order to automate the experiments. The interface layout is given in Figure 2.8.

The GPIB board was accessed via the QuickBasic driver (QBIB.COM), which was made accessible by a QuickBasic declaration file (QBDECL.BAS) at the beginning of each program. Similarly, the timer card was programmed via an assembly code software driver (PCL830.BIN). The timer card had a 1MHz on board timebase and 10 independent counters, which were used to trigger the

series of events. A separate QuickBasic program was written to modify the individual pulse widths and delay times (TIMER.BAS). The A/D converter board was accessed via a self-written assembly code driver (ADCONV.ASM).

Accurate timing and triggering was crucial to all experiments. Generally the master trigger frequency was defined by the clock of the timer/counter card and set to 10Hz. As shown schematically in Figure 2.9, the timer board triggered a series of events. The two ND:YAG laser lamps were triggered by channel 7 and 9 of the timer board, and the homemade nozzle delay generator by channel 8. However, the triggering of the Q-switch of the ablation laser, the oscilloscope, and the two high voltage switches needed to be very precise. This was done via a commercial four-channel delay generator (Princeton Research, EG&G 9650), which in turn was triggered by channel 3 of the timer board. The delay generator offered four independent and two dependent outgoing triggers, with variable delays in regard to the incoming trigger in the range of 0 to 100ms in the steps of 10ps. The jitter was specified by the manufacture as being $< (50\text{ps} + 10^{-8} \Delta t_{\text{delay}})$ for successive pulses.

As mentioned in the previous discussion, channel D of the EG&G board was used to trigger the Q-switch of the ablation laser, which was adjustable in order to produce the best yield of clusters. Channel D of the board can only give a positive trigger, but the Q-switch of the ablation laser can only be triggered by the falling edge of a negative 5V trigger. A negation circuit was constructed between the outgoing trigger of the board and the laser Q-switch.

Figure 2.8: Experimental interface layout. Single line: signal; Broad line: data; HVS: High Voltage Switch

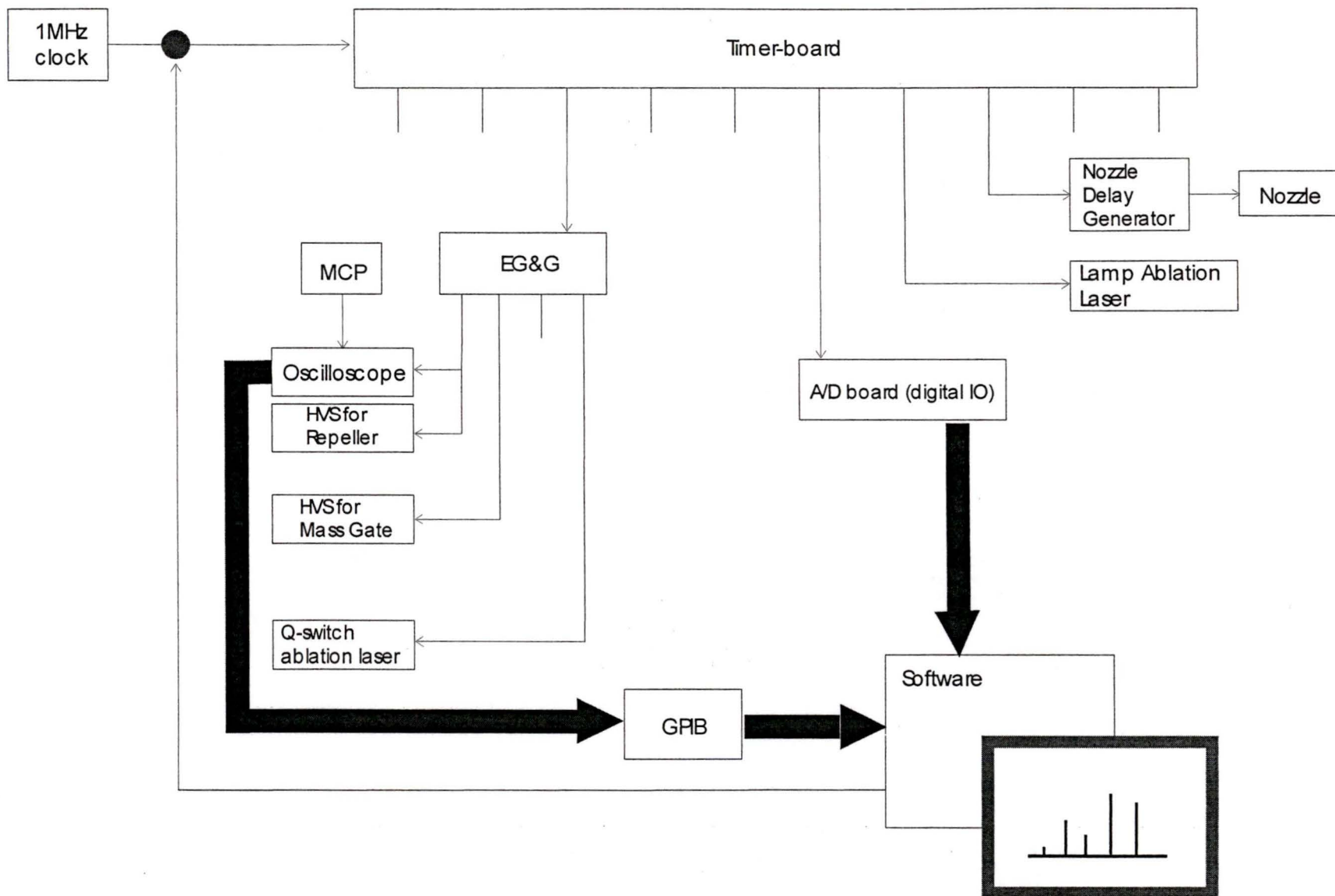
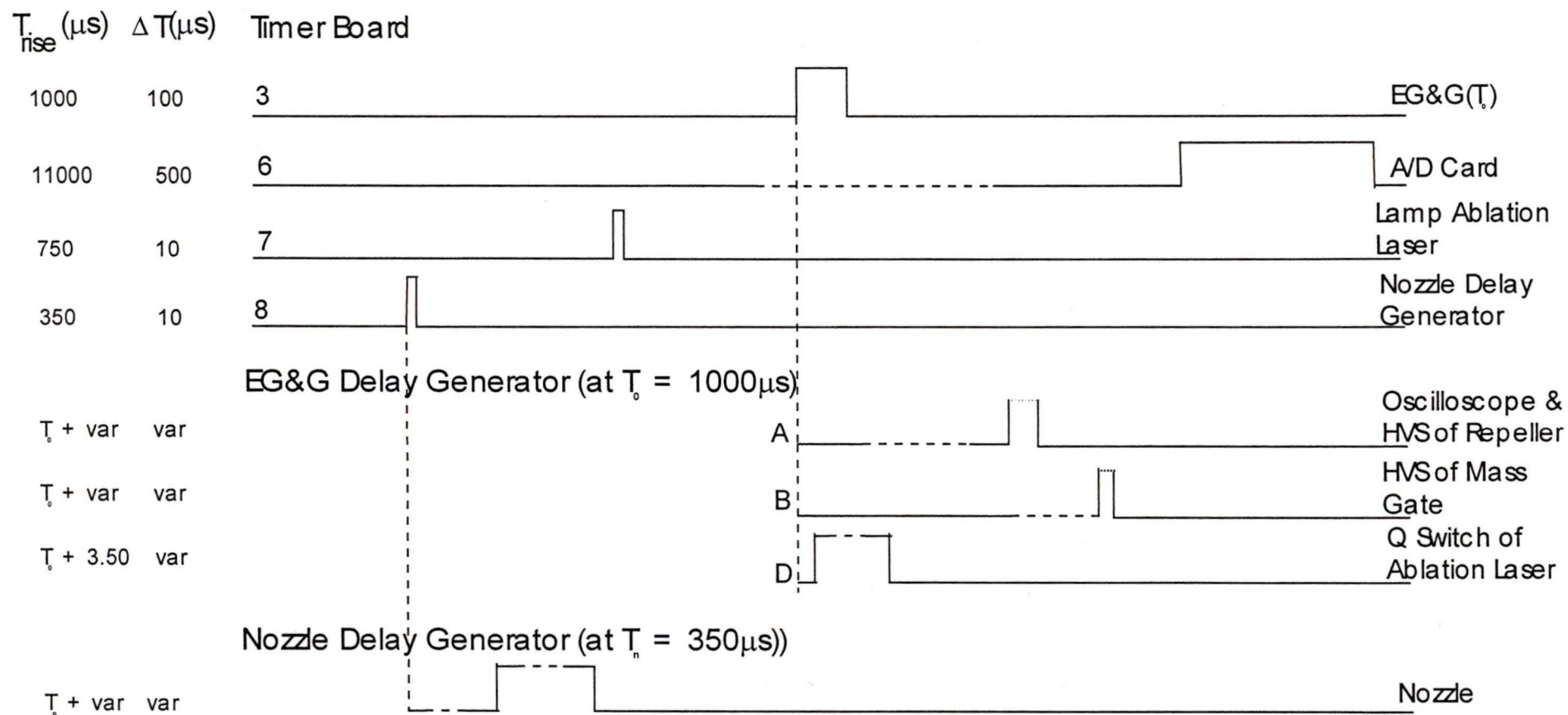


Figure 2.9: Diagram of the triggering sequence. HVS: High Voltage Switch



Channel A of the EG&G board was used to trigger both the oscilloscope and the repeller of the TOF-MS. By doing this, the flying time of the cluster ions can be followed by adjusting the delay time setting of the oscilloscope. The width of this trigger is approximately $3\mu\text{s} \sim 5\mu\text{s}$. It does not need to be precise, but it must be long enough to let all the cluster masses leave the two acceleration regions.

Channel B of the EG&G board was used to trigger the high voltage of the mass gate: both the delay and the trigger are different for each selected mass. The width of the trigger is very important. It must be long enough to let all the selected clusters pass the gate (Although the clusters with the desired single mass are space focused, they arrive at the mass gate at slightly different times, determined by the width of the mass peak). The trigger must be short enough so that only a selected cluster mass will pass the mass gate. By the time other mass clusters arrived, the mass gate is closed.

The experimental QB-programs performed tasks such as the sampling of the time of flight profiles at a fixed wavelengths, recording of TOF profiles at different wavelengths by scanning a probe laser, scanning of the photolysis laser while monitoring the integrated ion signal, and others. In the experiments for this thesis, only the first task was used.

2.10 Experimental Procedures

There are four crucial steps for the experiment.

Step One: Adjust the beam source in order to obtain the optimized yields of the cluster ions.

This step was completed by adjusting the delay and power of the ablation laser (the highest laser power doesn't necessarily produce the best yields), and adjusting the delay and width of the trigger to the nozzle. In this step, the delay time of the repeller and the data acquisition setting of the oscilloscope, might need adjustments in order to clear the signals. The signals are used to optimize the beam source condition.

Step two: Adjust the repeller of the TOF-MS in order to achieve the optimized signal and best space focusing condition.

This step was completed by first adjusting the delay time of the trigger (Channel A of the EG&G board) to the high voltage switch for the repeller, so that the best part of the original cluster beam will be selected by the repeller and sent to the detector. Next, the voltage setting of the two acceleration regions must be adjusted, in order to achieve the best space focusing condition of each mass peak. During the adjustment, the settings of the beam may need to be adjusted as well (step 1). Once completed, both the setting of the beam source and the setting of the repeller were fixed.

Step three: Adjust the deflector to get the best signal condition.

This step was completed by adjusting the voltage on the deflector in order to reduce velocity perpendicular to the TOF axis.

Step four: Adjust the mass gate (optional, only for those experiment that need to pick up only one cluster mass).

Using the arrival time of each cluster mass, the time that each cluster arrives at the mass gate for each of them can be calculated. This will be the delay time of the trigger (from Channel B of the EG&G board) to the high voltage switch of the mass gate. From the width of the mass peak, the duration time of each cluster mass needed to pass the mass gate can be calculated. This will be the width of the trigger. The trigger for the mass gate is set to those values just calculated, and adjusted to account for slight differences between the calculated values and the values actually being used. Once the adjustment for one singly massed peak is finished, the setting of the mass gate is fixed.

Each of the steps above needs an adjustment of the data acquisition setting of the oscilloscope in order to achieve the up-to-date best signal condition. Eventually, as the above steps are completed, the data acquisition setting of the oscilloscope needs to be adjusted once again in order to achieve the best signal condition.

Chapter 3: Characteristics of the Molecular Beam

This chapter describes the characteristics of the molecular beam generated by the laser ablation. The first part of the experiment was accomplished using a carbon rod, with pure helium as carrier gas. This system generated negative monoanionic clusters C_n^- . The length of the molecular beam was studied, with regard to the negatively charged clusters and the density distribution of the negatively charged clusters inside the molecular beam. The second part of the experiment was accomplished by using a Ti rod, with 4% Cl_2 in Helium as carrier gas. This system generated $TiCl_n^+$ and $TiCl_n^-$ clusters. A comparison of the density distribution and flying speed of the negatively charged and positively charged clusters in the original beam was carried out.

As mentioned in the previous chapter, the intensity of the mass signals collected from charged clusters is highly dependent on the trigger timing of the high voltage switch of the TOF repeller. The grids of the repeller are initially set to ground. When the trigger is applied, the grids established an electric field that repels the charged clusters currently at the grid position. Therefore, the length of the molecular beam can be studied by triggering the electric field at different times and collecting the intensity of the mass signal. In addition, after translating the time sequence of the triggers to a space sequence of the molecular beam, we can derive the density distribution of the charged clusters from the signal intensity collected at different parts in the space sequence of the original beam.

As negatively charged clusters are of most interest, the detailed discussion of the molecular beam characteristics is based on the negatively charged clusters. The results for neutral particles and positively charged clusters are presented as a comparison with the negatively charged clusters.

3.1 The Length of the Molecular Beam

As mentioned in the previous chapter, channel A of the EG&G board was used to trigger the high voltage switch of the repeller, and channel D of the EG&G board was used to trigger the ablation laser. The time the ablation laser was fired can be treated as the time the molecular beam was originally generated; therefore this time will be T_0 for defining the triggers for the HVS.

The delay time of channel D of the EG&G board was set to zero ($T_0 = 0$) for this experiment; therefore, the delay time of channel A will be exactly the delay time after the molecular beam was originally generated.

As shown in Figure 3.1, the head of the molecular beam can be captured by the repeller at $T_{dh} = 240 \mu s$ after the molecular beam is generated (Figure 3.1_a). The tail of the beam can be captured at $T_{dt} = 410 \mu s$ (Figure 3.1_b), and the maximum mass signals can be captured at delay time $T_{dm} = 350 \mu s$ (Figure 3.1_c). The flying distance of the molecular beam is $L_f = 76 \text{ cm}$ (the distance between the focusing point of the ablation laser and the repeller); therefore, the speed of the beam is approximately:

$$\begin{aligned} V_B &= L_f \div T_{dm} & (3.1) \\ &= 76 \text{ cm} \div 350 \mu s \end{aligned}$$

$$\approx 0.22 \text{ cm } \mu\text{s}^{-1}$$

As mentioned above, at the time the head and the tail of the beam arrived, the repeller was 240 μs and 410 μs . Therefore, the entire beam spent about:

$$T_d = T_{dh} - T_{dt} = 410 \mu\text{s} - 240 \mu\text{s} = 170 \mu\text{s} \quad (3.2)$$

Figure 3.1_a: TOF spectrum collected at a repeller delay of 240 μs

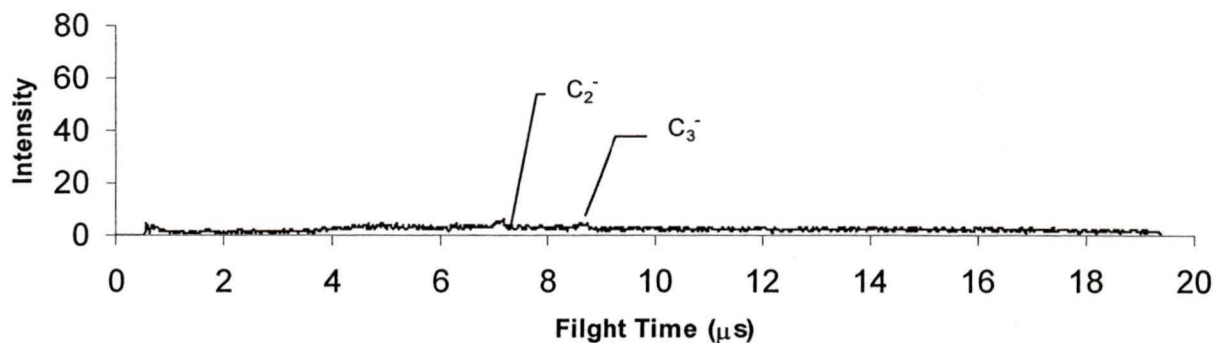


Figure 3.1_b: TOF spectrum collected at a repeller delay of 410 μs

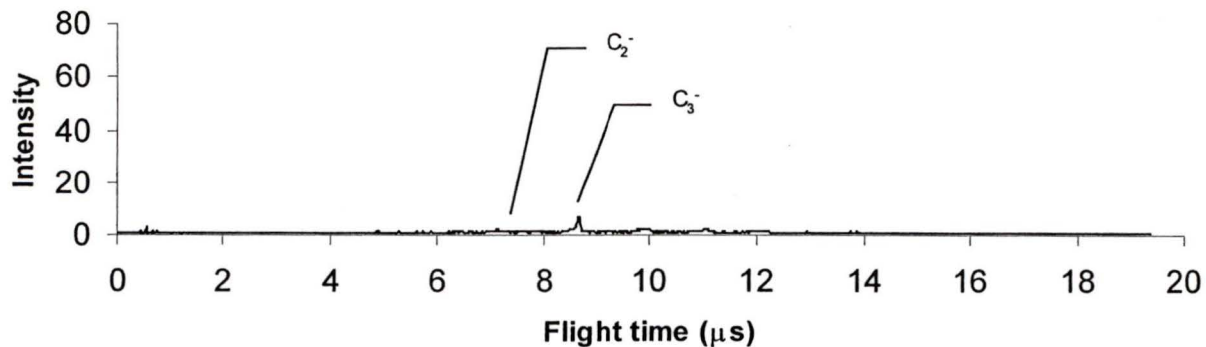
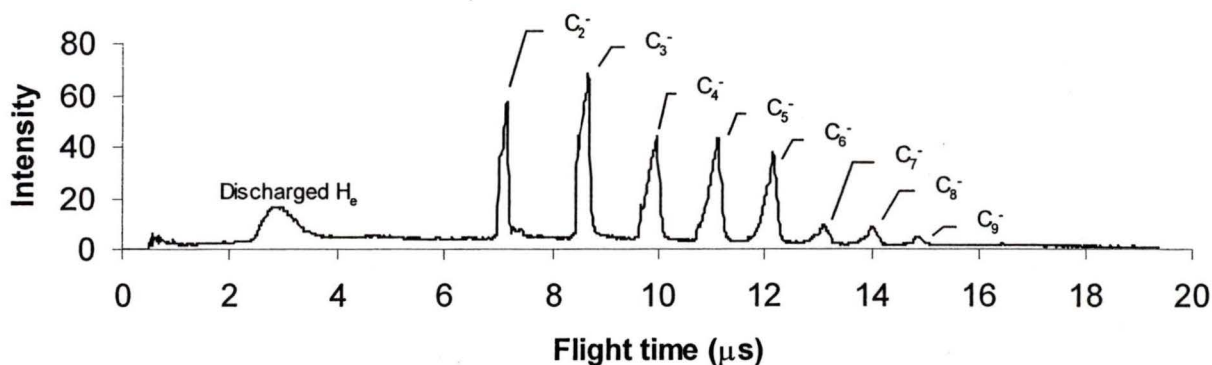


Figure 3.1_c: TOF spectrum collected at a repeller delay of 350 μs



to pass the repeller. This is reasonable since the pulse duration for the molecular beam valve was set to 180 μs for this experiment, which means the laser ablation product was exposed to the carrying gas for 180 μs .

The length of the molecular beam can then be calculated:

$$\begin{aligned}
 L_B &= T_d \times V_B & (3.3) \\
 &= 170 \mu\text{s} \times 0.22 \text{cm} \cdot \mu\text{s}^{-1} \\
 &\approx 37 \text{cm}
 \end{aligned}$$

Although the second chamber is kept under 10^{-6} Torr as the molecular beam passes the acceleration region, the local gas pressure at the acceleration region of the repeller can be high enough so that the voltage drop on the repeller will discharge the local gas. This is why, in Figure 3.1_c, there is a wide peak with a flight time of approximately 2.4 ~3.6 μs , which is the speed of helium negatively charged clusters. These are very difficult to remove, and they are impossible to

space focus. Fortunately, they come at the beginning of the spectra and will not affect the mass peaks that come later.

3.2 Density Distribution of the Negatively charged Clusters

By triggering the repeller at different delay times, and analysing the signal intensity collected, the density distribution of the negatively charged clusters in the molecular beam can be calculated.

If the origin of the coordinate system is set as the beginning of the molecular beam, then the space sequence (distance from the beginning of the beam) of the part at which the signal was collected from the original beam can be calculated as:

$$D_p = V_B \times (T_{dp} - T_{dh}) \quad (3.4)$$

Where V_B is the speed of the original beam, T_{dp} is the time sequence that the repeller was triggered in order to collect the proper signal, and T_{dh} is the time the beginning of the beam reached the repeller.

If the intensity of the signal collected at 350 μs for C_3^- (maximum intensity) was set to be 100, table 3.1 can be derived to present the density distribution of the negatively charged clusters. The density distribution of different negatively charged clusters was approximately the same: C_2^- and C_3^- were used for demonstration.

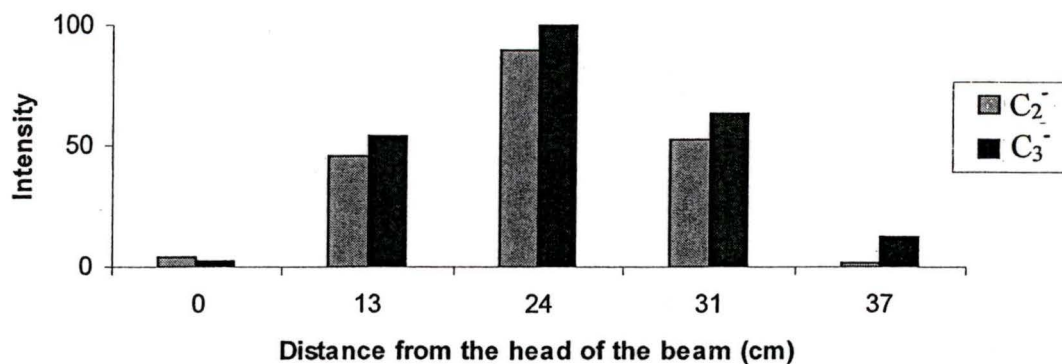
Figure 3.2 shows the density distribution of the two negatively charged clusters according to the data in table 3.1. From this Figure we can see that the maximum intensity is not at the center of the molecular beam but roughly in the range of

about 10 ~ 20% further along from the center. This information is crucial, since it establishes the timing that needed be used to obtain the maximum signal.

Table 3.1: The density Distribution of C_2^- and C_3^- in the Molecular Beam
Normalize to C_3^- Max = 100

Trigger (μ s)	Space Sequence (cm)	Intensity	
		C_2^-	C_3^-
240	0 (head)	4	2
300	13	46	55
350	24	85	100
380	31	53	63
410	37 (tail)	2	13

Figure 3.2: Density distribution of C_2^- and C_3^- in the molecular beam
(normalized to C_2^- max = 100)



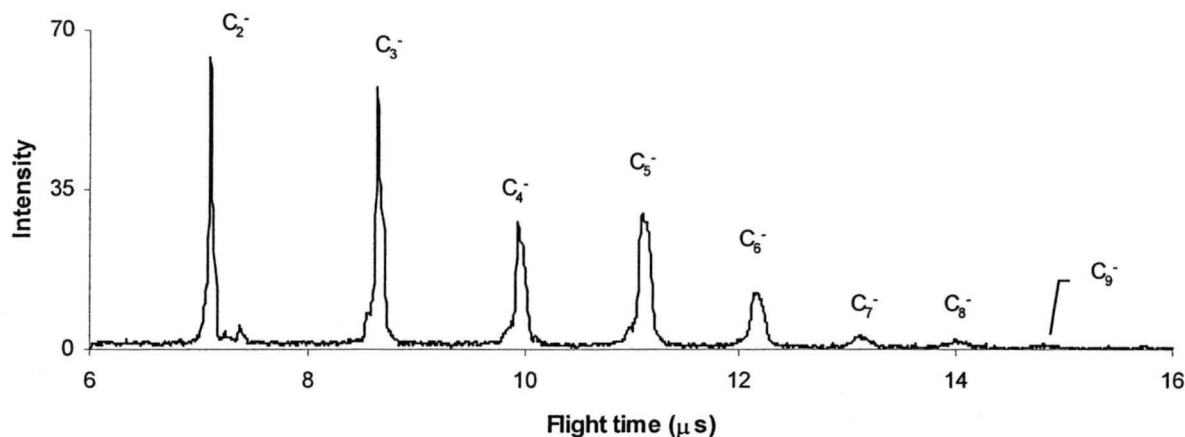
3.3 Molecular Beam Generated with Different Kinds of Beam Source

The intensity distribution of negatively charged carbon clusters detected from normal source varied slightly from time to time. Figure 3.3 shows the negatively charged carbon clusters detected through normal beam source (which is slightly different from figure 3.1_c), as was described in chapter 2. In this case, the delay of the trigger for the repeller is 350 μ s. The negatively charged clusters detected, along with their signal intensities, are given in Table 3.2.

Table 3.2 The negatively charged clusters collected from normal source

Negatively charged Clusters	Signal Intensity
C_2^-	100
C_3^-	90
C_4^-	43
C_5^-	47
C_6^-	20
C_7^-	5
C_8^-	3
C_9^-	1

Figure 3.3: Negatively charged clusters from normal source



C₂⁻ has the maximum signal intensity, and the largest negatively charged cluster that can be observed with this source is C₉⁻, which has a signal intensity of only 1.2% of the C₂⁻ cluster intensity.

Things are very different if a new reaction chamber is used. Figure 3.4 shows the shape of the new chamber. The difference between this chamber and the normal one is that the new chamber has a U-tube about 4cm long placed in front of the jet hole of the normal reaction chamber (shown in chapter 2). Figure 3.5_a shows the mass spectra collected using this setup; the clusters detected and their signal intensities are shown in Table 3.3. For comparison, the mass spectrum observed for C₂⁻ ~C₆⁻ under the same conditions were shown in Figure 3.5_b.

The differences between the clusters generated from the two sources can be clearly seen. The source with the U-tube generated bigger clusters. As the plasma species generated by laser ablation pass through the U-tube, they

undergo many more collisions with other plasma species; therefore, bigger clusters will be generated.

Table 3.3: The negatively charged clusters collected from source with the U-tube

Cluster Detected	Intensity
C_9^-	100
C_{10}^-	27
C_{11}^-	95
C_{12}^-	18
C_{13}^-	13
C_{14}^-	16
C_{15}^-	64

Figure 3.4: Molecular beam laser vaporization source.

A: vaporization laser; B: molecular beam; C: piezoelectric valve; D: rotating-translating metal tod; E: The U-tube.

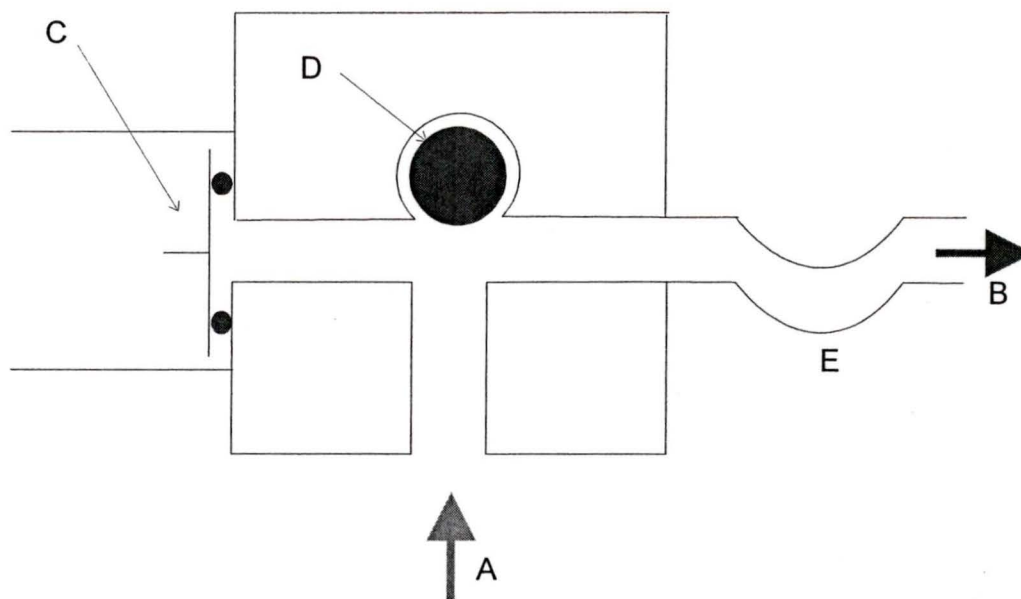


Figure 3.5_a: Negatively charged clusters obtained from source with U-tube. Flight time: 14~24 μ s

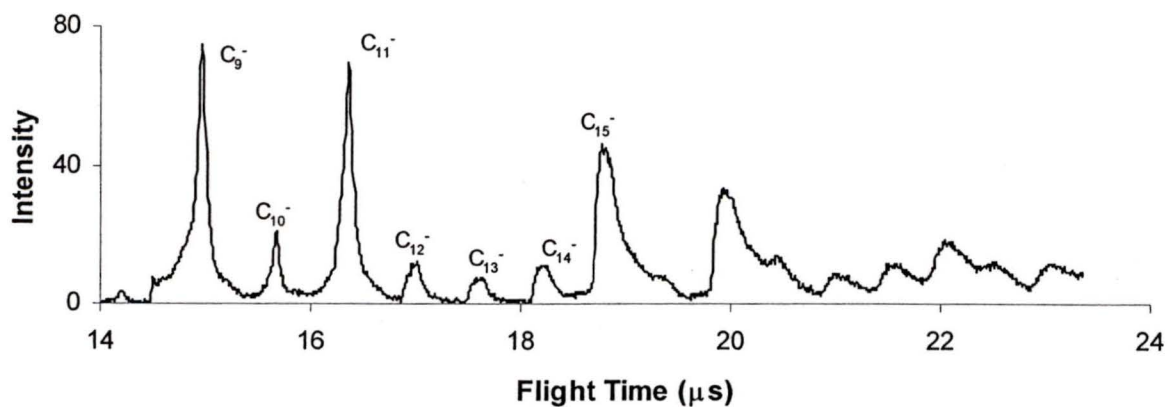
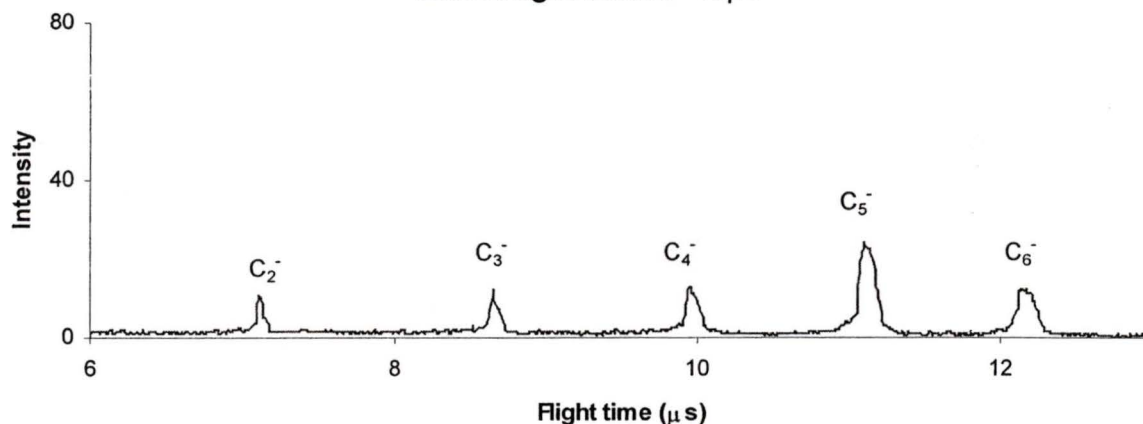


Figure3.5_b: Negatively charged clusters from the source with a U-tube. Flight time: 6~13 μ s



Due to the new source, another significant change concerning the molecular beam is its flying speed. As calculated in previous sections, the normal flying speed of the molecular beam is approximately $0.22 \text{ cm } \mu\text{s}^{-1}$. However, the speed for the molecular beam generated with the U-tube is

$$76 \text{ cm} \div 440 \mu\text{s} = 0.17 \text{ cm } \mu\text{s}^{-1}$$

which is 23% slower than the normal speed. This is due to the U-tube retarding the speed of the carrying gas.

The molecular beam generated from the U-tube source spent about $170 \mu\text{s}$ in order to pass the repeller, which is the same as the normal molecular beam. Therefore, the length of the molecular beam is about 29 cm. This indicates that the length of the molecular beam was controlled by the pulse duration of the beam valve, not by the shape of the reaction chamber. The speed of the molecular beam varies from time to time; it is highly dependent on the pressure of the carrying gas and the ablation laser power. However, what we were

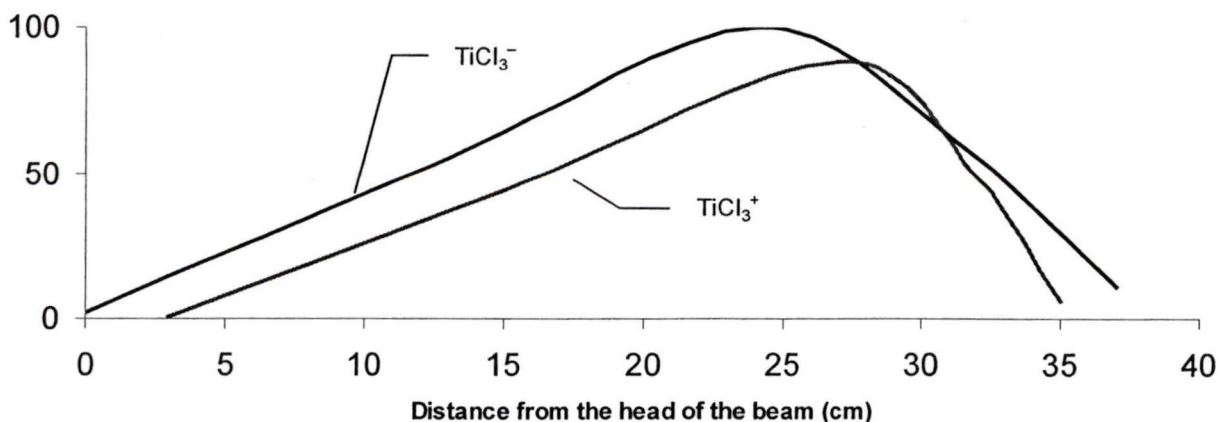
interested in was the density distribution and the duration time that the beam needed in order to pass the repeller.

3.4 Density Distribution of Positively charged Clusters in the Molecular Beam

Since it is not easy to generate positively charged carbon clusters, a Ti rod was used in this experiment, with the carrying gas of 4% Cl₂ in Helium. The density distribution of the TiCl₃⁻ and TiCl₃⁺ cluster in the original beam were studied.

The most interesting observation is that the maximum signal intensity of TiCl₃⁺ can be obtained with a repeller trigger delay of 360 μs. However, the maximum part of the TiCl₃⁻ signal with the same source reaches the repeller at 310 μs, which is 50 μs earlier than the positive ions. This indicates that the positively charged clusters fly slower than the negatively charged clusters.

Figure 3.6: Density distribution of the TiCl₃⁻ and TiCl₃⁺ clusters in the molecular beam



By repeating the analyses carried out in section 3.2, the density distribution of TiCl_3^+ in the molecular beam can be determined as presented in Figure 3.6.

Figure 3.6 shows that TiCl_3^+ clusters achieve the maximum density at about 27% offset from the tail to the middle point of the beam, which is significantly different from the behavior of TiCl_3^- . The positively charged clusters also spend about $170\mu\text{s}$ in order to pass the repeller, which proves again that the width of the molecular beam is controlled by the duration time of the valve, not by the character of the reaction chamber.

Chapter 4 TOF-MS Space Focusing

This chapter describes how the TOF-MS space focusing was carried out in order to optimize the resolution of each single mass peak.

4.1 Theory

4.1.1 Overview

If all the charged clusters being accelerated in the first acceleration region of the repeller were in a plane parallel to the repeller, and with zero initial vertical velocity, the flight time would be the same for all ions which had the same q/m , and the resolution would be limited only by the detecting equipment. In practice, the resolving power of a TOF spectrometer depends on its ability to reduce the time spread caused by ever-present initial space and initial kinetic energy distributions.

Ions have a spatial distribution since they will be at different vertical positions when they reach the first acceleration region. The ability of the spectrometer to resolve masses despite the initial space distribution is called the spatial resolution, while the reduction of the time spread introduced by the initial kinetic energy distribution is called the energy resolution. The initial spatial distribution can be considered as a deviation of initial position (measured from the middle of the first acceleration region) in regard to its average, S_0 , so that

$$S_{\max} = S_0 + \frac{1}{2} \Delta S \quad \text{and} \quad S_{\min} = S_0 - \frac{1}{2} \Delta S \quad (4.1)$$

The spatial resolution problem is how to reduce the time spread, $\Delta T_{\Delta S}$. This can be done either by making ΔS small in comparing with S_0 , or by space focusing, which gives each ion a velocity dependent on S (as well as on q/m) in such a way as to minimize $\Delta T_{\Delta S}$.

The maximum time spread introduced by the spread of initial velocities, ΔT_{θ} , is the difference in flight times between a pair of identical ions formed at the same position and with the same maximum initial speed, but with oppositely directed velocities. The value of ΔT_{θ} can be reduced by increasing the ratio of the ion's total energy to its initial energy, or by employing either of two types of energy focusing. One type of focusing involves adjusting the parameters available in the beam source so that it produces a smaller initial kinetic energy distribution. The other form of focusing introduces a time lag between the creation of the ions and their acceleration.

Spatial resolution and energy resolution place opposite requirements on several system parameters. Detailed discussions of these requirements are carried out separately in the following sections.

4.1.2 The TOF Mass Spectrometer setup

The TOF mass spectrometer contains two accelerating regions as shown in Figure 4.1. When the ions reach the first accelerating region, the pulse sent to the repeller generates an electric field, E_s . Ions are then accelerated to the second accelerating region by E_s . The second accelerating region, of width d , has an electric field, E_d . The third region, D , is field free. The double-field source

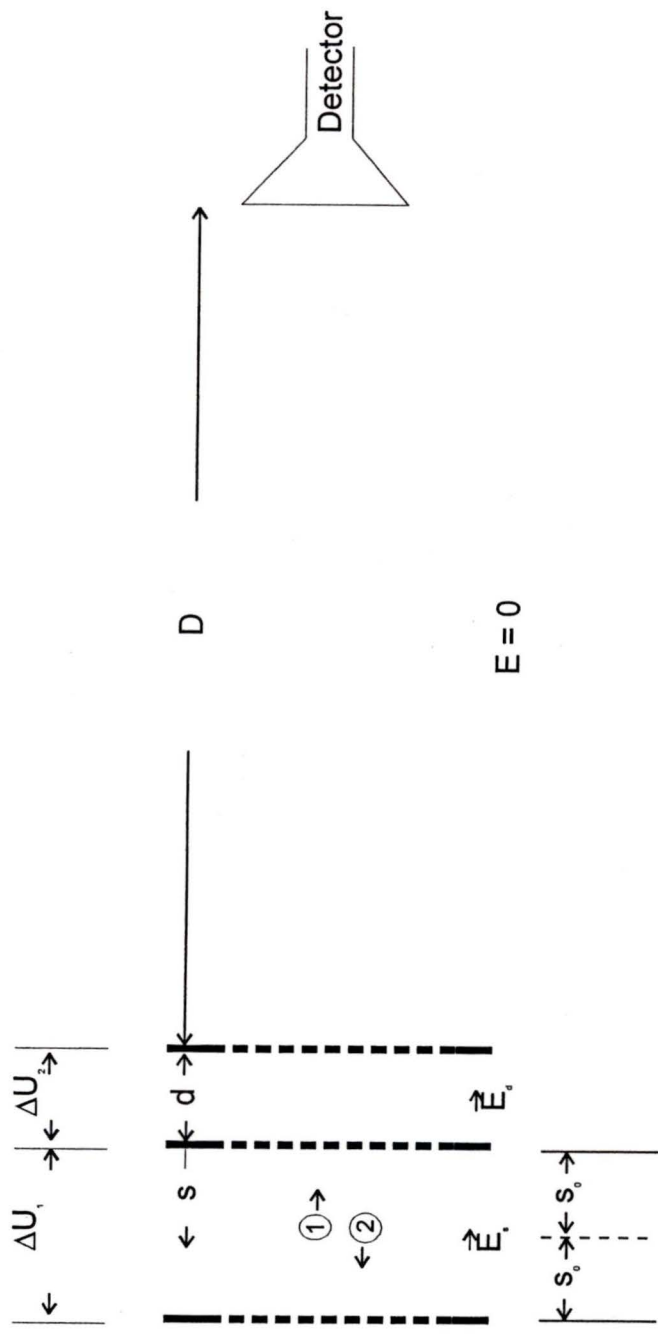


Figure 4.1: TOF Setup in our experiment

introduces two new parameters, d and E_d/E_s .

4.1.3 Flight Time

In moving through the source, any ion with initial energy, U_0 , will increase its energy to a value, U , which is independent of m , but dependent on U_0 , S and q [9],

$$U = U_0 + qSE_s + qdE_d \quad (4.2)$$

Under these conditions, the time-of-flight can easily be shown to be

$$t(U_0, S) = t_s + t_d + t_D \quad (4.3)$$

Where

$$t_s = \frac{(2m)^{\frac{1}{2}}}{qE_s} [(U_0 + qSE_s)^{\frac{1}{2}} \pm (U_0)^{\frac{1}{2}}] \quad (4.3a)$$

$$t_d = \frac{(2m)^{\frac{1}{2}}}{qE_d} [U^{\frac{1}{2}} - (U_0 + qSE_s)^{\frac{1}{2}}] \quad (4.3b)$$

$$t_D = (2m)^{\frac{1}{2}} D / 2U^{\frac{1}{2}} \quad (4.3c)$$

The + and – signs in t_s correspond to initial velocities directed away respectively, and toward the collector.

In the analysis which follows, it is convenient to investigate t when $U_0 = 0$, $S = S_0$. If we define

$$U_i = qS_0E_s + qdE_d \quad (4.4a)$$

and

$$k_0 = (S_0E_s + dE_d) / S_0E_s \quad (4.4b)$$

then $t(0, S_0)$, from a substitution of Eqs. (4.4) into Eqs. (4.3) becomes

$$t(0, S_0) = \left(\frac{m}{2U_i} \right)^{\frac{1}{2}} \left(2k_0^{\frac{1}{2}} S_0 + \frac{2k_0^{\frac{1}{2}}}{k_0^{\frac{1}{2}} + 1} d + D \right) \quad (4.5)$$

4.1.4 Spatial Resolution

Spatial focusing depends on the fact that an ion initially closer to the detector (and thus of smaller S value) acquires less energy and is therefore eventually overtaken by ions which have higher initial s values. To find the position at which

ions whose initial S values were $S = S_0 \pm \frac{1}{2} \delta S$ pass each other, we set

$(dt/dS)_{0, S_0} = 0$, using Eq. (4.3) for t and, by substitution from Eq. (4.4), obtain

$$D = 2S_0 k_0^{\frac{3}{2}} \left(1 - \frac{1}{k_0 + k_0^{\frac{1}{2}}} \times \frac{d}{S_0} \right) \quad (4.6)$$

This focusing condition is the same for all ions and is independent of the total energy of the system. If S_0 , d and D are fixed, which is the situation in our experiment, E_d/E_s is uniquely determined by Eq. (4.6), since k_0 can have only one physically significant value. Thus in the double-field system, the spatial focus is obtained by a simple adjustment of E_d/E_s .

4.1.5 Energy Resolution

To investigate the effects of initial kinetic energies [9], it is convenient to consider two ions formed at the same initial position S with equal, but oppositely directed speeds, as shown in Fig. 4.1. Ion 2 moves away from the collector and therefore is decelerating due to E_s until it stops. It is then accelerated, returning to S with its original speed. Subsequently, its motion is identical with that of ion 1, which it continues to lag behind by the "turn-around" time. The time spread, Δt_θ , introduced by the initial energies, is the "turn-around" time (i.e., twice the deceleration time) of an ion having the maximum initial energy being considered,

$$\Delta t_\theta = 1.02 \frac{2v_0 m}{qE_s} = 1.02 \frac{2(2mU_0)^{\frac{1}{2}}}{qE_s} \quad (4.7)$$

If we consider only the effects of initial energy, the maximum resolvable mass, M_θ , is that for which the energy time spread, Δt_θ , equals the time between adjacent mass peaks, $t/2m$ (i.e., $M_\theta = t/2\Delta t_\theta$). This is evaluated by substituting from Eqs. (4.5) and (4.7). If D/S_0 from the focus condition Eq. (4.6) is substituted in the result, M_θ is given by

$$M_\theta = \frac{1}{4} \left(\frac{U_t}{U_0} \right)^{\frac{1}{2}} \left(\frac{k_0 + 1}{k_0^{\frac{1}{2}}} - \frac{k_0^{\frac{1}{2}} - 1}{k_0 + k_0^{\frac{1}{2}}} \times \frac{d}{S_0} \right) \quad (4.8)$$

In general, M_θ is increased by increasing D and/or decreasing s_0 and d. In our experiment, the kinetic energy distribution generated by our molecular beam source is very small. The resolution problem generated by the original kinetic

energy distribution is also small, compared with the resolution problem generated by the original space distribution. Therefore, the effect of energy focusing was neglected in our experiment.

4.2 Experimental Space Focusing Result

A convenient measure of the resolution of the TOF is the largest mass, M , for which adjacent masses are essentially completely separated, i.e., that mass for which the time spread for ions of the same mass simply equals the time between adjacent masses.

Figure 4.2_a shows the mass peak collected without spatial focusing. A Ti rod and 4% air in helium was used in this experiment. The width of the peak is approximately $4 \mu\text{s}$, and it is difficult to identify masses from the signal collected. Figure 4.2_b shows the correlative mass signal with spatial focusing. The mass peaks are separated by approximately $1.5\mu\text{s}$, and their masses are easily identified.

In our experimental setup, we have

$$D = 90\text{cm}, d = 1\text{cm}, S_0 = 1\text{cm}$$

Substitute these constants into Eq. (5), we get:

$$90 = 2 \times 1 \times k_0^{\frac{3}{2}} \left(1 - \frac{k_0^{\frac{3}{2}}}{k_0 + k_0^{\frac{1}{2}}} \right) \quad (4.9)$$

Eq. (4.9) can be simplified to :

Figure 4.2_a TOF mass signal without space focusing

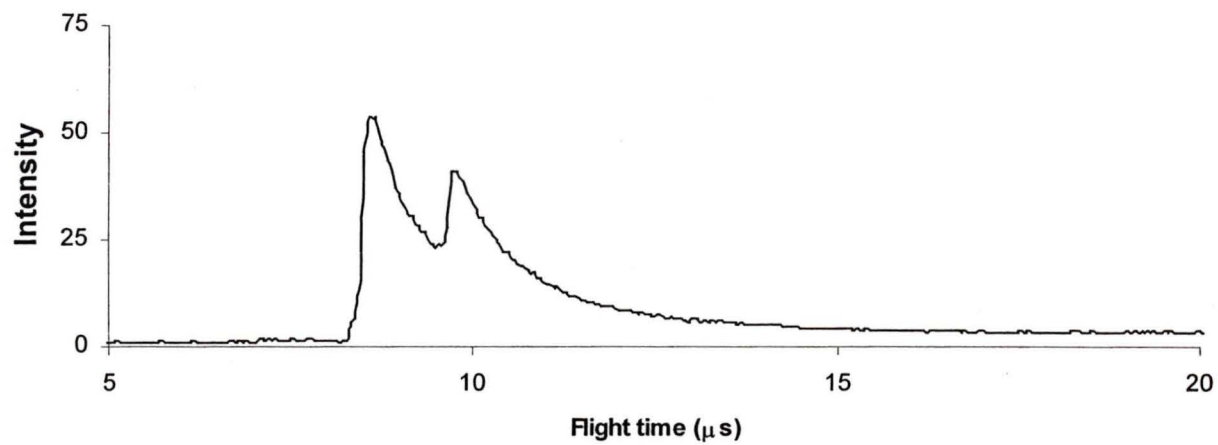
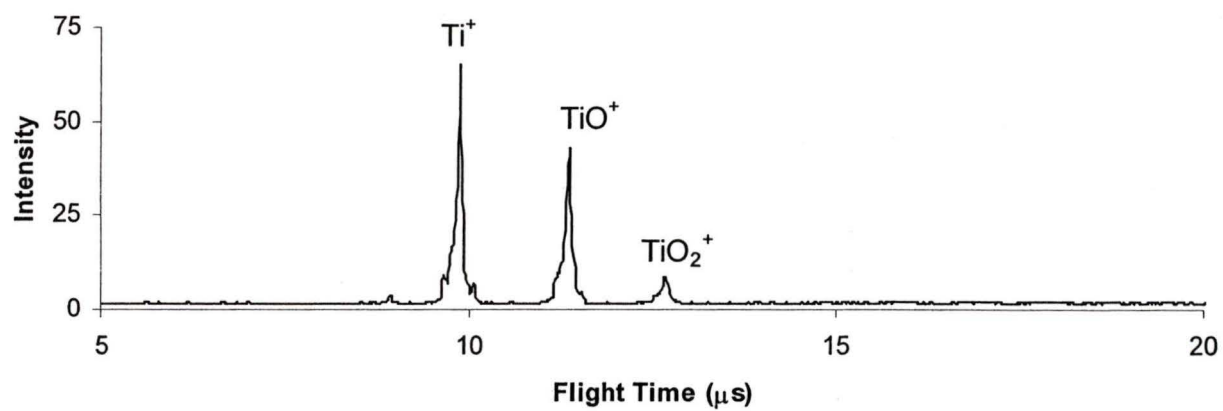


Figure 4.2_b TOF Mass Signal with space focusing



$$k_0^2 + k_0^{\frac{3}{2}} - k_0 - 45k_0^{\frac{1}{2}} - 45 = 0 \quad (4.10)$$

The result of Eq. (4.10) is $k_0 = 13.18$

Substitute this to Eq.(4.4d) gives us:

$$\begin{aligned} k_0 &= (s_0 E_s + dE_d) / s_0 E_s \\ &= \left(\frac{1}{2} \Delta U_1 + \Delta U_2 \right) / \frac{1}{2} \Delta U_1 \\ &= 13.18 \end{aligned} \quad (4.11)$$

Therefore, the space focusing condition for our setup will be

$$\frac{\Delta U_2}{\Delta U_1} = 6.1 \quad (4.12)$$

However, during the experiment, the ratio of U_2 with U_1 used varies between 1:5.4 and 1:11.8. The value was adjusted to reach the optimized space focusing condition, and the real value used is usually different from the one calculated.

There are five reasons for this:

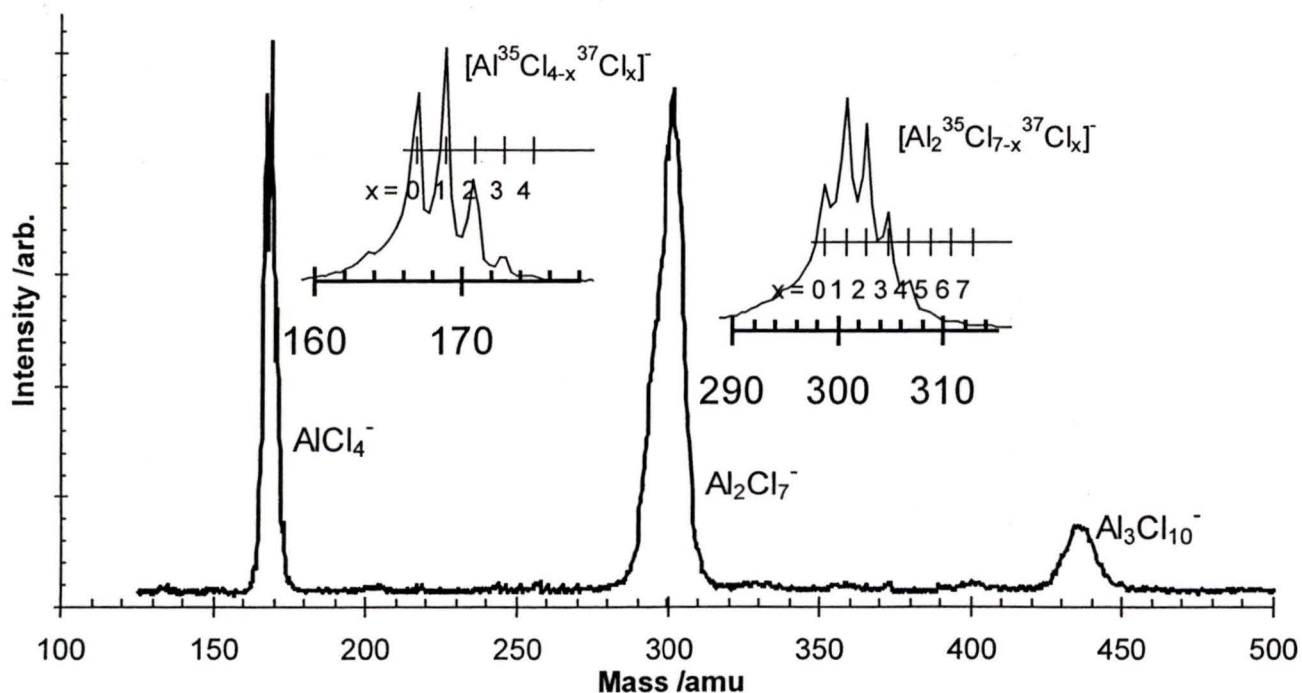
1. The constant D , d , and S_0 can not be measured precisely.
2. The three electrical grids used in the acceleration regions are not perfectly flat, which means E_s and E_d are not perfectly uniform electrical field.
3. Since a pulsed high voltage electrical field was used, it was actually a very powerful microwave source. There was a leaking of this electrical field from the acceleration region to the field free region D , which made region D not perfectly field free.
4. The energy focusing condition was not considered in the calculation.

5. Space charging of the original molecular beam occurred every time the electrical field was turned on.

6. Edge effect of the electrical field.

Figure 4.3 shows the mass spectra obtained from an aluminum rod and 5% chlorine in helium as carrying gas, which demonstrates the biggest mass that can be resolved in our experiment. The optimized mass resolution we can achieve is approximately 300. Detailed discussion of aluminum chlorine clusters can be found in the next chapter.

Figure 4.3 The Mass Spectra of aluminum-chlorine negatively charged clusters



Chapter 5: Species Generated from Laser Ablation of Transition Metal in a Chlorine or Hydrogen Sulfide Carrier Gas

This chapter describes the negatively and positively charged clusters generated by the ablation of metal rods in an atmosphere of Cl_2 , or an atmosphere of H_2S . The experiments were done by using several metal rods – Ti, Cr, Fe, Co, Ni, Cu, Zn, Al. With the exception of different rods, all the clusters were generated in the same reaction chamber with the same ablation laser power. The pressure of the carrying gas – 3~5% Cl_2/He or $\text{H}_2\text{S}/\text{He}$ – was set at 3atm originally, and dropped slightly as the experiment went on.

5.1 Transition Metal-chlorine clusters

5.1.1: Titanium Chlorides

a: negatively charged clusters:

Figure 5.1 shows the mass spectrum obtained for negatively charged titanium-chlorine clusters of Ti. TiCl_2 , TiCl_3 , TiCl_4 are the common neutral titanium chlorides. The addition of one Cl^- ion to each of them forms TiCl_3^- , TiCl_4^- , and TiCl_5^- , as were detected. No clusters with more than one Ti atom were detected.

b: positively charged clusters

Figure 5.2 shows the positively charged titanium chlorine clusters that were detected, which were TiCl^+ , TiCl_2^+ , and TiCl_3^+ . They can be viewed as formed by

Figure 5.1 Mass Spectrum of negatively charged Titanium-chlorine clusters

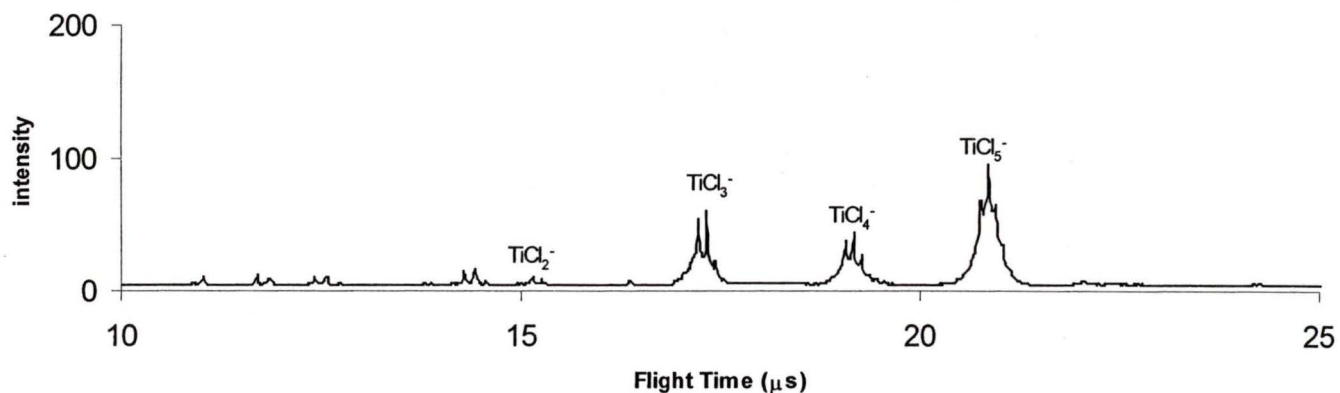
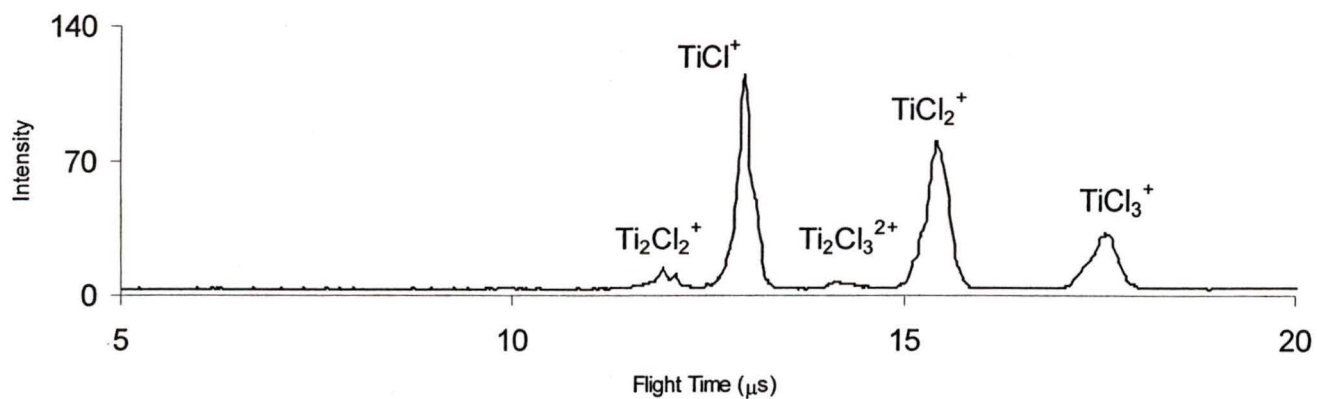


Figure 5.2 Mass Spectrum of Positively charged Titanium-chlorine Clusters



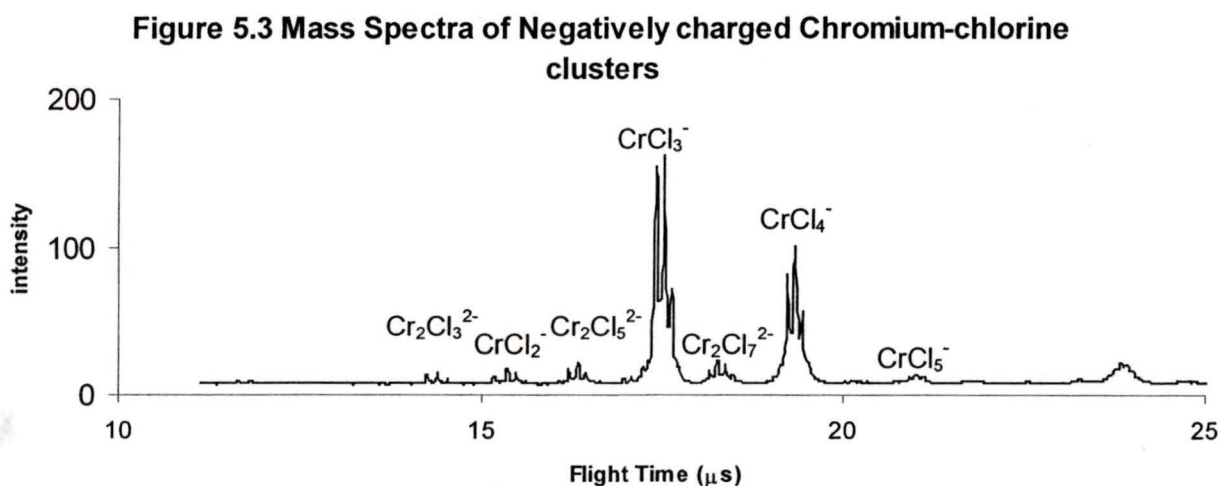
loss of one Cl^- ion from the stable neutral chlorides of Ti. TiCl^+ has higher intensity than TiCl_2^+ which may be due to the higher number of collisions needed to form the latter. $\text{Ti}_2\text{Cl}^{2+}$ and $\text{Ti}_2\text{Cl}_3^{2+}$ were also detected with low intensity.

5.1.2: Chromium Chlorides

a: Negatively charged Clusters

CrCl_2 , CrCl_3 , CrCl_4 are the common chromium chlorides; therefore, it is not surprising that the CrCl_3^- ($\text{CrCl}_2 + \text{Cl}^-$), CrCl_4^- ($\text{CrCl}_3 + \text{Cl}^-$) and CrCl_5^- ($\text{CrCl}_4 + \text{Cl}^-$) clusters were detected with reasonable intensity (Figure 5.3). As discussed with Ti, CrCl_5^- was also detected with low intensity.

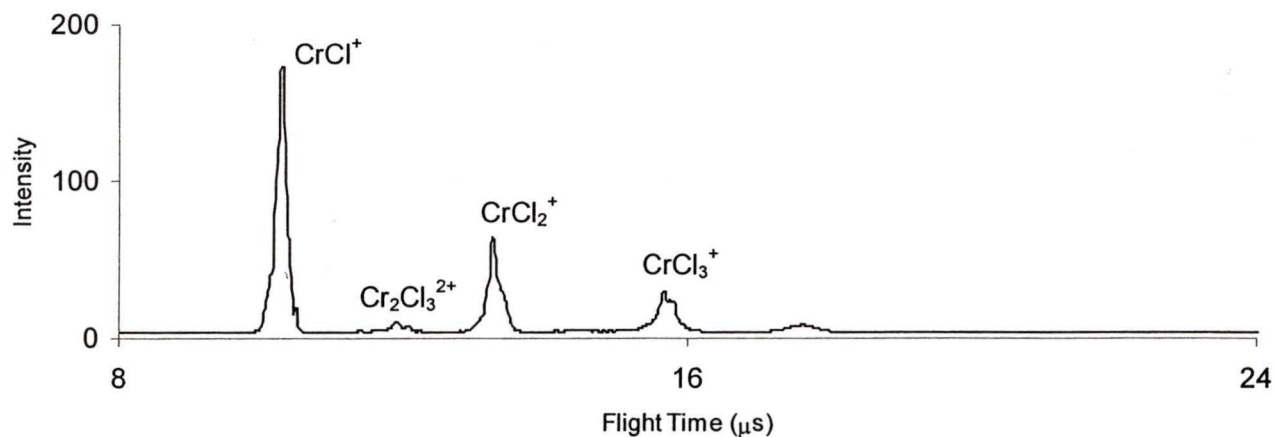
Multiple charged Chromium Chlorine clusters like $\text{Cr}_2\text{Cl}_9^{2-}$ in solid phase are very well studied [53]. Several multiple charged chromium chlorine clusters ($\text{Cr}_2\text{Cl}_3^{2-}$, $\text{Cr}_2\text{Cl}_5^{2-}$, $\text{Cr}_2\text{Cl}_7^{2-}$) were also detected with low intensity.



b: Positively charged Clusters

The positively charged clusters detected for chlorine were CrCl^+ , CrCl_2^+ , and CrCl_3^+ , as shown in Figure 5.4. They can be viewed as formed by loss of one Cl^- ion from the common neutral chromium chlorides. $\text{Cr}_2\text{Cl}_3^{2+}$ was also detected, it is a known cation in solid phase [54].

Figure 5.4 Mass Spectrum of Positively charged Chromium-chlorine Clusters



5.1.3: Iron Chlorides

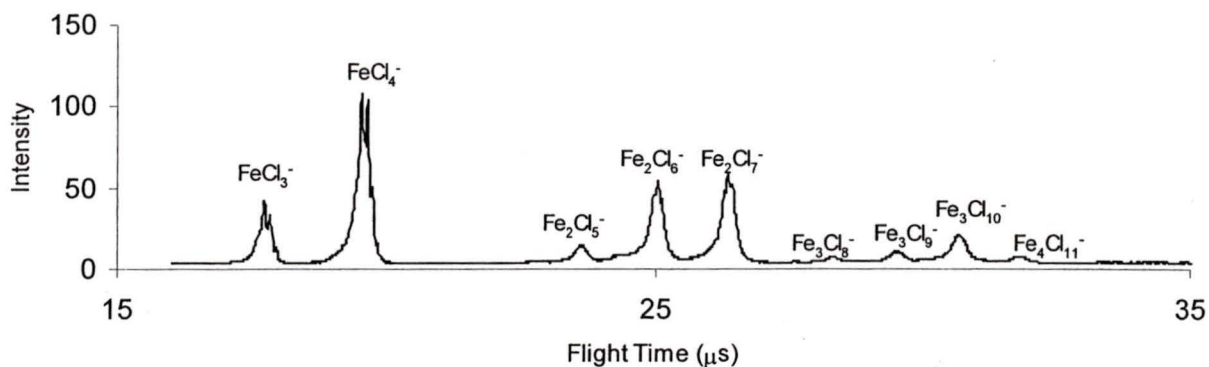
a: Negatively charged Clusters

Figure 5.5 shows the large number of anionic Fe_nCl_m^- species obtained. The common iron chlorides – FeCl_2 and FeCl_3 – give stable negatively charged monoiron clusters – FeCl_3^- and FeCl_4^- – by attachment of one Cl^- ion. Thereafter, all other observed ions can be seen as accretions of the two neutrals, plus the two dominant anions as given in Table 5.1.

Table 5.1: Possible building block combinations of negatively charged iron-chlorine clusters and their relative intensity

	# of FeCl_2	# of FeCl_3^-	# of FeCl_3	# of FeCl_4^-	Intensity
FeCl_3^-	0	1	0	0	37
FeCl_4^-	0	0	0	1	100
Fe_2Cl_5^-	1	1	0	0	12
Fe_2Cl_6^-	0	1	1	0	49
Fe_2Cl_7^-	0	0	1	1	53
Fe_3Cl_8^-	1	1	1	0	4
Fe_3Cl_9^-	1	0	1	1	7
$\text{Fe}_3\text{Cl}_{10}^-$	0	0	2	1	17
$\text{Fe}_4\text{Cl}_{11}^-$	2	0	1	1	4

Figure 5.5 Mass Spectrum of Negatively charged Iron-chlorine Species



It is well known that FeCl_3 is a stable compound (much more stable than FeCl_2); therefore, FeCl_4^- ($\text{FeCl}_3 + \text{Cl}^-$) was observed with the highest intensity in the mass spectrum, and much stronger than FeCl_3^- ($\text{FeCl}_2 + \text{Cl}^-$). The intensity of the other clusters formed through these building blocks followed this trend in relative abundance. Fe_2Cl_7^- ($\text{FeCl}_3 + \text{FeCl}_4^-$) has the maximum intensity among the bigger clusters, while Fe_2Cl_6^- ($\text{FeCl}_2 + \text{FeCl}_4^-$) is the second largest one. Fe_2Cl_5^- ($\text{FeCl}_2 + \text{FeCl}_3^-$) has the smallest intensity among the di-iron species detected.

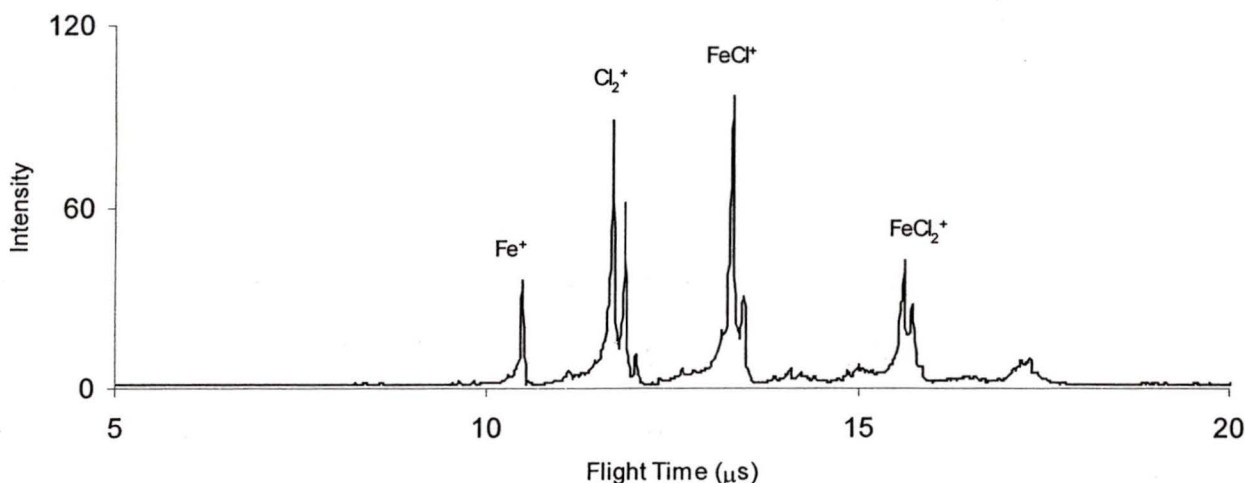
b: Positively charged Clusters

Iron did not form positively charged clusters with more than one Fe atom, as shown in Figure 5.6. The two positive iron-chlorine ions obtained were FeCl_2^+ and FeCl^+ . These species can be seen as the result of the following two reactions:



The mass peak with flight time of about 17.5 μ s may be some multiply charged iron-chlorine clusters. Since the charge is unknown, the formula is hard to decide.

Figure 5.6 Mass Spectrum of Positively charged Iron-chlorine Clusters



5.1.4: Cobalt Chlorides

a: Negatively charged Clusters

The cobalt chlorine negatively charged clusters detected are shown in Figure 5.7. The detected cobalt chlorine cluster with the highest intensity is $CoCl_3^-$, which can be treated as the stable $CoCl_2$ plus one Cl^- . Since $CoCl_3$ is also quite a stable neutral compound, $CoCl_4^-$ is detected with reasonable intensity as well. $CoCl$ is also a known compound, although not as stable as the other two salts, therefore

Figure 5.7 Mass Spectrum of Negatively charged Cobalt-chlorine Clusters

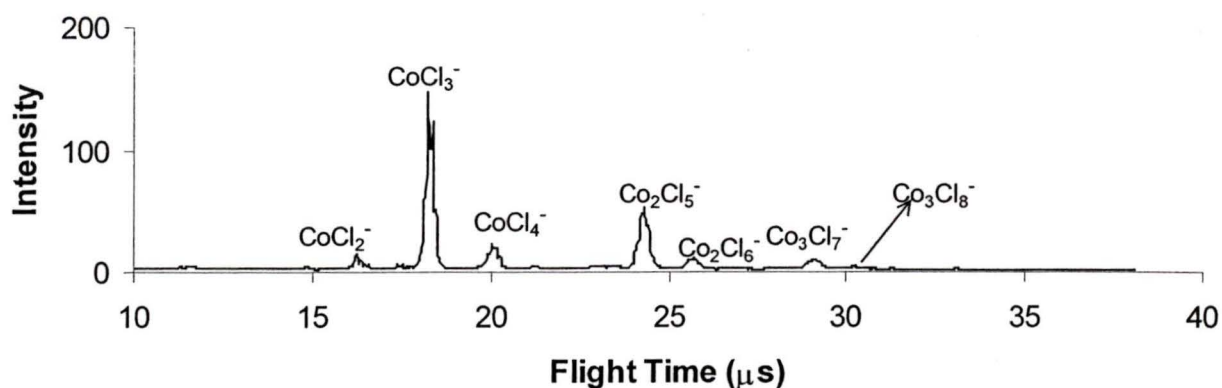


Table 5.2: Building block combinations of negatively charged cobalt-chlorine clusters and their relative intensity

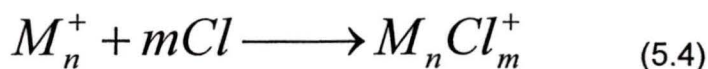
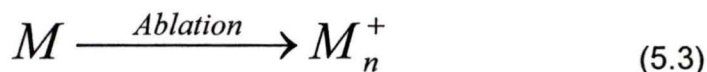
	# of CoCl_2^-	# of CoCl_2	# of CoCl_3^-	# of CoCl_3	# of CoCl_4^-	Intensity
CoCl_2^-	1	0	0	0	0	8
CoCl_3^-	0	0	1	0	0	100
CoCl_4^-	0	0	0	0	1	15
Co_2Cl_5^-	0	1	1	0	0	36
Co_2Cl_6^-	0	0	1	1	0	6
Co_3Cl_7^-	1	1	1	0	0	2
Co_3Cl_8^-	0	1	1	1	0	6

CoCl_2^- ($\text{CoCl} + \text{Cl}^-$) was detected with a low intensity. As with Fe, the clusters detected can be constructed by 3 anionic building blocks and 2 neutrals, as shown in table 5.2.

The intensity of the bigger clusters falls into the same intensity trend as the iron clusters. That is, the most abundant di-cobalt ions arise from the most abundant mono-cobalt ions.

b: Positively charged Clusters

Cobalt forms positively charged clusters with more than one metal atom. Figure 5.8_a and 5.8_b show the cobalt-chlorine positively charged clusters detected under the same formation conditions, but at different times during the experiments. Figure 5.8_b was obtained one day after 5.8_a. From the two Figures, it is clear that the intensity of each mass peak is variable. In Figure 5.8_a, the dominant species is Co_2Cl^+ , and the peak for Co_2Cl_2^+ is very small. However, in Figure 5.8_b, the peak with the maximum intensity is CoCl^+ , with a reasonably high Co_2Cl_2^+ peak. The reason for this phenomenon may be as follows: the hot metal plasma ablated from the metal rod may form pure metal clusters with a positively charged charge at first:



Then the charged metal clusters react with one or two chlorine atoms in the carrying gas to form the final clusters. An observation consistent with this result is

Figure 5.8_a Mass Spectrum of Positively charged Cobalt-chlorine Clusters

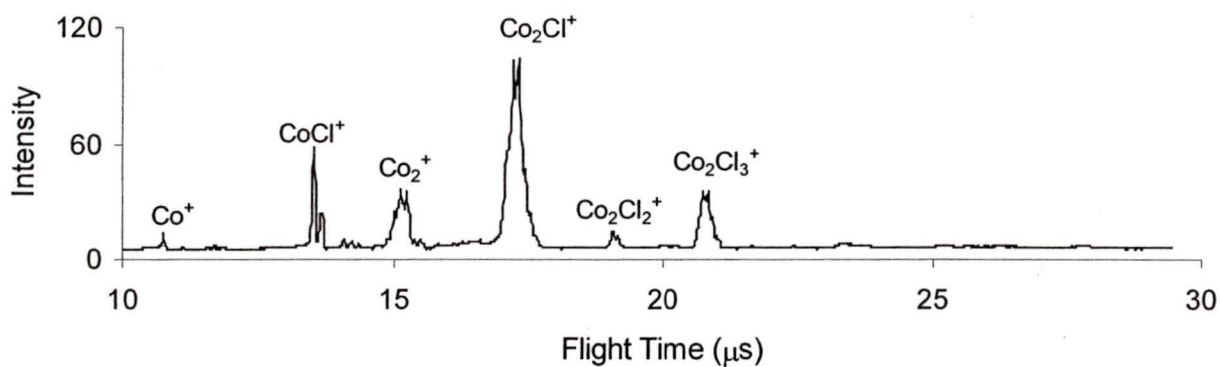
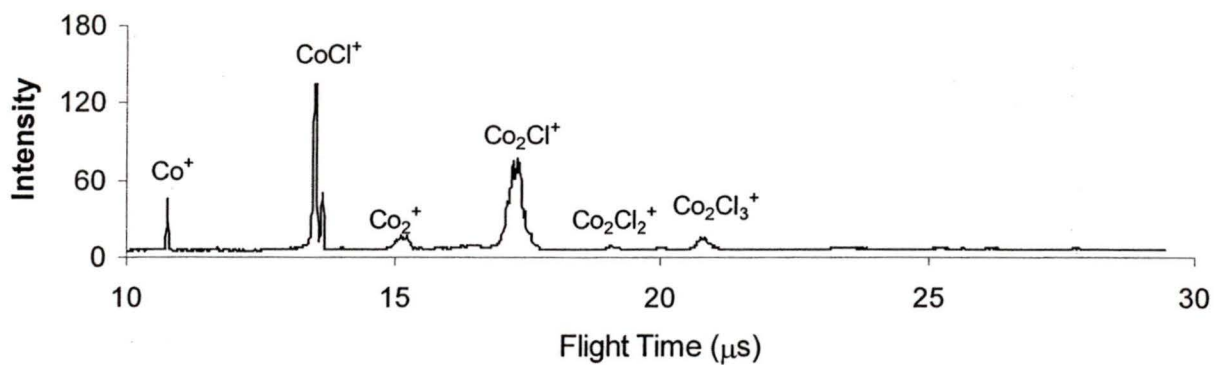


Figure 5.8_b Another Mass Spectrum of Positively charged Cobalt-chlorine Clusters



that both Figure 5.8_a and 5.8_b show the Co_2^+ peak, but 5.1.8_a has a more intense Co_2^+ peak, which is followed by the three Co_2Cl_n^+ ($n = 1,2,3$) peaks with higher intensity than in Figure 5.8_b.

Since the possibility for the metals to form positively charged clusters is unpredictable – any slight inevitable experimental condition change will change the result significantly – the final mass spectrum obtained may vary from time to time.

5.1.5: Nickel Chlorides

a: Negatively charged Clusters

The only stable neutral chloride of nickel is NiCl_2 . For this reason, Figure 5.9 NiCl_3^- ($\text{NiCl}_2 + \text{Cl}^-$) has a much higher intensity than NiCl_2^- or NiCl_4^- . The building block construction of bigger clusters and their intensity trends are shown in Table 5.3.

Figure 5.9 Mass Spectrum of Negatively Charged Nickel-chlorine Clusters

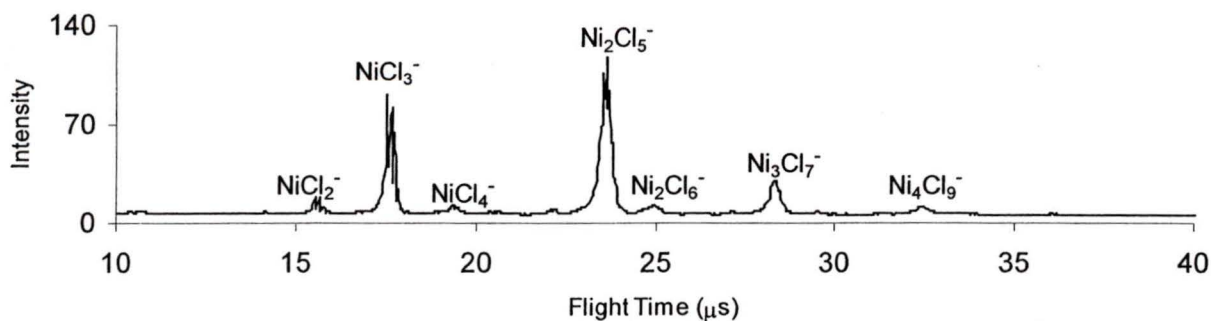


Table 5.3: Building block combinations of negatively charged Nickel-chlorine clusters and their relative intensity

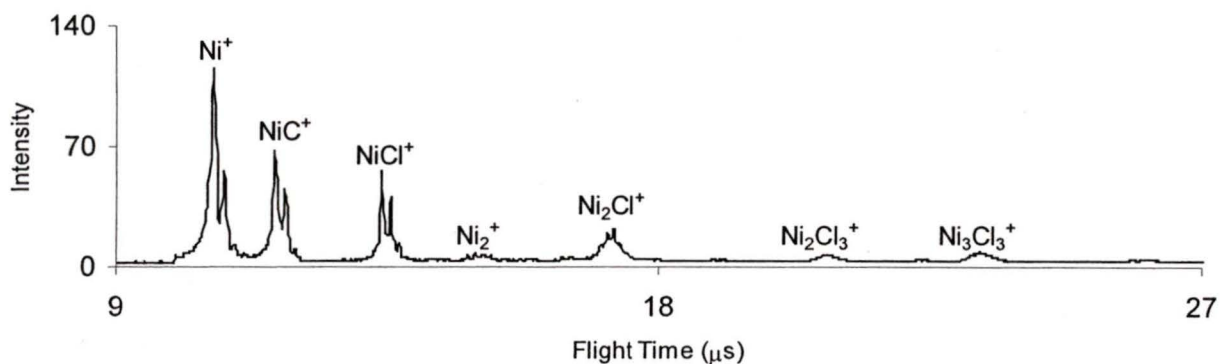
	# of NiCl ₂	# of NiCl ₂ ⁻	# of NiCl ₃ ⁻	# of NiCl ₄ ⁻	Intensity
NiCl ₂ ⁻	0	1	0	0	11
NiCl ₃ ⁻	0	0	1	0	75
NiCl ₄ ⁻	0	0	0	1	6
Ni ₂ Cl ₅ ⁻	1	0	1	0	100
Ni ₂ Cl ₆ ⁻	1	0	0	1	6
Ni ₃ Cl ₇ ⁻	2	0	1	0	21
Ni ₄ Cl ₉ ⁻	3	0	1	0	5

b: Positively charged Clusters

Ni⁺ is the dominant species in the mass spectrum of positively charged chlorine clusters of nickel (Figure 5.10); the second biggest peak in the spectrum is NiCl⁺, which is formed from NiCl₂ by losing of one Cl⁻. For the same reason as discussed for cobalt, pure nickel positively charged clusters were apparently

formed first, and then reacted with chlorine atoms to form the clusters obtained. Although Ni_2^+ was detected, its low intensity may be due to its very high reactivity with chlorine atoms.

Figure 5.10 Mass Spectrum of Positively charged Nickel-chlorine Clusters



The NiCl^+ peak obtained may be due to residual carbon on the walls of the reaction chamber, since this procedure followed an experiment in which a carbon rod was used.

5.1.6: Copper Chlorides

a: Negatively charged Clusters

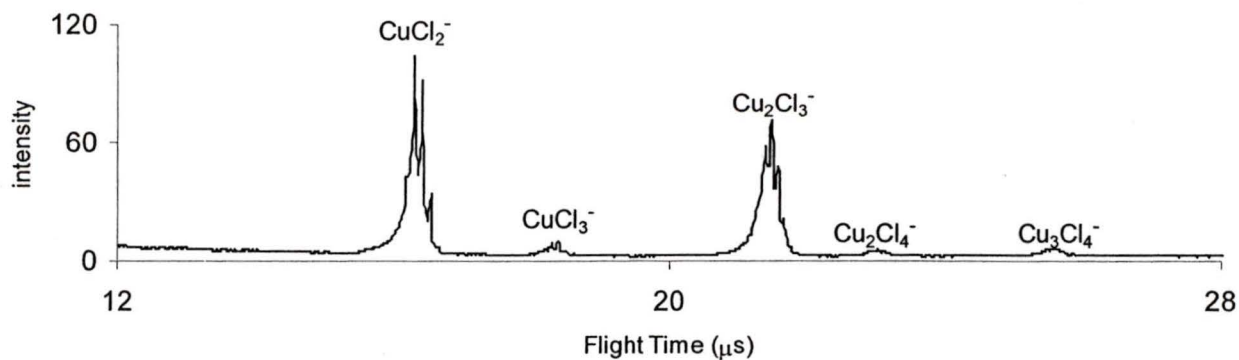
Although CuCl_2 is much more stable in nature than CuCl , the dominant species detected in the mass spectrum of copper chlorides is CuCl_2^- ($\text{CuCl} + \text{Cl}^-$), and the intensity of CuCl_3^- is very small. This will be outlined later in the molecular orbital discussion in section 5.2.

As shown in Table 5.4 and Figure 5.11, the intensity trend in the larger clusters is quite reasonable if CuCl , CuCl_2^- and CuCl_3^- are used as the basic building blocks.

Table 5.4: Building block combinations of negatively charged copper-chlorine clusters and their relative intensity

	# of CuCl	# of CuCl_2^-	# of CuCl_3^-	Intensity
CuCl_2^-	0	1	0	100
CuCl_3^-	0	0	1	7
Cu_2Cl_3^-	1	1	0	69
Cu_2Cl_4^-	1	0	1	4
Cu_3Cl_4^-	2	1	0	4

Figure 5.11 Mass Spectrum of Negatively Charged Copper-chlorine Clusters



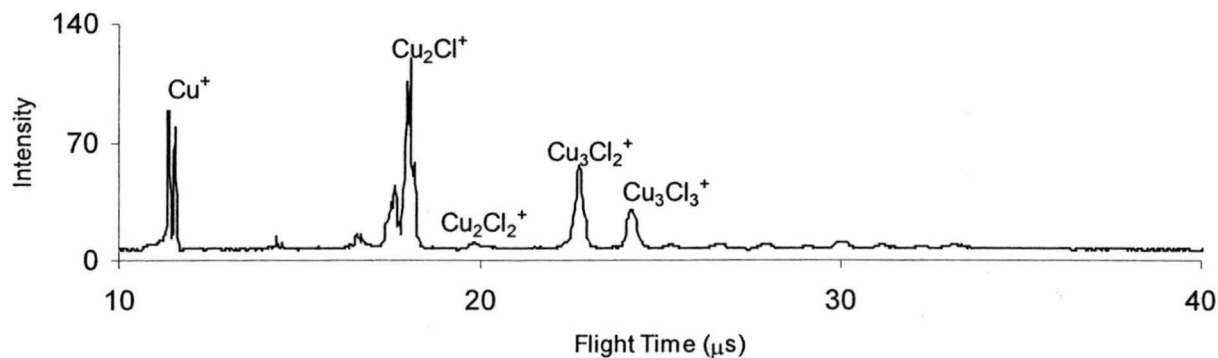
b: Positively charged Clusters

From Figure 5.12, it appears that Cu^+ is the only reasonably charged building block for positively charged copper chlorine clusters. Based on neutral CuCl and CuCl_2 as the other two building blocks. The ions observed can be built up, as shown in table 5.5.

Table 5.5: Building block combinations of positively charged copper-chlorine clusters and their relative intensity

	# of Cu^+	# of CuCl	# of CuCl_2	Intensity
Cu^+	1	0	0	73
CuCl^+	0	0	0	<1
Cu_2Cl^+	1	1	0	100
Cu_2Cl_2^+	1	0	1	4
Cu_3Cl_2^+	1	2	0	45
Cu_3Cl_3^+	1	1	1	21

Figure 5.12 Mass Spectrum of Positively Charged Copper-chlorine Clusters



5.1.7: Zinc Chlorides

a: Negatively charged Clusters

The analysis of negatively charged zinc-chlorine clusters (Figure 5.13) is simple. Since ZnCl_2 is the most stable zinc chloride, it is easy to conclude that ZnCl_3^- ($\text{ZnCl}_2 + \text{Cl}^-$) is the dominant species in the spectrum. Using ZnCl_2 and ZnCl_3^- as the basic building blocks for bigger clusters, Zn_2Cl_5^- , Zn_3Cl_7^- and Zn_4Cl_9^- can be formed with the intensities shown in Table 5.6 and Figure 5.13.

Figure 5.13 Mass Spectrum of Negatively Charged Zinc-chlorine Clusters

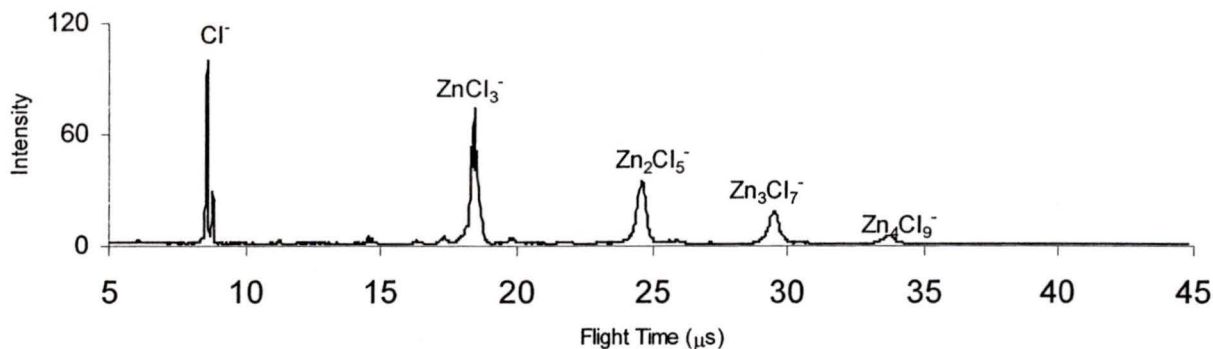


Table 5.6: Building block combinations of negatively charged zinc-chlorine clusters and their relative intensity

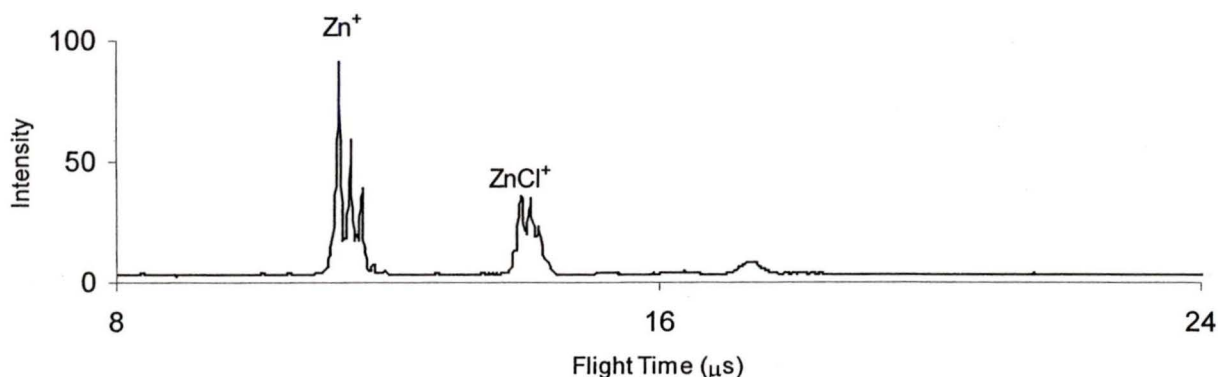
	# of ZnCl_2	# of ZnCl_3^-	intensity
ZnCl_3^-	0	1	100
Zn_2Cl_5^-	1	1	47
Zn_3Cl_7^-	2	1	25
Zn_4Cl_9^-	3	1	6

b: Positively charged Clusters

Zinc does not form bigger positively charged clusters. The only positive ions detected were Zn^+ and ZnCl^+ ($\text{ZnCl}_2 - \text{Cl}$). The peak obtained in the range of

17 μ s ~ 18 μ s was multiple charged large clusters, and their formula can not be concluded from their flight time alone, as was shown in Figure 5.14.

Figure 5.14 Mass Spectrum of Positively Charged Zinc-chlorine Clusters



5.1.8: Summary

Many of the transition metals (Ti, Cr, Fe, Co, Ni, Cu, Zn) of the fourth period were studied. A summary of the transition metal-chlorine positively and negatively charged clusters generated, and their relative intensities are listed in table 5.7

In general, the negatively charged clusters were generated by using two basic building blocks:

1. the neutral metal chloride compounds (MCl_n) which are stable in both solid and gas phases. One metal element may have several stable chlorides;
2. the negative ions that were formed by adding one Cl^- ion to the stable neutral compound (MCl_{n+1}). Since one metal can have several stable chlorides, the different negative ions can be generated accordingly. These negative ions are

stable in the gas phase. They usually have the biggest intensity among all the mass peaks detected.

Simply adding these two building blocks together can form all the remaining negatively charged clusters observed for a given element.

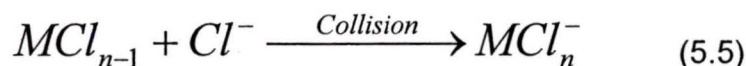
The intensity of the mass peaks that were detected depended on three main factors. The first was the stability of the cluster formed. Clusters with higher stability were observed with higher intensity. The second factor was the probability of the collision to form clusters. A good example can be found in Figure 5.9: NiCl_3^- was observed with much higher intensity than NiCl_4^- , which means the density of NiCl_3^- in the original plasma was much higher than the density of NiCl_4^- . Therefore, the possibility for the NiCl_3^- to collide with one neutral NiCl_2 in order to form Ni_2Cl_5^- was much higher than the possibility for NiCl_4^- to collide with NiCl_2 to form Ni_2Cl_6^- . This is another reason why Ni_2Cl_5^- was observed with a much higher intensity than Ni_2Cl_6^- . The third factor was the number of collisions that the cluster required to be formed. The bigger the cluster the more collisions it needed in order to be formed, and therefore the smaller the intensity. The final intensity of the peaks involves the balancing of these three processes. However, experimental facts such as the power of the laser and the pressure of the carrying gas may alter the intensities, although the relative intensities of the distribution will be the same.

It is interesting to note in Table 5.7 that no metal-monochlorine anions were observed. The reason for this is believed to be the following: Since MCl_{n-1} is a strong Lewis acid and Cl^- is a strong Lewis base, the basic reaction that forms

Table 5.7. Experimentally observed transition metal-chlorine ions and their relative intensity.

Titanium		Chromium		Iron		Cobalt	
TiCl ₂ ⁻	62	CrCl ₃ ⁻	100	FeCl ₃ ⁻	37	CoCl ₂ ⁻	8
TiCl ₃ ⁻	44	CrCl ₄ ⁻	61	FeCl ₄ ⁻	100	CoCl ₃ ⁻	100
TiCl ₄ ⁻	100	CrCl ₅ ⁻	4	Fe ₂ Cl ₅ ⁻	12	CoCl ₄ ⁻	15
TiCl ₅ ⁻	7	Cr ₂ Cl ₃ ²⁻	4	Fe ₂ Cl ₆ ⁻	49	Co ₂ Cl ₅ ⁻	36
		Cr ₂ Cl ₅ ²⁻	8	Fe ₂ Cl ₇ ⁻	53	Co ₂ Cl ₆ ⁻	6
TiCl ⁺	100	Cr ₂ Cl ₇ ²⁻	12	Fe ₃ Cl ₈ ⁻	4	Co ₃ Cl ₇ ⁻	2
TiCl ₂ ⁺	69			Fe ₃ Cl ₉ ⁻	7	Co ₃ Cl ₈ ⁻	6
TiCl ₃ ⁺	27	CrCl ⁺	100	Fe ₃ Cl ₁₀ ⁻	17	Co ⁺	9
Ti ₂ Cl ²⁺	8	CrCl ₂ ⁺	36	Fe ₄ Cl ₁₁ ⁻	4	CoCl ⁺	71
Ti ₂ Cl ₃ ²⁺	3	CrCl ₃ ⁺	16	Fe ⁺	36	CoCl ₂ ⁺	3
		Cr ₂ Cl ₃ ²⁺	3	FeCl ⁺	100	Co ₂ Cl ⁺	100
				FeCl ₂ ⁺	44	Co ₂ Cl ₂ ⁺	4
						Co ₂ Cl ₃ ⁺	9
Nickel		Copper		Zinc		Aluminum	
NiCl ₂ ⁻	11	CuCl ₂ ⁻	100	ZnCl ₃ ⁻	100	AlCl ₄ ⁻	100
NiCl ₃ ⁻	75	CuCl ₃ ⁻	7	Zn ₂ Cl ₅ ⁻	47	Al ₂ Cl ₇ ⁻	99
NiCl ₄ ⁻	6	Cu ₂ Cl ₃ ⁻	69	Zn ₃ Cl ₇ ⁻	25	Al ₃ Cl ₁₀ ⁻	16
Ni ₂ Cl ₅ ⁻	100	Cu ₂ Cl ₄ ⁻	4	Zn ₄ Cl ₉ ⁻	6		
Ni ₂ Cl ₆ ⁻	6	Cu ₃ Cl ₄ ⁻	4			Al ⁺	100
Ni ₃ Cl ₇ ⁻	21	Cu ⁺	73			AlCl ⁺	15
Ni ₄ Cl ₉ ⁻	5	CuCl ⁺	<1	Zn ⁺	100	Al ₃ Cl ⁺	3
		Cu ₂ Cl ⁺	100	ZnCl ⁺	38	Al ₃ Cl ₂ ⁺	28
Ni ⁺	100	Cu ₂ Cl ₂ ⁺	4			Al ₄ Cl ⁺	3
NiCl ⁺	48	Cu ₃ Cl ₂ ⁺	45				
Ni ₂ Cl ₂ ⁺	17	Cu ₃ Cl ₃ ⁺	21				
Ni ₂ Cl ₃ ⁺	4						
Ni ₃ Cl ₃ ⁺	5						

the monometal chlorine ions can be viewed as Lewis acid-base reaction:

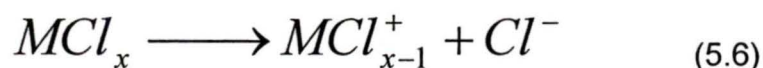


acid *base*

However, transition metal atoms have 3d^m4s² valence electrons, and they have very low electron affinity – no pure metal negative ions were ever detected. Thus, reaction of the metal atoms with Cl⁻ is not reactive. Even if a MCl⁻ was formed, it would be very productive, and it will look for another acid for further reaction.

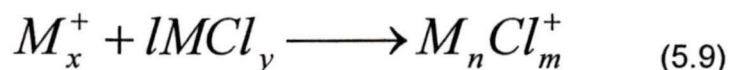
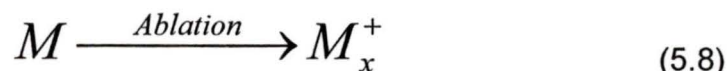
The building block approach introduced for anions does not work as well for cations. This may be because the generation of the positively charged clusters falls into two mechanisms:

1: The building block approach. The components are the stable neutral transition metal chlorides and the positive ions that are formed by loss of one chlorine from the stable neutral transition metal chlorides. Both species are the basic building blocks for the larger positively charged clusters, as is shown in the following equations. This mechanism works for Ti, Cr, Fe and Zn.



$$\text{with } n = l + 1; \quad m = ly + x - 1$$

2: The transition metal may form a positively charged pure metal cluster first. Since this kind of cluster is an excellent Lewis acid, both Cl atoms and the neutral stable metal chlorides can donate electrons to it in order to form the final clusters observed (following equations). This mechanism works for Co, Ni, Cu. Note that small M_2^+ ($M = Co, Ni, Cu$) peaks were detected in all mass spectra of these metals.



$$\text{with } n = x + 1; \quad m = ly + x$$

Since the formation of metal clusters during the ablation is unpredictable, this mechanism produces an irreproducible mass spectrum,. Even under virtually the same experimental conditions, different mass spectra were detected on different days. The clusters formed and detected are still the same, but the intensities vary from time to time.

This second mechanism for positively charged clusters does not work for the negatively charged metal clusters. The reason is that it is difficult for the neutral metal clusters to gain another electron. Neutral metal clusters have very low electron affinities and are not willing to accept electrons; therefore, negatively charged metal clusters can not be formed. The evidence for this is that no pure negatively charged metal clusters (M_n^-) were detected in any of the mass spectra.

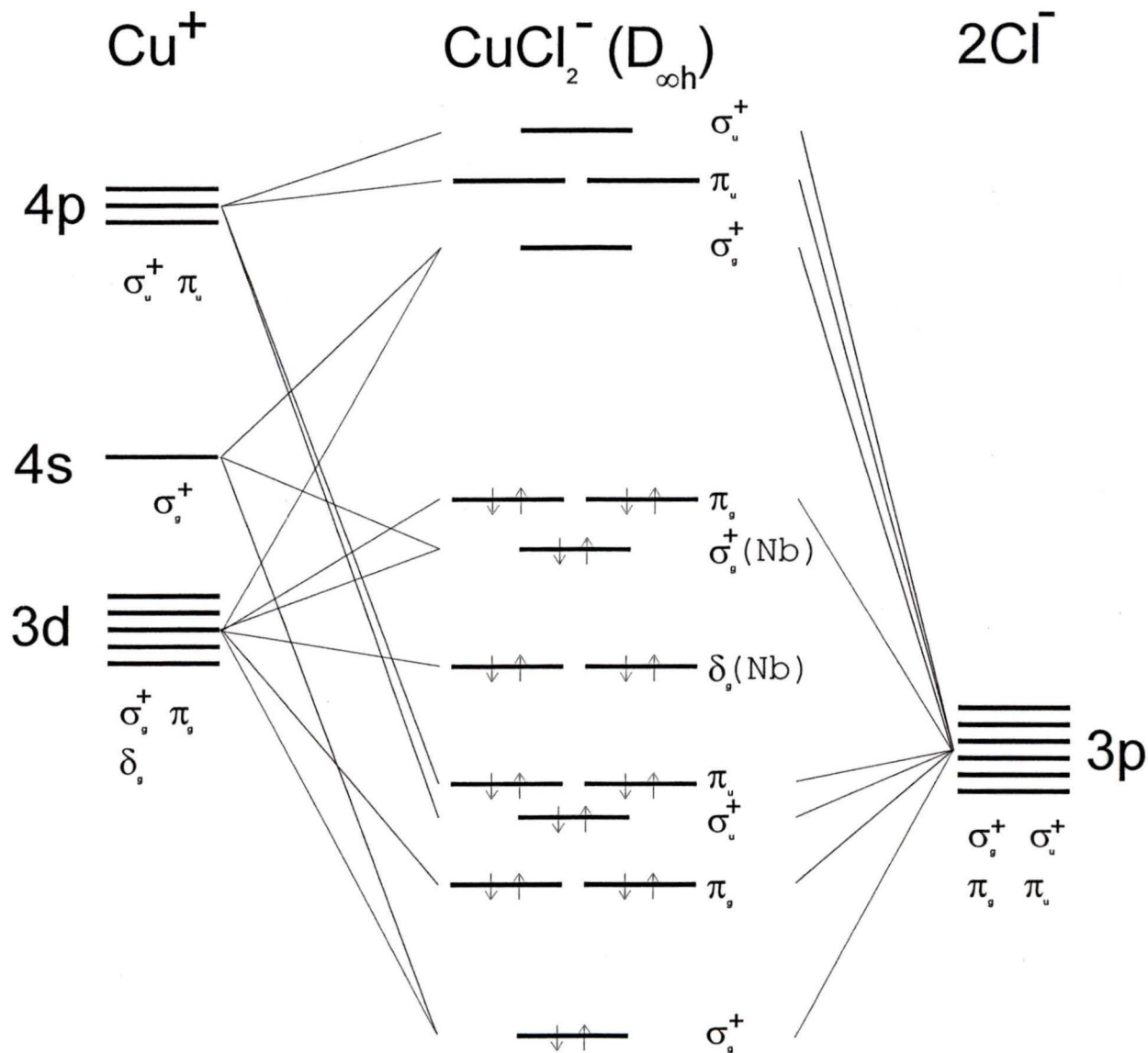
5.2 Molecular orbital considerations

As shown in the previous sections, several stable anions with relatively large yields are observed: $TiCl_4^-$, $CrCl_3^-$, $CrCl_4^-$, $FeCl_4^-$, $CoCl_3^-$, $NiCl_3^-$, $CuCl_2^-$, and $ZnCl_3^-$. In the following discussion, simple molecular orbital models are used to consider the structures of these anions. This discussion is aimed at a qualitative interpretation of the experimental results. A more accurate analysis must await high-resolution spectroscopy studies and/or accurate ab initio calculations.

Figure 5.15 shows a molecular orbital (MO) diagram for linear $CuCl_2^-$. In this MO diagram, the 3s orbital on chlorine was omitted because it will have minimal effect on the qualitative picture presented herein.[55] The $CuCl_2^-$ anion has

electrons filling the bonding and non-bonding MOs, which makes a closed shell configuration. Therefore, CuCl_2^- can be expected to be stable.

Figure 5.15 MO diagram of CuCl_2^-



CuCl_2^- is a common linear anion in solution phase chemistry [56,57]. M.C.L.Gerry used laser ablation Fourier transform microwave spectroscopy in order to study ArCuCl and proved it is also linear [58]. Recent ab initio calculations on CuCl_2

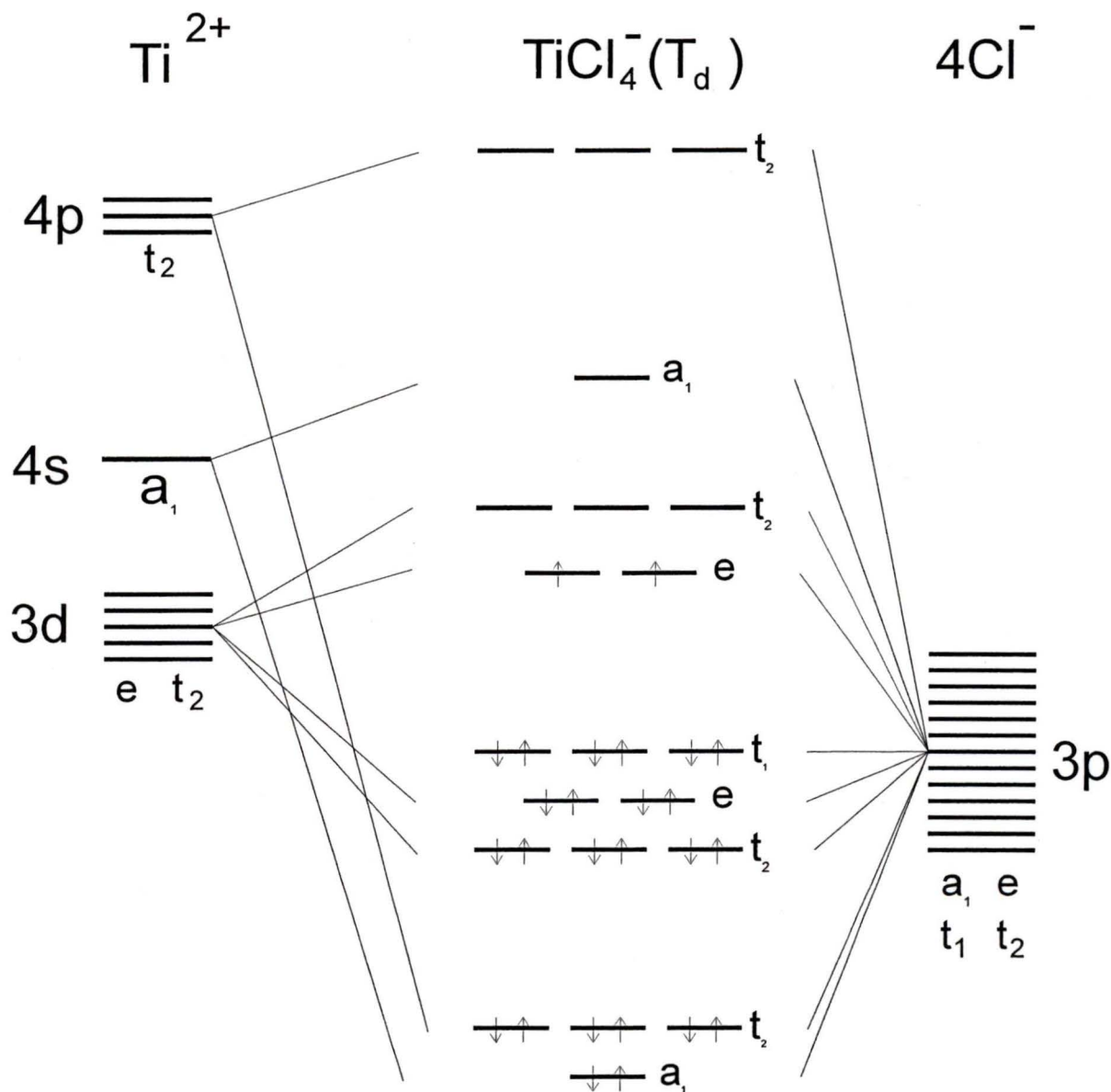
indicate it has a mixed $^2\Sigma_g^+$ and $^2\Pi_g$ ground state [59,60,61], which is in agreement with the MO model of Figure 5.15.

Radicals will be stretched by the electrostatic forces, due to the negatively charged chlorine atoms, and this will lead to a linear geometry. As was discussed previously [62,63,64,65,66,67,68,69,70,71,72,73,74], many of the MCl_2 neutral species are linear. This linear structure will be reinforced by the additional electron in MCl_2^- . The electron affinity of Cl is only 3.61eV; this makes Cl^- a good Lewis base. The ionization energies of copper and chlorine atoms are 7.73 and 12.97 eV, respectively. Based on these considerations and the symmetry just discussed, the negative charge on $CuCl_2^-$ should be delocalized predominantly onto the chlorine atoms.

Figure 5.16 shows the possible structure of the MO diagram for $CrCl_3^-$ constructed for D_{3h} symmetry. $CrCl_3^-$ has a closed shell configuration with an electron configuration of $...(e'')^4$. The unoccupied a_1' and e' orbitals are low lying and can participate in further bonding. This may be the reason that, in the case of chromium, $CrCl_4^-$ has a comparable intensity with $CrCl_3^-$ (61:100). Adding five more electrons to Figure 5.16 will give the MO diagram of $CuCl_3^-$. Thus, $CuCl_3^-$ will have an unpaired electron in the e' orbital which makes it a radical with high reactivity. This may be the reason the intensity of $CuCl_3^-$ is significantly lower than $CuCl_2^-$ (7:100). The negative charge in $CrCl_3^-$ is delocalized to an extent similar to $CuCl_2^-$. Electrostatic repulsion considerations suggest that MCl_3^- anions

NiCl_3^- and ZnCl_3^- . The structures of CoCl_3^- is much more difficult to predict. A MO diagram similar to Figure 5.15 for CoCl_3^- predicts a radical with three unpaired electrons. Therefore, geometric distortion may occur for CoCl_3^- .

Figure 5.17 MO diagram of TiCl_4^-



Simple electron counting for TiCl_4^- and FeCl_4^- implies at least one unpaired electron in each case. Electrostatic considerations lead to a tetrahedral geometry

and stability of the MCl_4^- radical anions. Figure 5.17 shows the MO diagram of $TiCl_4^-$ with tetrahedral symmetry. $FeCl_4^-$ is slightly tetragonally distorted from tetrahedral in the solid phase [77,78,79].

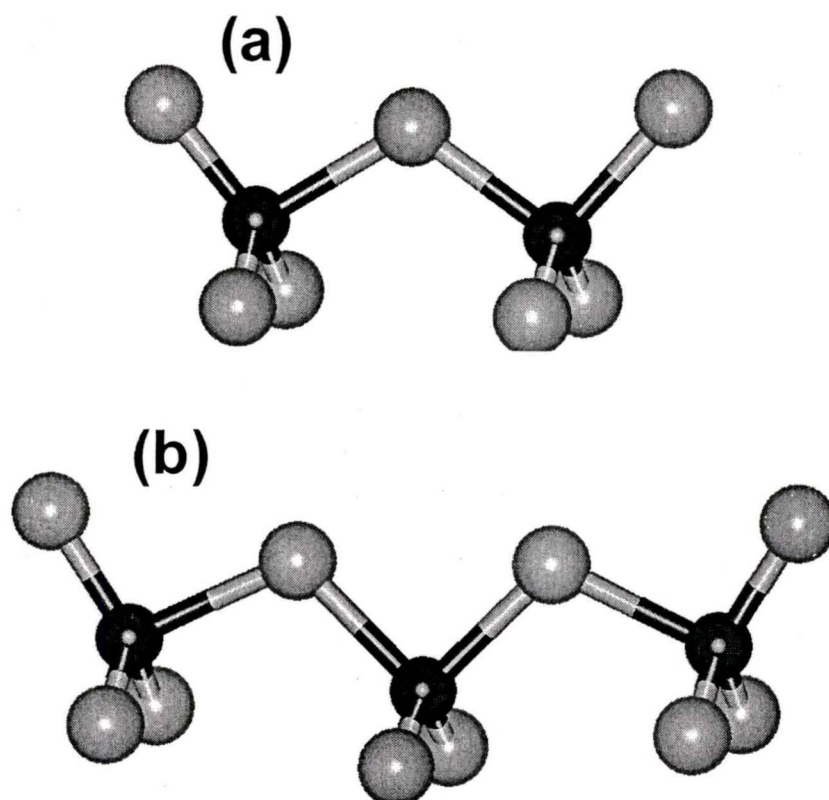
5.3 Aluminum-chlorine Clusters

The aluminum-chlorine clusters were generated from the aluminum rod and 4% chlorine/helium as carrying gas. The negative ion mass spectrum from aluminum was shown in Figure 4.3, in chapter 4. The species detected were $AlCl_4^-$, $Al_2Cl_7^-$, and $Al_3Cl_{10}^-$. The inserts display the fine structure of the $AlCl_4^-$ and $Al_2Cl_7^-$ peak, due to ^{35}Cl and ^{37}Cl isotopes.

The structures of the observed ions can be rationalized as follows. There are three valence electrons in an Al atom. In neutral $AlCl_3$, the Al atom performs sp^2 hybridization, and the three sp^2 orbitals form three σ bonds with the three Cl atoms. However, the Al atom still has an empty p orbital, which makes the $AlCl_3$ molecule a very good electron acceptor. Cl^- has a filled valence shell with 8 electrons; it is a very good electron donor, and therefore can form a strong ligand bond. This is the reason why $AlCl_4^-$ is stable in the gas phase, and is one of the dominant species observed. In addition, the Cl^- in $AlCl_4^-$ can donate electrons to other $AlCl_3$ molecules through other full-filled p orbitals. Thus, $AlCl_4^-$ and $AlCl_3$ are the basic building blocks for the aluminum-chlorine clusters, based on a Cl^- bridge between the two $AlCl_3$ molecules. Taking into account the above discussion, it is not surprising that $AlCl_4^-$ and $Al_2Cl_7^-$ are the two dominant species

in the spectrum, both of these anions occur in molten $\text{AlCl}_3/\text{NaCl}$ [80]. The minor peak in our spectrum can be attributed to $\text{Al}_3\text{Cl}_{10}^-$.

Figure 5.18 The Possible Structure of Negative Aluminum Chlorine Clusters
a: Al_2Cl_7^- , b: $\text{Al}_3\text{Cl}_{10}^-$ (linear)



The actual structures of these aluminum-chlorine compounds needs to be determined from either ab initio calculation or spectroscopy studies. However, the above basic discussion suggests the structures displayed in Figure 5.18.

5.4 Transition Metal-Sulfur Clusters

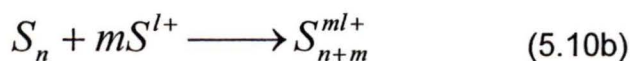
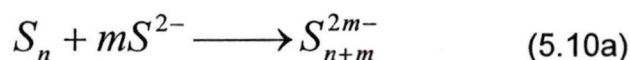
Transition metal sulfur clusters were generated under the same experimental conditions as those used for the generation of transition metal-chlorine clusters. The only difference was that a carrying gas of 3~5% H₂S in He was used.

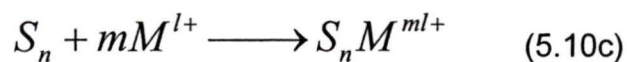
The mass spectra detected for transition metal sulfur clusters (both positively charged clusters and negatively charged clusters), were far more complicated and unpredictable than the spectra detected for chlorine. None of the spectra were reproducible and the intensities of each mass peak varied considerably over time.

The reason for this is believed to be the following:

1: Neutral S_n species are well known stable clusters. The S atoms generated during the laser ablation will combine and form the S_n clusters first. The value of n is unpredictable since this step occurs in the ablation zone of the experiment. The S_n cluster will then react with the other species in order to form the final singly charged clusters detected.

2: Neutral S atoms or the neutral S_n clusters are both good electron donors and acceptors. Ions like S²⁻, S⁺, S²⁺, S⁴⁺, S⁶⁺ are all stable ions and will be in the original plasma. When the S_n cluster collides with S²⁻, it will act like a Lewis acid and react with S²⁻, which is a Lewis base. However, when metal atoms or cations collide with S^{m+} ions, the sulfur species will behave like a Lewis base and be an electron donor for these Lewis acids. The four fundamental reactions are:





Both m and n in these four equations may vary from 0 to 6. These first generated clusters can react further to form the final cluster mixture detected.

3: Since the S atom or the S_n clusters can carry multiple charges, many multiply charged clusters may be generated. Since it is impossible to know the charges carried by a given ion, it is impossible to establish the mass of the observed ion. Moreover, the multiply charged clusters may cover the same time of flight range as the singly charged clusters. For example, $Fe_3S_3^-$ will have the same flight time as $Fe_6S_6^{2-}$.

Figure 5.19_a and Figure 5.19_b show two very different mass spectra of negatively charged nickel-sulfur clusters collected under the same experimental condition. The only difference between the two spectra is that one was obtained two days

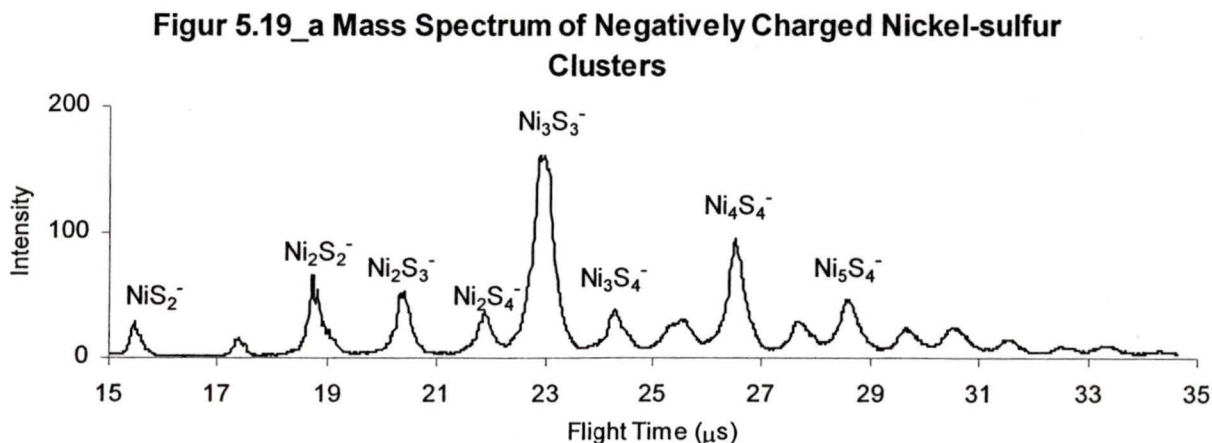
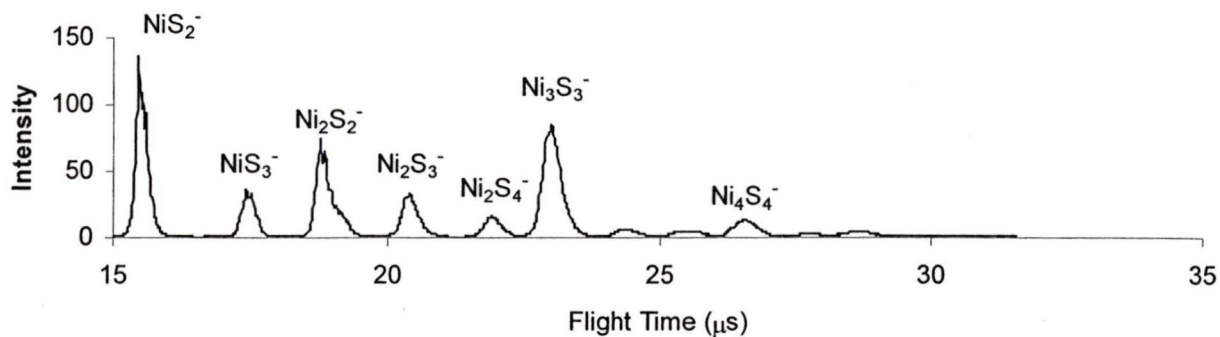


Figure 5.19_b Another Mass Spectrum of Negatively Charged Nickel-sulfur Clusters



after the other. NiS₂⁻ was the dominant mass peak in Figure 5.19_b, but its intensity in Figure 5.19_a is very small. More clusters were detected in Figure 5.19_a, and the dominant peak in Figure 5.19_a can be related to Ni₃S₃⁻. There are several mass peaks (in both Figure 5.19_a and Figure 5.19_b) that can not be assigned a formula with a relative mass. Even those peaks that have a relative formula are just an approximation since the charges are unknown. Moreover, the width of the peaks is large (usually 1.5~1.8 μs) relative to the metal-chlorine ions generated.

Table 5.8 lists all the charged metal sulfur clusters detected. Since their intensities varied from time to time, the species detected are listed without showing their relative intensities.

Table 5.8. Experimentally observed transition metal-sulfur ions and their relative intensity.

Titanium		Chromium		Iron		Cobalt	
TiS_{2-4}^-		CrS_{2-3}^-		FeS_{2-4}^-	Fe^+	CoS_{2-3}^-	Co^+
$Ti_2S_{4-6}^-$		$Cr_2S_{3-4}^-$		$Fe_2S_{2-4}^-$	FeS^+	$Co_2S_{2-4}^-$	CoS_3^+
$Ti_3S_{5-7}^-$		$Cr_3Cl_4^-$		$Fe_3S_{3-5}^-$	$Fe_2S_{1-3}^+$	$Co_3S_{3-4}^-$	
$Ti_4Cl_{6-8}^-$				$Fe_4S_{4-5}^-$	$Fe_3S_{2-4}^+$	$Co_4S_{4-5}^-$	
				$Fe_5S_{5-6}^-$	$Fe_4S_{3-5}^+$	$Co_5S_{4-5}^-$	
				$Fe_6S_6^-$	$Fe_5S_{4-5}^+$	$Co_3Cl_7^-$	
					$Fe_6S_4^+$	$Co_3Cl_8^-$	
Nickel		Copper		Zinc			
NiS_{2-3}^-	Ni^+		Cu^+				
$Ni_2S_{2-4}^-$	$Ni_2S_{1-2}^+$		CuS_{1-2}^+				
$Ni_3S_{3-5}^-$	$Ni_3S_{1-3}^+$		$Cu_2S_{1-4}^+$			Zn^+	
$Ni_4S_{4-5}^-$	$Ni_4S_{2-4}^+$					ZnS_{1-3}^+	
$Ni_5S_{4-5}^-$	$Ni_5S_{3-4}^+$						

Chapter 6 Mass Gate Purification of the Clusters

6.1 Theory

A mass gate is a region with triggered high electric fields, which are grounded at a particular time (the open of the mass gate) for a specific time duration. After charged clusters have been mass selected and their spatial distributions mapped by the repeller, different cluster ions with different mass will fly to the detector with different speeds. Therefore, a mass gate can be inserted between the repeller and the detector. Since the cluster ions move with different speeds according to their mass, they will reach the mass gate at different times. Opening the mass gate at a different time interval will select each specific mass peak or a group of closely related isotopes. A detailed discussion of the setup of the mass gate used in our experiment can be found in Chapter 2.

Figure 6.1 shows the basic setup of the mass gate and the important parameters. The time dependence of the voltage setting of V_M on the second grid of the mass gate is shown in Figure 6.2. The triggering time of the mass gate (t_{tri}) depends upon the flight time of the selected cluster. The time duration of the trigger (t_d) depends upon the width of the original mass peak of the selected cluster.

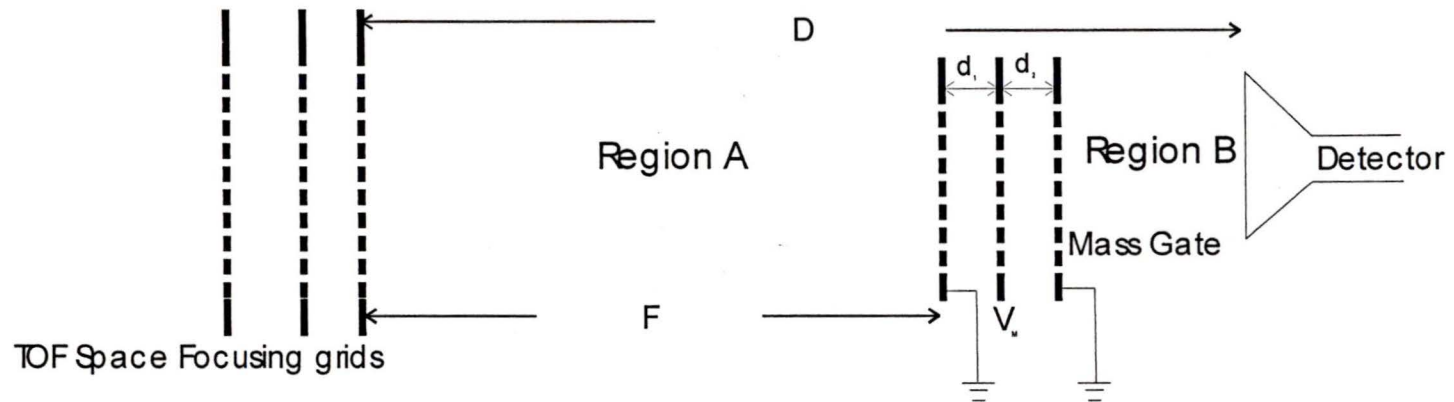


Figure 6.1 Important Parameter settings of the Mass Gate in our experiment
 $D = 90\text{cm}$, $F = 67\text{cm}$, $d_1 = d_2 = 1\text{cm}$

Figure 6.2_a: V_M as a function of time to singly select a specific mass peak or group for a negatively charged cluster

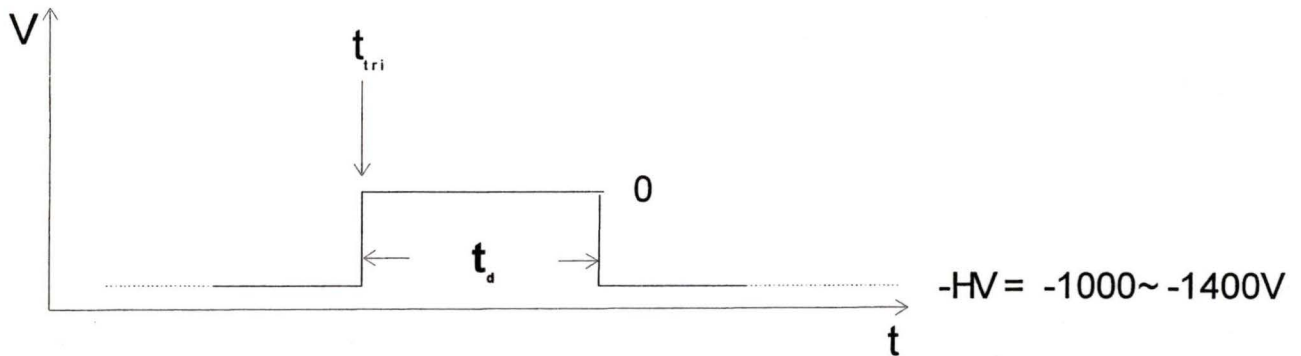
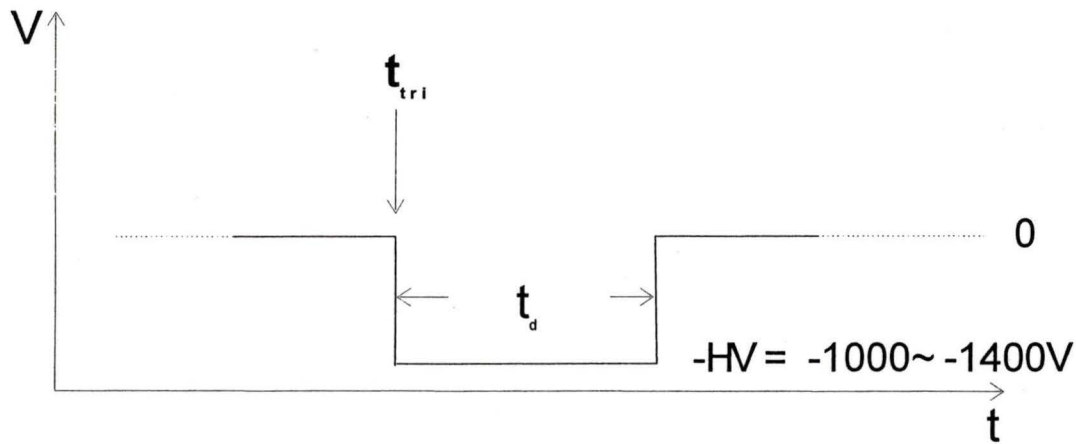


Figure 6.2_b: V_M as a function of time to singly reject a specific mass peak or group for a negatively charged cluster

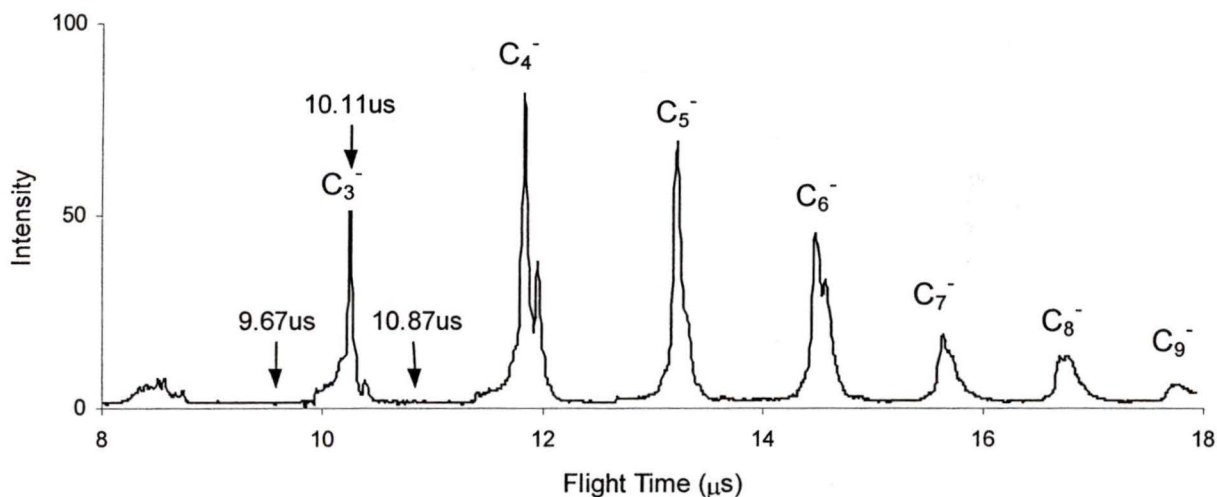


Since the first and third grid of the mass gate were grounded, the region between the repeller and the first grid of the mass gate (A), and the region between the third grid of the mass gate and the detector (B) are field free regions. In these two regions, the ions will move with uniform velocity. The time the cluster spends inside the repeller can be ignored compared with the large

flight time the clusters spend in the field free region. Therefore, the approximate time that a particular cluster will reach the mass gate can be calculated.

Anionic carbon clusters, generated by using carbon rod and pure helium as the carrying gas, were used to test the functionality of the mass gate. The original carbon clusters detected are shown in Figure 6.3.

Figure 6.3: Mass Spectrum of Negative Carbon Clusters



As was mentioned in chapter 2, the oscilloscope used to collect the signal and the repeller of the TOF MS was triggered at the same time. Therefore, the flight time detected on the spectrum for a specific cluster was the flight time that this cluster spent between the repeller and the detector. If this time duration is t_f ,

then the time the cluster needed to fly from the repeller to the mass gate defines a trigger delay time t_{tri} :

$$t_{tri} = t_f \times \frac{F}{D} \quad (6.1)$$

Where F and D are defined by Figure 6.1.

However, clusters with a specific mass will not reach the detector at one single time. Figure 6.3 shows that clusters with specific mass will reach the detector within a time window. For example, the C_3^- cluster will reach the detector in the time window of $9.94\mu s \sim 10.60\mu s$. This means these clusters will reach the mass gate over a time window as well. The mass gate must be opened when the front of the cluster reaches it, and be closed when the tail of the cluster passes by. Clusters with a specific mass were space focused on the detector, which means they left the repeller at different times, with different speeds, but they arrived at the detector at approximately the same time. It is important to note that clusters were not space focused on the mass gate! Thus, they reached the mass gate with a much larger time window than they reached the detector. Therefore, the exact front and tail of flight time, which are directly available from the spectrum, could not be used to calculate the trigger for the mass gate. After many experiments, it was determined that a trigger time which extends both the front and the tail by a factor of $0.2 \sim 0.3 \mu s$ gave the best mass gate performance. Thus, a window of $9.74 \mu s \sim 10.80 \mu s$ was used to set the mass gate trigger for C_3^- .

The delay of the mass gate trigger from the trigger of the repller would then be:

$$t_{tri} = t_f \times \frac{F}{D} = 9.74 \times \frac{67}{90} = 7.25 \mu s \quad (6.2)$$

The width of the trigger would be:

$$t_d = T_{head} - T_{Tail} = 10.80 - 9.74 = 1.06 \mu s \quad (6.3)$$

However, these are approximate values. During experiments, they were adjusted to achieve the best result. Usually, the width of the trigger would be adjusted to a value much larger than the value calculated. The real voltage change of this trigger during the experiment was not shaped exactly as the “perfect” trigger shown in Figure 6.2. It would have a large tail at both the rising edge and the falling edge as shown in Figure 6.4. The voltage on the mass gate required several microseconds in order to increase to precisely 0V or to decrease to the -HV desired. This sometimes requires the width of the trigger to be extended to approximately 5 μs .

The width of the trigger must be extended so that when the clusters with the selected mass reach the mass gate, the voltage on the second grid of the mass gate is low enough. As a consequence, there will be clusters with other masses arriving at the mass gate during the time of the “rising tail” and the “falling tail”. These clusters will then penetrate the mass gate and reach the detector, which will produce impurities in the mass selection. The real values used for the trigger of the mass gate are a balanced result, the goal is to get the best functionality of mass selection without impurity ions.

Figure 6.4 The real mass gate voltages profiles

a: To select negatively charged clusters with a specific mass



b: To reject negatively charged clusters with a specific mass



The value of the voltage set on the second grid of the mass gate (V_m) is a second experimental variable. Theoretically, since the acceleration voltage of the repeller is 1400V in total, V_m should be set to 1400V. However, since most of the clusters will be accelerated in the middle of the first and second grid of the repeller, the clusters will leave the repeller with kinetic energies smaller than 1400eV. This means that V_m does not have to be as high as 1400V. In addition, the higher the voltage, the longer the tails at the two edges (Figure 6.4). Experimental values for V_m varied from 750V to 1300V; this value was adjusted to optimize the final mass spectrum.

6.2 Selection and rejection of clusters of a specific mass

In this case, the carbon clusters detected were used as an example in order to present the result of mass gate selection.

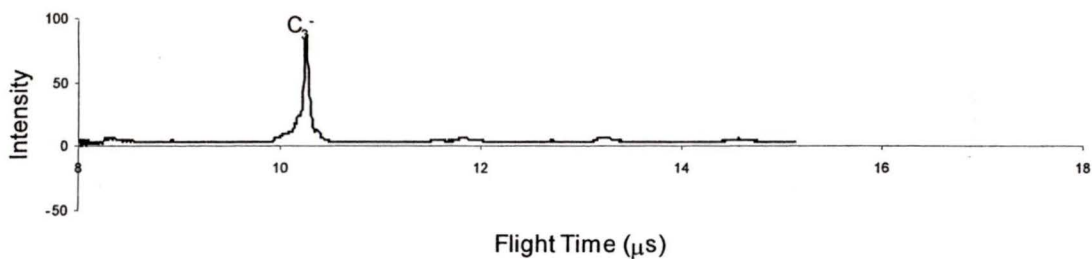
6.2.1 Selection of clusters with one specific mass

Figure 6.5 shows the result of the mass selection of the mass gate, and the delay of the trigger for the mass gate from the trigger of the repeller. The width of the trigger in all cases was set to 4 μs . As shown in the figure, delays of 7.2 μs , 8.3 μs , and 9.5 μs were used to singly select C_3^- , C_4^- and C_5^- .

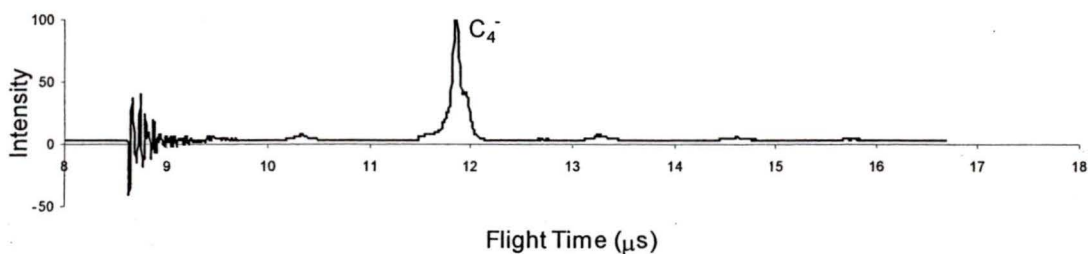
The reason for the oscillations at the beginnings of a,b and c of Figure 6.5 is believed to be as follows: The mass gate is very close to the detector. It behaved as a strong microwave source due to the high voltage switching. The detector acted as an antenna, and picked up this signal and generated the oscillations. In order to avoid this, an aluminum plate was insert between the mass gate and the detector to shield the microwave. However, the source was so strong that it could not be completely shielded.

Figure 6.5: The selection result of the mass gate to select clusters with a specific mass

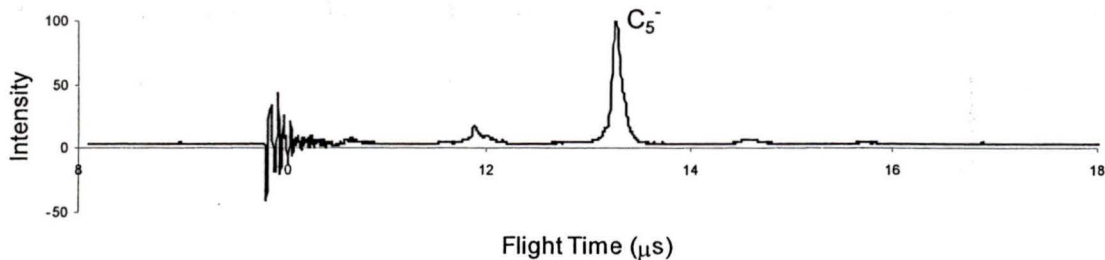
a: Mass Gate Trigger Delay = 7.2 μ s



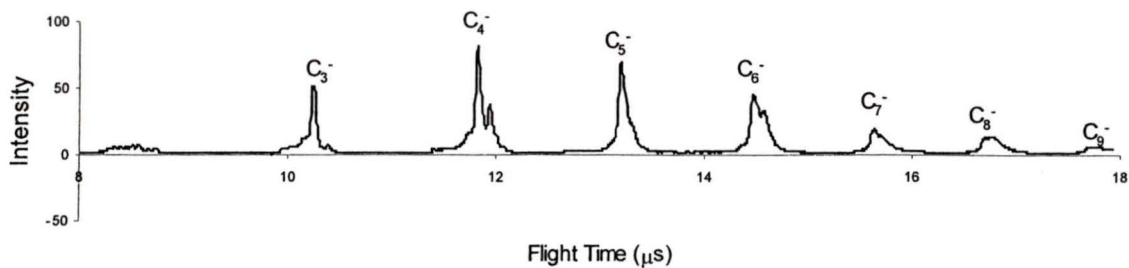
b: Mass Gate Trigger Delay = 8.3 μ s



c: Mass Gate Trigger Delay = 9.5 μ s



d: the Original Mass Spectrum of Negative Carbon Clusters



The functionality of the mass gate selection (purification) is shown in the following tables:

Table 6.1 The functionality of the mass gate for single ion selection

Ion Selected	Trigger Delay	Trigger Width	% of C ₃ ⁻ remaining	% of C ₄ ⁻ remaining	% of C ₅ ⁻ remaining	% of C ₆ ⁻ remaining	% of C ₇ ⁻ remaining	% of C ₈ ⁻ remaining
C ₃ ⁻	7.2μs	4μs	>95%	2%	1.5%	1%	0	0
C ₄ ⁻	8.3μs	4μs	1.5%	>95%	1%	0.5%	<0.5%	0
C ₅ ⁻	9.5μs	4μs	1.5%	4%	>95%	1.2%	0.5%	<0.5%

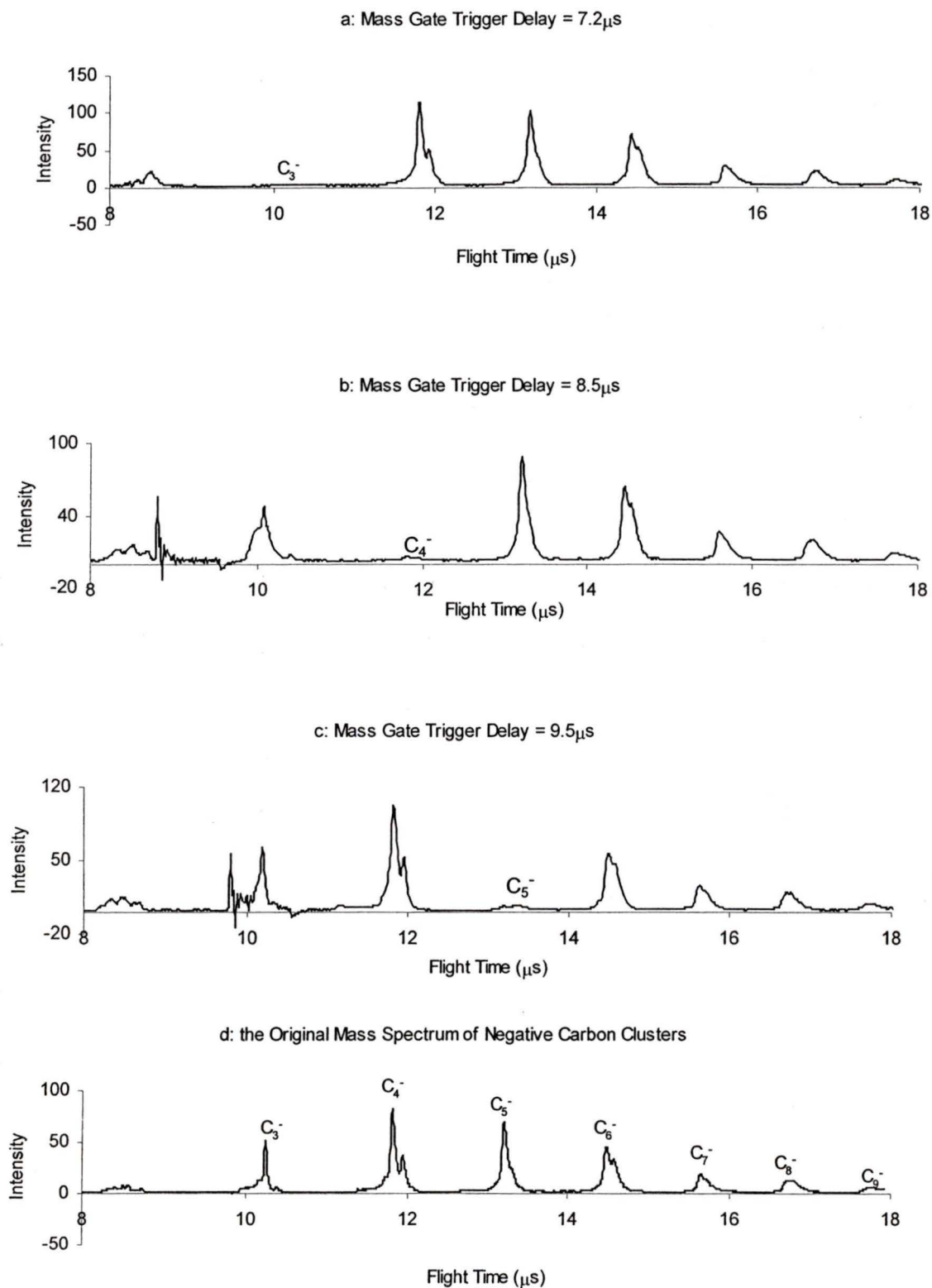
6.2.2 Rejection of clusters with one specific mass

If the setting of V_m was changed, as was shown in Figure 6.2_b, clusters with a specific mass can be rejected by the mass gate. The resultant mass spectra are shown in Figure 6.6, and the functionality of the mass gate rejection is shown in the following table:

Table 6.2 The functionality of the mass gate single rejection

Ion Rejected	Trigger Delay	Trigger Width	% of C ₃ ⁻ remaining	% of C ₄ ⁻ remaining	% of C ₅ ⁻ remaining	% of C ₆ ⁻ remaining	% of C ₇ ⁻ remaining	% of C ₈ ⁻ remaining
C ₃ ⁻	7.2μs	4μs	<0.5%	>95%	>95%	>95%	>95%	>95%
C ₄ ⁻	8.3μs	4μs	>95%	1%	>95%	>95%	>95%	>95%
C ₅ ⁻	9.5μs	4μs	>95%	>95%	2.5%	>95%	>95%	>95%

Figure 6.6: The rejection result of the mass gate to reject clusters with a specific mass



Chapter 7: Conclusion

7.1 Summary

The goal of this thesis was to provide information to facilitate further spectroscopic study of transition metal-chlorine and transition metal-sulfur clusters.

Effectively, this thesis reports on how to produce clusters with the maximum intensity; detailed characterization of the plasma generated by laser ablation was also accomplished. The approximate flight speed of the charged clusters was studied. Positively charged clusters were shown to have a slower original flight speed than negatively charged clusters. The approximate time window in which the negatively charged clusters and the positively charged clusters would reach the repeller with the maximum density was also measured. The density distribution of the clusters in the original beam was studied: the maximum density of the clusters occurred at approximately 5 ~ 6cm beyond the center of the beam. The length of the molecular beam was affected only by the duration time the molecular beam nozzle was opened.

In order to carry out a spectroscopic study of clusters, these clusters must be separated from the original beam and be space focused so that they are gathered in the same region at the same time. A functional triggered TOF-Mass spectrum was built with adjustable space focusing parameters (the ratio of the voltage differences of the two acceleration regions). This setup works to space focus the positively or the negatively charged cluster generated by the laser

ablation. The optimized mass resolution ($M/\Delta M$) this setup can provide is about 300.

No ionic clusters composed of only a transition metal and chlorine or sulfur have been previously reported in the gas phase. However, many such new species were synthesized through our experiments, and a survey of the transition metal–chlorine clusters was conducted. Trends evident in the formation of negatively charged clusters can be explained by a simple building block model. In general, the negatively charged clusters were generated by using two basic building blocks:

1: the neutral metal-chlorine compounds (MCl_n), which are stable in both the solid state and in the gas phases. One metal element may have several stable chlorides.

2: the negative ions that were formed by adding one Cl^- ion to the stable neutral compound (MCl_{n+1}). Since one metal can have several stable chlorides, a range of different negative ions can be generated accordingly. These negative ions are stable in the gas phase. Among all the mass peaks detected, they usually have the biggest intensity.

To a lesser extent, the building block model can also be applied to some of the positively charged clusters observed. However, the building block approach introduced for anions does not work as well for cations. This may be because the generation of the positively charged clusters falls into two mechanisms:

1: The building block approach. The components are the stable neutral transition metal chlorides (a) and the positive ions that were formed by loss of

one Cl from the stable neutral transition metal chlorides (b). Both a and b are the basic building blocks for the larger positively charged clusters. This mechanism works for Ti, Cr, Fe and Zn.

2: The transition metal may first form a positively charged pure metal cluster. Since this type of cluster is a very good Lewis acid, both the Cl atom and the neutral stable metal chloride can donate electrons to it and form the final clusters observed. This mechanism works for Co, Ni, Cu.

The early transition metals do not form larger clusters with more than one metal atom. Larger cluster formation was observed in the middle and late transition metal complexes. Positively charged clusters had fewer Cl atoms than similar negative complexes. The formation of transition metal sulfur clusters was far more complicated, only a brief discussion was presented.

These experiments provided sufficient densities of small positively charged and negatively charged clusters to make spectroscopic characterization possible. In order to provide an optical spectrum of a selected cluster, the cluster must be separated from the many other types of clusters generated at the same time. Therefore, a functional mass gate was built. The mass gate can be used to isolate a particular mass peak with about 95% purity for clusters with a flight time difference of 1.1 μ s. This results implies that a detailed spectroscopy study of these small charged metal-chlorine clusters is just one step in the future.

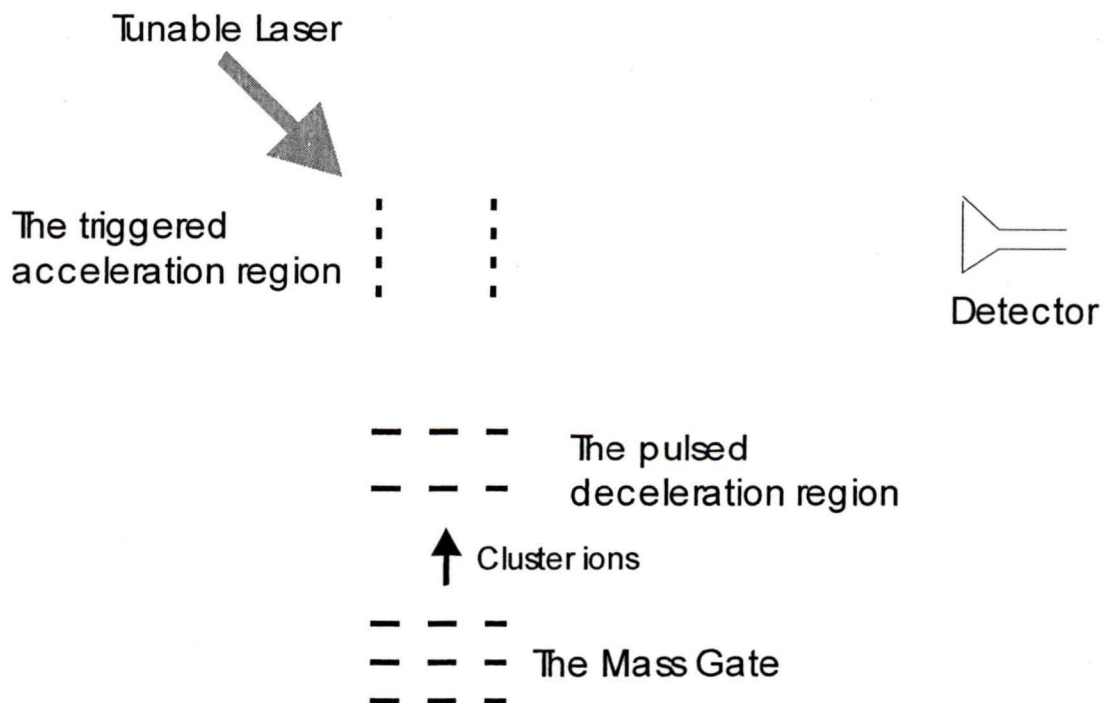
7.2 Possible Future Spectroscopy Work

This thesis provides fundamental information necessary for further spectroscopic work. The next logical step is to study these transition metal cluster.

The future work can be accomplished as follows:

1: Since the clusters are still moving fast, and this makes the capture of the selected clusters by a second laser very difficult, a pulsed deceleration region may be inserted between the mass gate and the detector. As shown in Figure 7.1, this deceleration region will reduce the kinetic energy of the clusters to about 5eV.

Figure 7.1: A possible modification to perform spectroscopic work



2: As the clusters pass the deceleration region, they can easily be captured by a second tunable laser. This laser can then provide a multi-photon ionization of the selected clusters. The electrons generated by this ionization can then be accelerated by a second pulsed electronic field. Since it is electrons that will be accelerated, the voltage of this field need only be approximately 10V. The detector will detect the electrons generated. A record of the wavelength of the tunable laser against the signal intensity will provide the photo electron spectrum.

By studying the spectrum, information about both the ground state and the excited states of the cluster can be gained. Since the ground and the excited states information can provide information related to molecular symmetry and bonding information, the possible structure of the specific cluster can then be studied.

References

-
- [1] H. Kroto, *Rev. Mod. Phys.* 69, (1997), 703.
- [2] R.E. Smalley, *Rev. Mod. Phys.* 69, (1997), 723.
- [3] R.F. Curl, *Rev. Mod. Phys.*, 69, (1997), 691.
- [4] B. Gerald, *Solid State Physics*, Academic Press, Toronto, (1985).
- [5] H. Stromsnes, S. Jusuf, O. Gropen, *J. Mol. Str.*, 567, (2001), 137.
- [6] J.R. Reimers, N.S. Hush, *J. Phys. Chem. B*, 105(37), (2001), 8979
- [7] T. Wenzel, J. Bosbach, F. Trager, *App. Phys. B, Laser and Optics*, 69 (5-6), 1999, 513
- [8] L. S. Zheng, C. M. Karner, P.J. Brucat, S.H. Yang, C. L. Pettiette, M. J. Craycraft, R.E. Smalley, *J. Chem Phys.* 85, (1986), 1681.
- [9] R. A. Larson, S. K. Neoh, D. R. Gerschbach, *Rec. Sci. Instrum.* 45, (1984), 1151.
- [10] T. P. Martin, T. Bergmann, *J. Chem. Phys.*, 90, (1989), 6664.
- [11] G. Gantefor, K. H. Meiwes-Broer, H. O. Lutz, *Phys. Rev. A*, 37, (1988), 2716.
- [12] I. Katause, T. Ichihara, Y. Fujita, T. Matzuo, T. Sakurai, and H. Matsuda, *Int. J. Mass Spectrom. Ion Processes* 67, (1985), 229.
- [13] W.A. Saunders, S. Fredrigo, *Chem. Phys. Lett.* 156, (1989), 14.
- [14] M. D. Morse, *Chem. Rev.* 86, (1986), 1049.
- [15] X. B. Wang, L. S. Wang, H. Schwarz, *J. Chem. Phys.*, 114(17), (2001), 7388.
- [16] G. V. Chertihin, L. Andrews, *J. Chem. Phys.* 106, (1997), 3457.
- [17] G.V. Chertihin, W. D. Bare, L. Andrews, *J. Chem. Phys.* 107, (1997), 2798.
- [18] G. V. Chertihin, W. D. Bare, L. Andrews, *J. Phys. Chem.* 101, (1997), 5090.
- [19] G.V. Chertihin, L. Andrews, C. W. Bauschlicher, *J. Phys. Chem.*, 101, (1997), 4026.
- [20] Z. Hu, B. Shen, J. R. Lombardi, D. M. Lindsay, *J. Chem. Phys.*, 96, (1992), 8757.
- [21] E. Fujimaki, A. Fujii, T. Ebata, N. Mikami, *J. Phys. Chem.*, 105 (20), (2001), 4882.
- [22] A. Fujii, E. Fujimaki, T. Ebata, N. Mikami, *J. Chem. Phys.* 112 (14), (2000), 6275.
- [23] E. Fujimaki, Y. Matsumoto, A. Fujii, T. Ebata, N. Mikami, *J. Phys. Chem.* 104 (31), (2000), 7227.

-
- [24] R. Takasu, K. Nishikawa, N. Miura, A. Sabu, K. Hashimoto, C .P. Schulz, I.V. Hertel, K. J. Fuke, *Phys. Chem. A.*, 105 (27), (2001), 6602.
- [25] W.Y. Lu, P. D. Kleiber, *J. Chem. Phys.* 114 (23), (2001), 10288.
- [26] B. Y. Man, J. Zhang ; P. G. Ni, D. Z. Zhang, *Chi. Phys. Lett.*, 17 (9), (2000), 672.
- [27] C. X. Su and P. B. Armentrout, *J. Chem. Phys.* 99, (1993), 6506.
- [28] C. X. Su, D. A. Hales, P. B. Armentrout, *J. Chem. Phys.*, 99, (1993), 6613.
- [29] L. Lian, C. X. Su, P. B. Armentrout, *J. Chem. Phys.*, 97, (1992), 4084.
- [30] L. Lian, C. X. Su, P. B. Armentrout, *J. Chem. Phys.* 97, (1992), 4072.
- [31] L. Lian, C. X. Su, P. B. Armentrout, *J. Chem. Phys.* 97, (1992), 7542.
- [32] E. K. Parks, K. Liu, S. C. Richtsmeier, L. G. Pobo, S. J. Riley, *J. Chem. Phys.* 82, (1985), 5470.
- [33] E. K. Parks, G. C. Nieman, L. G. Pobo, S. J. Riley, *J. Chem. Phys.* 88, (1988), 6260.
- [34] S. J. Riley, E. K. Parks, L. G. Pobo, S. Wexler, *Ber. Bunsenges., Phys. Chem* 88, (1984), 287.
- [35] L.S. Wang , H. B. Wu , H. S. Cheng, *Phys. Rev. B*55 (19), (1994), 12884.
- [36] L. S. Wang, H. B. Wu, *J.Chem. Phys.* 107(1), (1997), 16.
- [37] H. B. Wu, L. S. Wang, *J.Chem. Phys.* 107(20), (1997), 8221.
- [38] J. H. D. Eland, *Photoelectron spectroscopy*, Butterworths, London, (1984).
- [39] C. C. Arnold, C. Xu, G. R. Burton, D. M. Neumark, *J. Chem. Phys.* 102, (1995), 6982.
- [40] C. C. Arnold, Y. Zhao, T. N. Kitsopoulos, D. M. Newmark, *J. Chem. Phys.*, 97, (1997), 6121.
- [41] G. Drechsler, U. Boesl, C. B. Bmann, E. W. Schlag, *J. Chem. Phys.* 107, (1997), 2284.
- [42] D. S. Yang, A. M. James, D. M. Rayner, P. A. Hackett, *Chem. Phys. Lett.*, 231, (1994), 177.
- [43] D. S. Yang, A. M. James, D. M. Rayner, P. A. Hackett, *J. Chem. Phys.*, 102, (1995), 3129.
- [44] D. S. Yang, B. Simard, P. A. Hackett, A. Breces, M. Z. Zgierski, *Int. J. Mass Spectr. Ion Proc.* 159, (1996), 65.

-
- [45] D. S. Yang, M. Z. Zgierski, D. M. Rayner, P. A. Hackett, A. Martinez, D. R. Salahub, P.-N. Roy, T. Carrington, *J. Chem. Phys.* 103, (1995), 5335.
- [46] D. Bellert, W. H. Breckenridge, *Chem. Phys. Lett.* 337 (1-3), (2001), 103.
- [47] Y. Yoon, Y. Lee, T. Kim, J. S. Ahn, Y. Jung, B. Kim, S. J. Lee, *Chem. Phys.*, 114 (20), (2001), 8926.
- [48] P. Imhof, W. Roth, C. Janzen, D. Spangenberg, K. Kleinermanns, *Chem. Phys.*, 242 (2), (1999), 141.
- [49] M. Izuha, K. J. Yamanouchi, *Chem. Phys.* 113 (24), (2000), 10999.
- [50] G. M. Greetham, M. J. Hanton, A. M. Ellis, *Phys. Chem. Chem. Phys.* 1 (11), (1999), 2709.
- [51] D. Proch, T. Trickl, *Rev. Sci. Instrum.*, 60, (1989), 713
- [52] J. Cao, Y. Wang, C. X. W. Qian, *J. Chem. Phys.*, 103, (1995), 9653.
- [53] P. W. Dyer, V. C. Gibson, J. C. Jeffery. *Polyhedron* 14 (20-21), (1995), 3095
- [54] A. R. H. Alsoudani, A. S. Batsanov, P. G. Edwards. *J Chem. Soc DALTON*, 7, (1994), 987.
- [55] D. L. Price, M. L. Saboungi, Y. S. Badyal, J. Wang, S. C. Moss, R. L. Leheny, *Phys. Rev. B* 57, (1998), 10496.
- [56] J. M. Poblet, M. Bénard, *Chem. Commun.*, (1998), 1179.
- [57] G. Exarchos, S.C. Nyburg, S.D. Robinson, *Polyhedron*, 17, (1998), 1257.
- [58] C.J. Evans, M.C.L. Gerry, *J. Chem. Phys.*, 112, (2000), 9363.
- [59] C.W. Bauschlicher Jr., B.O. Roos, *J. Chem. Phys.*, 91, (1989), 4785.
- [60] F. Rogemond, H. Chermette, D.R. Salahub, *Chem. Phys. Lett.*, 219, (1994), 228.
- [61] A.J. Bridgeman, *J. Chem. Soc. Dalton Trans.*, (1996), 2601.
- [62] C.W. Bauschlicher Jr., B.O. Roos, *J. Chem. Phys.*, 91, (1989), 4785.
- [63] R.J. Deeth, *J. Chem. Soc. Dalton Trans.*, (1993), 1061.
- [64] F. Rogemond, H. Chermette, D.R. Salahub, *Chem. Phys. Lett.*, 219, (1994), 228.
- [65] A.J. Bridgeman, *J. Chem. Soc. Dalton Trans.*, (1996), 2601.
- [66] A.J. Bridgeman, C.H. Bridgeman, *Chem. Phys. Lett.*, 272, (1997), 173.
- [67] M.C. Drake, G.M. Rosenblatt, *J. Electrochem. Soc.*, 126, (1979), 1387.

-
- [68] D.W. Green, D.P. McDermott, A. Bergman, *J. Mol. Spectrosc.*, 98, (1983), 111.
- [69] M. Hargittai, I. Hargittai, *J. Mol. Spectrosc.* 108, (1984), 155. (and references cited therein)
- [70] J.S. Ogden, R.S. Wyatt, *J. Chem. Soc. Dalton Trans.*, (1987), 859.
- [71] M. Hargittai, *Coord. Chem. Rev.*, 91, (1988), 35.
- [72] M. Hargittai, N.Y. Subbotina, M. Kolonits, A.G. Gershikov, *J. Chem. Phys.*, 94 (1991), 7278.
- [73] S.H. Ashworth, F.J. Grieman, J.M. Brown, P.J. Jones, I.R. Beattie, *J. Am. Chem. Soc.*, 115, (1993), 2978.
- [74] S.H. Ashworth, F.J. Grieman, J.M. Brown, *J. Chem. Phys.*, 104, (1996), 48.
- [75] M.C. Drake, G.M. Rosenblatt, *J. Electrochem. Soc.*, 126, (1979), 1387.
- [76] D.W. Green, D.P. McDermott, A. Bergman, *J. Mol. Spectrosc.*, 98, (1983), 111.
- [77] B. Zaslów, R.E. Rundle, *J. Phys. Chem.*, 61 (1957) 490.
- [78] T.J. Kistenmacher, G.D. Stucky, *Inorg. Chem.*, 7 (1968) 2150.
- [79] F.A. Cotton, C.A. Murillo, *Inorg. Chem.*, 14 (1975) 2467.
- [80] I.R. Beattie, P.J. Jones, J.A.K. Howard, L.E. Smart, C.J. Gilmore, J.W. Akitt, *J.C.S. Dalton*, (1979), 528.

VITA

Surname: Yu

Given name: Yongzhi

Place of Birth: Changchun, Jilin, P.R.China

Educational Institutions Attended:

University of Victoria	1998 to 2002
University of Science and Technology of China	1992 to 1997

Degrees Awarded:

B.Sc.	University of Science and Technology of China	1997
-------	---	------

Awards:

University of Victoria Fellowship	2000 to 2001
Dr. E. & Mrs. M. Von Rudloff award, University of Victoria	1999
Outstanding Student Scholarship, University of Science and Technology of China	1995
Outstanding Student Scholarship, University of Science and Technology of China	1993
Second award, Chinese National Mathematics Championship	1991
Second award, Northern China Mathematics Championship	1990

Publication:

Transition metal-chlorine anions and cations: monomers, clusters, and periodic trends
Chuan-Fan Ding, Yongzhi Yu, Roy H. Jensen, Walter J. Balfour and Charles X.W. Qian
Chemical Physics Letters, 2000, V 331, N 2-4, 1 December, 163-169


Partial Copyright License

I hereby grant the right to lend my thesis to users of the University of Victoria Library, and to make single copies only for such users or in response to a request from the Library of any other university, or similar institution, on its behalf or for one of its users. I further agree that permission for extensive copying of this thesis for scholarly purposes may be granted by me or a member of the University designated by me. It is understood that copying or publication of this thesis for financial gain shall not be allowed without my written permission.

Title of Thesis:

Space Focusing and Mass Selection of Transition-metal-chlorine and -sulfur Clusters Generated Through Laser Ablation

Author:



Yongzhi Yu

April 2, 2002

Draft printed at 04/03/02 10:09 AM